



Resonating Nanomechanical Microcantilevers for Quantitative Biological Measurements in Liquid

Inauguraldissertation

zur

Erlangung der Würde eines Doktors der Philosophie

vorgelegt der

Philosophisch-Naturwissenschaftlichen Fakultät

der Universität Basel

von

Murali Krishna Ghatkesar

aus Hyderabad, Indien

Basel, 2007

Genehmigt von der Philosophisch-Naturwissenschaftlichen Fakultät auf Antrag der
Herren Professoren:

Prof. Dr. Hans-Joachim Güntherodt (Faculty Responsible)

Prof. Dr. Ernst Meyer (Co-referee)

Basel, den 12, Juni 2007

Prof. Dr. Hans-Peter Hauri, Dekan

Life is not an easy matter.... You cannot live through it without falling into frustration and cynicism unless you have before you a great idea which raises you above personal misery, above weakness, above all kinds of perfidy and baseness.

To my beloved parents and all my teachers

ACKNOWLEDGEMENTS

*"I would thank you from the bottom of my heart,
but for you my heart has no bottom." – Anonymous*

The outcome of this thesis is an effort and support of many wonderful people to whom I sincerely express my deepest gratitude. The first person to thank is my research supervisor Dr. Hans Peter Lang. I am grateful to him for introducing me to the fascinating world of nanotechnology and giving me an opportunity to pursue my thesis in the area of cantilever sensors. His optimism, enormous patience, very caring nature, vast knowledge, trust in me and freedom he gave, made my work very smooth. His help during my initial days in a completely new country, ever availability, perseverance for perfection has made redefine some of the basic human characteristics in me.

I am grateful to Prof. Dr. Christoph Gerber, tech guru of STM, AFM, and cantilever sensors, Prof. Dr. Hans-Joachim Güntherodt, father of nanoscience at Institute of Physics for giving me a Ph.D. position to work in their group. I also thank Prof. Dr. Ernst Meyer, head of UHV Force Microscopy group, University of Basel for kindly accepting to be my referee. The secret of their success which I understood is their unflinching enthusiasm to make a difference in this world. Every time I spoke to Christoph, his power packed words and great visions, gave me tremendous motivation and confidence in the work that I do. It is a great honor for me to work with such eminent and valuable scientists. I thank Prof. Dr. Peter Oelhafen for kindly agreeing to chair my defence.

My earnest thanks goes to PD Dr. Martin Hegner for adding "bio" to my career. With his extraordinary skills in both biology and physics, he is the cardinal link for the scientists in two fields. His lectures on fundamentals of biology taught me how beautiful is nature in doing certain things by itself. His motivation, encouragement and support to further my knowledge in "NanoBio" is enormous.

A person who added value to my every result in this thesis work is Dr. Thomas Braun. His steadfast knowledge in biology, physics, software, geography of Switzerland and history of Europe are amazing. His hospitality to any new person he meets is uncomparable. He carefully taught me many finer aspects of biology and physics explaining the beauty and elegance of nature. His ever availability, wonderful problem solving skills and kindness have always kept my work at ease. Long discussions in the Mensa interpreting our results, gentle but elegant critiques have improved the quality of my work. He has imbibed new perspectives in my life. I thank him for every contribution he made.

My first teacher on microcantilevers is Dr. Viola Barwich. She elegantly taught me the physics and mathematics behind dynamic mode cantilever sensors. She also taught me how to be organized and handle the setup. The lesson I learnt from her is to keep things simple and easy to use. Thanks Viola.

The scientific temper in the lab is set by wonderful smiling and fun loving colleagues Dr. François Huber, Dr. Natalija Backmann and Dr. Natalia Nugaeva. Thank you for teaching me essential basics of biology and wet lab techniques. I cherish all the fun moments we had in the Mensa and other gatherings. Marc Karle with his typical German style always inspires me to be well organized. A person whom I cannot reach his speed is Dr. Wilfried Grange. His super fast TGV speed of thinking is unbeatable. His command on labview programming has accelerated and improved the quality of the setup to a great extent. I thank him for his time and kindness to help me. I also thank all my former colleagues Dr. Jiayun Zhang, Dr. Karin Gfeller, Dr. Patricia Bertoncini, Adriaan Bredekamp, Avigail Abuhatsira for some of the wonderful moments I shared. I am also thankful to short term visitors Dr. Rachel McKendry for her help in pH experiments, Dr. Rupa Mukhopadhyay for her motivation, Martin Lorentzen for sharing his typical Danish style, Fernando Mancilla for his Mexican food, Dr. Shin Hur for his Korean gifts. Many discussions on resonating cantilevers in liquid with Dr. Marko Dorrestijn were very useful. It was fun solving puzzles with him. We welcome Dr. Genki Yoshikawa to the world of cantilever array sensors.

Experimental physicists research dreams can never be realized without skilled technical help. I acknowledge Jean-Pierre Ramseyer for his acumen and providing solutions to every problem. He taught me many general technical aspects of engineering. I remember all the lighter moments we shared sitting adjacent to each other in the same office. I am also grateful to Andy Tonin for his perfect design of electronic circuits and chocolate bars in his office, Dr. Hans-Rudolf Hidber for every kind of software and all the animations beautifully explaining the working principle of cantilever sensors, Dr. Peter Reimann for his optical microscope and wonderful technical solutions and Jakob Silvester for his ultra fine machine skills in fabricating the liquid chamber. Over all I thank all the skilled technical experts of mechanical and electronic workshop for helping me at different times.

All the administrative help very generously came from Ms. Germaine Weaver, Ms. Barbara Kammermann, Ms. Astrid Kalt, Ms. Audrey Fischer and Ms. Jacqueline Vetter. Being alien to German language their help at all levels made every processes very easy for me. Many thanks to all of you.

My special thanks to Kate Rakhmatullina for her help in dynamic light scattering experiments and viscosity measurements. All the wonderful weekends playing badminton, fun filled gatherings and hiking trips will be remembered. I should also thank her and other Russian colleagues for introducing me to typical Russian vodka. I am also thankful to Late Mr. Holger Hammerich for viscosity measurements and Dr. Christian Dittrich for allowing me to use his extruder to prepare vesicles at the Department of Organic Chemistry, University of Basel. I acknowledge Dr. Thomas Kaufmann at Biozentrum, University of Basel for teaching me about lipids and his time for doing contact angle measurements for me. REM lab experts Dr. Markus Dürrenberger, Marcel Düggelein and Daniel Mathys are acknowledged for allowing me to use their sputtering systems for gold coating.

My heartfelt thanks are due to Srirang-Joan in Haaksbergen, The Netherlands. They always prepared me for European culture and life style. Srirang always motivated and acted as inspiration since my IISc days. I enjoyed the kind hospitality of Murug-Santhiya at Münster, Vinodh and Harish in Stuttgart, Germany.

Having landed in a completely new world I was looking for an Indian with whom I can feel at home. At that time I was introduced to Sudhir and Sangeeta who helped me in every way to settle down. Thanks for wonderful weekends with delicious food that savored my taste buds.

My stay here wouldn't have been never pleasant without emotional support from lovely, fun loving, caring Indian friends Divya-Anurag, Richa-Ratnesh, Nidhi-Vivek, Rejina-Sudip, Brinda-Srijit, Sourabh-Shampa, Abhi-Sachin, Jhanvi-Jenish, Rupa-Vinay, Akshata-Shantanu, Sham, Prasad, Abi, Nav, Deepti, Gauri-Deepak, Pijush, Senthil, Shivaraman, Kavita-Dinesh, Radhi-Bala, Arundhati, Ago-Srinjoy and Charu-Mayank. I will cherish my special friendship with Manju and Sourabh for having every variety of character among three of us. Special thanks to Nidhi for carefully correcting some of the chapters inspite of her busy schedule. Birthday parties, gruppen house stays, dancing, singing and various adventures are sweet memories of my stay in Switzerland. Shilpa-Satheesh-Rithvik, Yashosa-Niranjana-Lalima, Annapoorna-Varma-Divya-Navya, Hyma-Sreedhar-Greeshma, Sridevi-Ramanand-Srikar, Anita-Srinivas, Anu-Sudhakar, Nitya-Jagadish, Banala are the very people who spoke my tongue to make me feel at home. I will never forget in my life for the very care you all have shown me when I was hospitalized for my knee operation. You never allowed me feel alone or miss my family. I wish you a successful career and a contented life. Many thanks also goes to Dr. DeSouza family for their wonderful hospitality. The knowledge they shared and the parental kind of care they showed reflects their beautiful heart.

It was like a story in a movie when I met Ms. Sabrina Steinmann in the aircraft during my return to Switzerland after my holidays in Hyderabad. She was sitting beside me and we struck a conversation only to become very good friends now. Thank you very much for your Easter bunny and your participation in Holi celebrations. I wish you a happy life ahead.

My old contacts kept going with Girish, Ramesh, Bachi, Pammi, Chandru, TC, Narsi and Kalyan. No longer are we living in the same city but still we always have many fun filled moments over emails. Thanks for keeping me in the thread and your support. Wishing you success in your endeavors.

My heartfelt thanks are due to my very special childhood friends Sham, Sridhar and Ramesh. Your phone calls and mails have made some of my days staying so far away from home. I wish you a contented life ahead.

I wouldn't have been successful in this endeavor without the blessings of my parents. They always stood by me as pillars of support and affection. The success of my doctoral studies is a dream come true for my parents. I am very happy to make them proud. Without you I wouldn't be where I am now or even who I am. Abundant love, affection and care from my brothers and sisters-in-law is a boon for me. Delicate Namrata, clever Aarti, sporty Lavanya and soccer freak Shiva always made my day whenever I spoke to

them. Lots of love and best wishes for your bright future. Many thanks goes to Reshmi for being with me and encouraging at every phase. I never imagined in my life that I will ever meet such a wonderful person like you. Your achievements are my motivation; your love and support is everything for me.

Finally, I would like to thank wonderful atmosphere and camaraderie of Basel people who made me fell head over heels in love with this city. I never had any problem during my stay here. It was more than comfortable enjoying the nature's beauty, quality living and working in the frontiers of research. The value addition I got in Switzerland has made me an important person. I started my adventures in cricket, badminton, skiing and photography here. I have many lessons and memories to carry back home. Thanks to everyone for everything.

ABSTRACT

Nanomechanical cantilevers have been proved as extremely sensitive time resolved mass and surface stress sensors. Recent demonstration of zepto gram (10^{-21} grams) sensitivity in vacuum and label free detection of human RNA biomarkers in the total background of cellular RNA at pM range are the unprecedented achievements with these sensors. However, using them as mass sensors in liquid has always been a great challenge. This thesis describes the successful attempt in resonating microcantilevers in liquid and using them as quantitative mass sensors for biological applications. Furthermore, simultaneous measurement of mass sensing and surface stress sensing provides a unique system which can detect multistep and multiprocess systems in biology without any labels.

The Instrument

Chapter 1 describes the present status of these sensors in various fields. A review of interesting experiments performed by various researchers is presented. In **Chapter 2** a detailed description of the setup which uses a tiny liquid chamber of $6 \mu\text{l}$ to hold a microcantilever array is given. Working principles of various parts and mathematical description of basic operating modes are also discussed. Importance of laser beam diameter for detection and a model test result of simultaneous stress and mass sensing are given in the results section.

Higher modes of vibration increase mass sensitivity

Operating the microcantilevers at higher modes increases mass sensitivity by at least two orders of magnitude. This is demonstrated by uniformly deposited gold layers on the cantilevers (see **Chapter 3**). A sensitivity increase of $940 \text{ ag/Hz}/\mu\text{m}^2$ at mode 1 to $8.6 \text{ ag/Hz}/\mu\text{m}^2$ at mode 7 under ambient conditions has been proved. The limitation of mass load with cantilever thickness is dealt in detail.

Resonating microcantilevers in liquid

In **Chapter 4**, a frequency spectrum with clear well resolved resonance peaks for 16 flexural modes of vibration in liquid is presented. The increase in quality factor with mode number is shown. The predicted frequency values from theoretical models and the estimated added apparent mass due to liquid on the resonating cantilever at various modes are compared. The independent effect of density and viscosity at various modes of vibration is discussed in **Chapter 5**. A distinguishable difference between peak frequency and eigen frequency is revealed in the plots.

Mass measurement of latex beads in liquid

A test system based on binding of biotin labeled latex beads to the streptavidin functionalized cantilever for measurement of mass sensitivity is described in **Chapter 6**. The increase in mass sensitivity at higher modes even in liquids is clearly demonstrated. A total of 7 ng was detected with a resolution of 1 ng.

Quantitative biological measurements

In **Chapter 7** quantitative measurement on real time biological system is presented. A new functionalization technique based on inkjet spotting was used to immobilize 2D crystals of reconstituted FhuA transmembrane proteins. FhuA functionalized cantilevers were found sensitive to detect the binding of ligands T5 phage virus particles (10^{-17} g) and ferrichrome molecules (700 Da).

Detecting multistep and multivariant biological system

An experiment demonstrating the capability of the system to perform simultaneous mass sensing and stress sensing is described in **Chapter 8**. The mass measurement plots reveal that only monolayer formation of lipid vesicles occurs. A multistep experiment with initial vesicle adsorption and subsequent binding of bee venom protein (melittin) demonstrates measurements in different mass ranges. Simultaneously, tensile stress on the cantilever due to vesicle adsorption and the subsequent compressive stress owing to the pore formation of melittin in the immobilized vesicles are observed in the deflection plot. Finally **Chapter 9** concludes summarizing all the results obtained.

CONTENTS

| | | |
|----------|---|-----------|
| 1 | Introduction | 1 |
| 1.1 | Nanomechanical microcantilever as a sensor | 1 |
| 1.1.1 | Static mode | 3 |
| 1.1.2 | Dynamic mode | 3 |
| 1.1.3 | Heat mode | 4 |
| 1.2 | Evolution of microcantilever sensors | 4 |
| 1.3 | Scope of the present thesis | 7 |
| 2 | The Instrument | 9 |
| 2.1 | Introduction | 9 |
| 2.2 | Sensor setup | 9 |
| 2.2.1 | Microcantilever sensing system | 9 |
| 2.2.2 | Fluid flow system | 12 |
| 2.2.3 | Detection System | 14 |
| 2.2.4 | Control and Analysis | 15 |
| 2.3 | Gold Coating | 18 |
| 2.4 | Functionalization | 20 |
| 2.4.1 | Capillary technique | 20 |
| 2.4.2 | Inkjet spotting | 22 |
| 2.5 | Modes of operation | 23 |
| 2.5.1 | Static Mode | 23 |
| 2.5.2 | Dynamic Mode | 24 |
| 2.5.3 | Combined mode | 26 |
| 2.6 | Results and Discussion | 26 |
| 2.6.1 | Characterization of PSD | 26 |
| 2.6.2 | Simultaneous measurement of dynamic and static mode | 27 |
| 2.7 | Conclusion | 31 |
| 3 | Higher modes of vibration increase mass sensitivity | 32 |
| 3.1 | Introduction | 32 |
| 3.2 | Experiment Details | 33 |
| 3.2.1 | Preparation of the cantilevers | 33 |
| 3.2.2 | Setup | 33 |
| 3.3 | Theory | 35 |
| 3.3.1 | Resonance frequency | 35 |
| 3.3.2 | Calculation of mass | 36 |
| 3.4 | Results | 36 |
| 3.4.1 | Visualization of resonance modes | 36 |
| 3.4.2 | Frequency Spectra | 37 |

| | | |
|----------|---|-----------|
| 3.4.3 | Calibration | 37 |
| 3.4.4 | Frequency shift for mass loading | 41 |
| 3.4.5 | Higher harmonics offer better sensitivity | 42 |
| 3.5 | Discussion | 42 |
| 3.6 | Conclusions | 45 |
| 4 | Resonance frequencies of cantilever array vibrating in liquid | 46 |
| 4.1 | Introduction | 46 |
| 4.2 | Results | 47 |
| 4.3 | Discussion | 49 |
| 4.4 | Conclusion | 55 |
| 5 | Rheological effects of liquid on resonating nanomechanical microcantilevers | 57 |
| 5.1 | Introduction | 57 |
| 5.2 | Materials and Methods | 58 |
| 5.3 | Results | 60 |
| 5.4 | Discussion | 63 |
| 5.5 | Conclusion | 64 |
| 6 | Binding kinetics of latex beads by biomolecular interaction in physiological environment | 65 |
| 6.1 | Introduction | 65 |
| 6.2 | Theory | 66 |
| 6.3 | Experimental Details | 69 |
| 6.3.1 | Measurement Setup | 69 |
| 6.3.2 | Cantilever Functionalization | 70 |
| 6.3.3 | Binding assay | 70 |
| 6.3.4 | Data analysis | 70 |
| 6.4 | Results | 72 |
| 6.4.1 | System characterization | 72 |
| 6.4.2 | Binding assays | 72 |
| 6.5 | Discussion | 80 |
| 6.6 | Conclusions | 82 |
| 7 | T5 phage virus binding to FhuA membrane protein | 83 |
| 7.1 | Introduction | 83 |
| 7.2 | Materials and Methods | 84 |
| 7.2.1 | FhuA preparation | 84 |
| 7.2.2 | Functionality assay | 85 |
| 7.2.3 | Functionalization | 85 |
| 7.2.4 | Characterization of functionalization | 86 |
| 7.2.5 | Binding assay | 86 |
| 7.2.6 | Data processing | 89 |
| 7.3 | Results and Discussion | 89 |
| 7.3.1 | Receptor preparation and protein functionality tests | 89 |
| 7.3.2 | Functionalization of cantilevers | 91 |
| 7.3.3 | Binding experiments | 91 |
| 7.4 | Conclusion | 95 |

| | | |
|----------|---|------------|
| 8 | Detection of multistep process in biosystems: Combined static and dynamic mode | 96 |
| 8.1 | Introduction | 96 |
| 8.2 | Materials and Methods | 97 |
| 8.3 | Results | 99 |
| 8.4 | Discussion | 101 |
| 8.5 | Conclusions | 103 |
| 9 | Conclusions and Outlook | 104 |

CHAPTER 1

INTRODUCTION

"Some ideas evolve and some ideas breakthrough and change everything." – Lexus

The invention of the scanning tunnelling microscope 25 years ago, followed by the atomic force microscope a few years later, were crucial events in the history of nanoscience and nanotechnology ((Binnig et al., 1982, 1983, 1986)). In the years that followed the excitement lead to the demonstration of using an STM to spell out IBM with xenon atoms on a nickel surface and moving iron atoms on a copper surface to construct a quantum corral (Eigler & Schweizer, 1990; Manoharan et al., 2000). Since its invention in 1986 (Binnig et al., 1986), the atomic force microscope (AFM) has proved its suitability in various fields of application. First designed as an instrument to image the surfaces of nonconductive materials with high lateral and vertical resolution, the technique has been adapted for various environments, such as vacuum, ambient, fluidics, low temperatures and magnetic fields, as well as for chemistry and biology applications. The capability to investigate surfaces with unprecedented resolution using the techniques of scanning probe microscopies introduced a wealth of related techniques using probes with local interaction (see Fig. 1.1), after (Gerber & Lang, 2006).

Another breakthrough occurred in 1994 when scientists have utilized the surface of AFM cantilevers as heat sensor (Gimzewski et al., 1994; Thundat et al., 1994). It was a major step to exploit the unprecedented potential in using microcantilevers for sensing applications. In the following years its application into various fields has opened doors to a whole new field of nanomechanical chemical/biosensing.

1.1 Nanomechanical microcantilever as a sensor

The surface of the microcantilever can be used as a platform to perform experiments whose effects can be determined by monitoring temporal changes in its extremely sensitive nanomechanical properties. Cantilevers can be used as a nanomechanical sensor device for detecting chemical interactions between binding partners on the cantilever surface and in its environment. Such interactions might be produced by electrostatic or intermolecular forces. At the interface between an active cantilever surface and the surrounding medium, the formation of induced stress, the production of heat or a change in mass can be detected. In general, one of the binding partners is placed on a cantilever, while the other binding partners are present in the environment. Figure. 1.2 shows the variety of detection modes using such cantilever sensors. We distinguish three main sensor types: static mode, dynamic mode and heat mode.

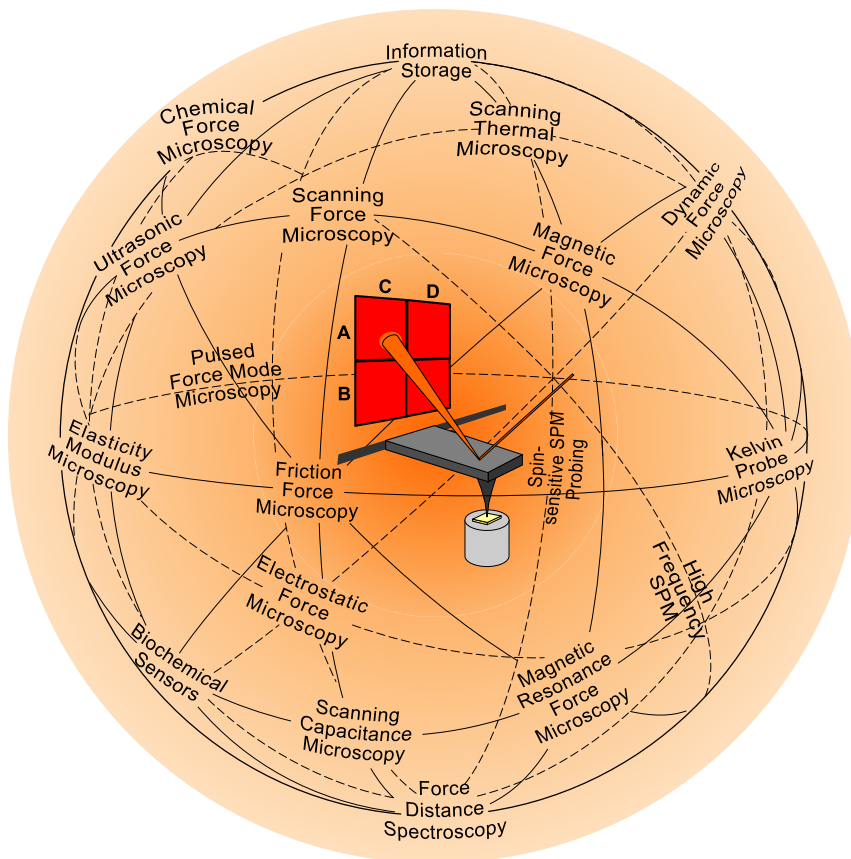


Fig. 1.1: World of possibility in the AFM universe. The AFM (centre) has inspired a variety of other scanning probe techniques. Originally the AFM was used to image the topography of surfaces, but by modifying the tip it is possible to measure other quantities (for example, electric and magnetic properties, chemical potentials, friction and so on), and also to perform various types of spectroscopy and analysis.

1.1.1 Static mode

In the static mode the static bending of the cantilever beam due to external influences and chemical/physical reactions on one of the cantilever's surfaces is investigated (see left column of Fig. 1.2). The asymmetric coating with a reactive layer on one surface of the cantilever favors preferential adsorption of molecules on this surface. In most cases, the intermolecular forces in the adsorbed molecule layer produce a compressive stress, i.e. the cantilever bends down if its reactive surface is its upper one. If the reactive layer is a thin layer of polymer, molecules from the environment will diffuse into the polymer layer and cause it to swell, resulting also in a downward bending of the cantilever. Finally, in liquid or biochemical environments, we can observe a downward bending of the reactive cantilever surface when molecular recognition reactions are taking place on the functionalized surface of the cantilever. Processes such as electrostatic repulsion between adsorbed biomolecules or steric effects due to the fact that the adsorbed molecules require additional space on the surface are responsible for the formation of compressive stress on cantilevers in fluidics. (Wu, Ji, et al., 2001).

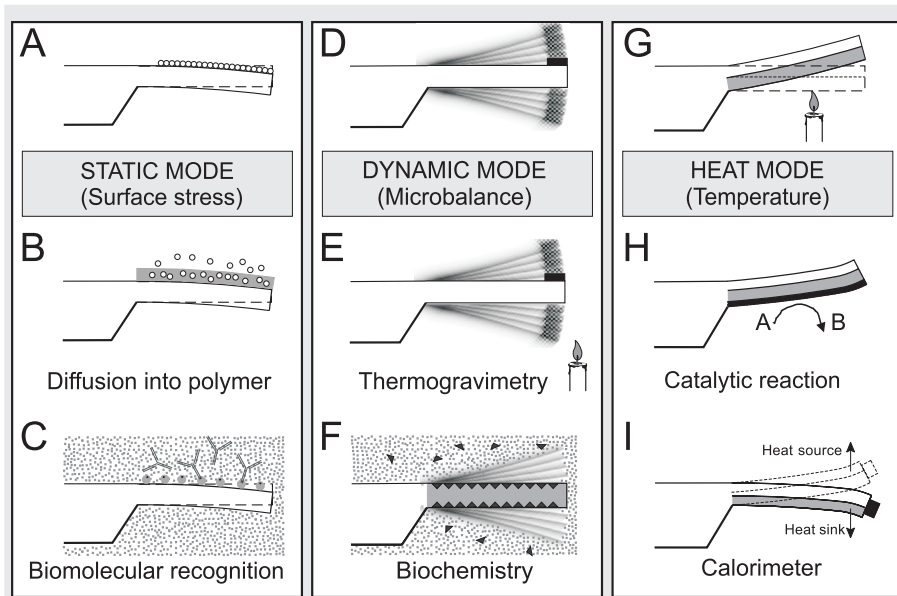


Fig. 1.2: Basic sensing techniques of the cantilever sensor

1.1.2 Dynamic mode

In the dynamic mode the cantilever is driven at its resonance frequency (see the middle column of Fig. 1.2). If the mass of the oscillating cantilever changes owing to additional mass deposited on the cantilever, or if mass is removed from the cantilever, its resonance frequency changes. Using electronics designed to track the resonance frequency of the oscillating cantilever, the mass changes on the cantilever are derived from shifts in resonance frequency. The cantilever can be regarded as a tiny microbalance, capable of

measuring mass changes of about 1 zg (10^{-21} g) (Yang et al., 2006). If a biochemically active layer is deposited onto the surface of a cantilever, the mass change during molecular recognition reactions can be observed directly using the oscillating cantilever technique. However, oscillating a cantilever in liquids results in a very low quality factor.

1.1.3 Heat mode

In the heat mode the cantilever is coated asymmetrically on one surface with a layer having different thermal expansion properties than those of the cantilever material. Suitable materials for coating silicon cantilevers are, for example, aluminium or gold, because their thermal expansion coefficient is much larger than that of silicon. If such a cantilever is subjected to external temperature changes it will bend due to the differing thermal expansion coefficients of the cantilever material and the coating layer. Deflections corresponding to temperature changes in the microkelvin range can be measured easily. The coating layer can also be catalytically active, e.g. a platinum layer facilitates the reaction of hydrogen and oxygen to form water. In this case, heat is directly generated on the surface of the cantilever, which causes the cantilever to bend owing to the differing thermal expansion coefficients of silicon and platinum. The cantilever surface can also be used as a platform to perform thermal experiments.

1.2 Evolution of microcantilever sensors

Nanomechanical microcantilever sensors have proved their capability in various fields as shown in Fig. 1.3.

The first demonstration of exothermic *chemical* reactions of 1 pJ was reported by (Gimzewski et al., 1994) in the heat mode. Thermal analysis of phase transitions with a short response time of 1 ms was performed (Berger et al., 1996). Subsequently, surface Stress in the self-Assembly of alkanethiols on gold was measured (Berger et al., 1997; Fritz, Baller, Lang, Strunz, et al., 2000). A detailed study into the molecular basis of stress generation in aqueous environments focusing on the pH titration of model mercaptohexadecanoic acid self-assembled monolayers (SAMs), using in situ reference cantilevers coated with nonionizable hexadecanethiol SAMs was performed: a differential surface stress of $+1.2 \pm 0.3$ mN/m at pH 6.0, corresponding to 1 pN attractive force between two adjacent MHA molecules was measured (Watari et al., 2007). The interest and excitement of successful chemical sensors has led to the application as a *artificial NOSE*. A polymer coated micromechanical cantilever array was used to identify gases and vapors (Lang, Berger, Battiston, et al., 1998). The concept of using arrays instead of single cantilevers had an advantage of doing multiple sensing using differently functionalized cantilevers. Furthermore including a control cantilever sensor among many sensor cantilevers resulted in more reliable and robust results. The response pattern for perfume essence using eight cantilevers was analyzed via principal component analysis and artificial neural network. The artificial NOSE was further developed to do simultaneous resonance frequency and binding readout enabling to measure physical and chemical process simultaneously (Battiston et al., 2001; Baller et al., 2000)

DNA hybridization of oligonucleotides with complementary oligos immobilized on the microcantilever surface has translated biomolecular recognition into nanomechanical bending of the microcantilever, hence starting their applications in *genomics*. A single base mismatch between two 12-mer oligonucleotides was clearly detectable (Fritz,

Baller, Lang, Rothuizen, et al., 2000). Subsequently, cantilever arrays permitted multiple binding assays in parallel and detect femtomoles of DNA on the cantilever at a DNA concentration in solution of 75 nM (McKendry et al., 2002). Latest development in this direction is detection of mRNA biomarkers in total cellular RNA. Differential gene expression of the gene 1-8U, a potential marker for cancer progression or viral infections, has been observed in a complex background. The measurements provided results within minutes at the picomolar level without target amplification, and are sensitive to single base mismatches (J. Zhang et al., 2006).

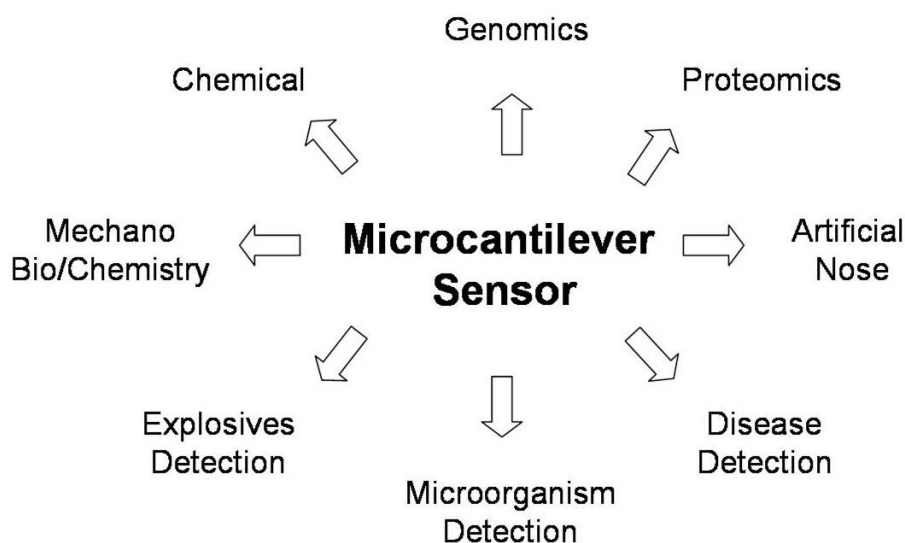


Fig. 1.3: Applications of the microcantilever sensors

Transducing biomolecular recognition in experiments on protein A-immunoglobulin interactions has hinted their application possibility in *proteomics* (Fritz, Baller, Lang, Rothuizen, et al., 2000). Two forms of prostate-specific antigen (PSA) over a wide range of concentrations from 0.2 ng/ml to 60 $\mu\text{g/ml}$ in a background of human serum albumin (HSA) and human plasminogen (HP) at 1 mg/ml was detected, making this a clinically relevant diagnostic technique for prostate cancer (Wu, Datar, et al., 2001). Because cantilever motion originates from the free-energy change induced by specific biomolecular binding, this technique may offer a common platform for high-throughput label-free analysis of protein-protein binding, DNA hybridization, and DNA-protein interactions, as well as drug discovery. Use of cantilever arrays permitted detection of up to seven different antigen-antibody reactions simultaneously, including an additional thermomechanical and chemical in situ reference. A continuous label-free detection of two cardiac biomarker proteins, creatin kinase and myoglobin at a sensitivity of 20 $\mu\text{g/ml}$ (Arntz et al., 2003) was another proof of their applicability. Recent development in this direction being enhancing the sensitivity of microcantilevers as immunosensors using single-chain Fv (scFv) antibody fragments as receptor molecules. Including the decrease in thickness of the microcantilevers, their sensitivity was increased to 1 nM concentration of antigen molecules (Backmann et al., 2005). With the independently progress in DNA and protein detection, an interesting experiment on transcription

factors involving protein interaction with double-stranded DNA oligonucleotides was performed. The transcription factors SP1 and NF- κ B were detected independently at concentrations of 80 to 100 nM. The experiments show that the recognition sequence of one transcription factor can serve as a reference for the other, highlighting the sequence specificity of transcription factor binding (Huber et al., 2006).

Conformation changes in molecules is associated with mechanical changes in the molecules resulting in *mechano bio/chemical* reactions. Microcantilevers modified by a monolayer of azobenzene molecules bend up and down periodically, switched by 365 nm UV light, as a result of conversion of the two configurations of azobenzene molecules in the monolayer (Ji et al., 2004). In biology, interaction of ligands to membrane proteins can result in their conformation change and signalling subsequent actions inside the cell. A membrane preparation containing 5-HT(3AS) receptors was used to modify a microcantilever. The modified microcantilever was found to bend on application of the naturally occurring agonist (5-hydroxytryptamine, which is also called serotonin) or the antagonist MDL-72222, but not to other similar molecules. These results suggest that the microcantilever system has potential for use in label-free, drug screening applications (Y. Zhang et al., 2004). For detection of ligand protein interaction and conformational changes of membrane proteins, the bacteriorhodopsin (bR) model system was tested. This membrane protein is responsible for the photon-driven transport of protons across the purple plasmamembrane of *Halobacteria salinarum*. Prosthetic retinal removal (bleaching) of the bacteriorhodopsin protein was successfully detected by measuring the induced nanomechanical surface stress change (T. Braun et al., 2006). Piezoresistive cantilevers were also used to measure specific protein conformations at the nanoscale level at injection concentration of 2.5-20 nM binding protein (Mukhopadhyay et al., 2005). Microcantilevers were also used to measure nanoscale motion of synthetic DNA motors via controlled conformational change. The forces exerted by the precise duplex to nonclassical i-motif conformational change were probed via differential measurements using an in-situ reference cantilever coated with a nonspecific sequence of DNA. Fueled by the addition of protons, the open to close stroke of the motor induced 32 ± 3 mN/m compressive surface stress, which corresponds to a single motor force of approximately 11 pN/m, an order of magnitude larger than previous classical hybridization studies. Motor-induced cantilever motion was tuneable via control of buffer pH and ionic strength, indicating that electrostatic forces play an important role in stress generation. Hybrid devices which directly harness the multiple accessible conformational states of dynamic oligonucleotides and aptamers, translating biochemical energy into micromechanical work, present a radically new approach to the construction of smart nanoscale machinery and mechano-biosensors (Shu et al., 2005).

Micromechanical oscillators were used as rapid biosensor for the detection of active growth of *Escherichia coli* leading to their application in *microorganism detection* (Gfeller et al., 2005a,b). Micromechanical oscillators were coated with common nutritive layers to grow them. The change in resonance frequency as a function of the increasing mass on a cantilever array forms the basis of the detection scheme. The calculated mass corresponded to the sensitivity of approximately 1000 *Escherichia coli* cells in 1 h. The results allow future applications in, e.g., rapid antibiotic susceptibility testing. They were also demonstrated for selective fungal immobilization and fast growth detection. An antibody-sensitized microcantilever were tested for the growth detection of *aspergillus niger* Spores (Nugaeva et al., 2005, 2007).

Demonstration of adsorption of trinitrotoluene (TNT) on a silicon cantilever that was coated with a self-assembled monolayer (SAM) of 4-mercaptobenzoic acid on one

surface showed its capability to detect *explosives*. This study shows that microcantilevers provide a convenient and versatile platform for the monitoring of molecular binding to SAMs (Pinnaduwaage et al., 2003).

To use cantilevers as sensors, throughput depends heavily on the functionalization efficiency. Widely used techniques are capillary based, ink jet spotting and electrochemical methods (Bietsch, Zhang, et al., 2004; Bietsch, Hegner, et al., 2004).

The main drawback of static mode sensing is that it needs the collective effect of many molecules to show some signal. Furthermore it doesn't account for the number of molecules contributing to a particular effect. Operating the sensor in dynamic mode offers a solution to this case. Measurement of mass allows to measure the number of molecules involved. Dynamic mode sensing was for the first time demonstrated by detection of mercury vapor using resonating microcantilevers (Wachter & Thundat, 1995). Subsequently, the dehydration reaction of copper sulfate pentahydrate into water-free copper sulfate upon heating was investigated on a sample mass of few micrograms by thermogravimetry. A small amount of sample material was attached to the apex of the cantilever, the response of that piece of material as a function of the thermal programme imposed was investigated (Berger et al., 1998). Some groups have fabricated ultrasensitive nanomechanical cantilevers capable of detecting atto gram (Ilic, Craighead, et al., 2004) and zepto gram (Yang et al., 2006) sensitivities of mass. Different structures were also implemented to increase their sensitivities (Craighead, 2000), (Ekinici et al., 2004), (Ekinici & Roukes, 2005). Single virus detection was demonstrated using these sensitive mass detectors (Gupta et al., 2004; Ilic, Yang, & Craighead, 2004). Recently an interesting design of hollow cantilevers which can work in vacuum with samples flowing in these hollow space was able to detect a mass resolution of 1 ag. It has a scope to weigh biomolecules, single cells and single nanoparticles in fluid while the cantilever itself is working in vacuum for better Q values (Burg et al., 2007). Microcantilever based mass sensors showed enhanced functionality using higher modes (Dohn et al., 2005). Highly sensitive polymer-based cantilever-sensors for DNA detection were also attempted (Calleja et al., 2005). Nanocantilevers from other materials like aluminum were also fabricated for high sensitivity mass sensors (Zachary & Boisen, 2005).

All the above mentioned literature indicates that there was hardly any attempt to use these cantilever sensors operated in dynamic mode in liquid. It is a challenging task to vibrate a cantilever array in liquid environment. Successful operation requires efficient coupling of external excitation energy to the cantilevers avoiding anomalous additional acoustic frequencies originating from liquid chamber. It also needs a bubble free fluid flow system, optimally focussed parallel laser beams and sufficient laser power to pass through air-liquid-air interface for optical detection of cantilever motion. However, recent results on nanomechanical sensing in liquid was focussed on the physics of boundary streaming near an oscillating surface (Dorrestijn, 2006; Dorrestijn et al., 2007). The focus of the present thesis is on further understanding of dynamic mode operation of microcantilever in liquid towards biological applications.

1.3 Scope of the present thesis

This thesis describes resonating nanomechanical microcantilevers for quantitative biological measurements in liquid. It starts with a detailed description about the setup that was developed to perform both static and dynamic mode detection simultaneously. The sensitivity increase with mode number for a distributed mass load and the limitation of overlaid thickness at which spring constant effect begins is analyzed. Then a clean complete spectrum of resonance modes of a vibrating cantilever in liquid is presented.

Mode numbers were clearly distinguished and matched with various theories available in the literature. The experimental results on highly debated effect of viscosity on the resonance frequency value has opened new questions about its dependency. As a test experiment to demonstrate mass measurements in liquid and higher harmonics contribute to higher sensitivity was done with bio-functionalized latex beads binding to its receptor molecules immobilized on the cantilever. Real time binding experiments of virus docking on to specific immobilized membrane protein is demonstrated. Finally, multi step binding and dual process of mass change and surface stress are detected sequentially and simultaneously in a single experiment.

CHAPTER 2

THE INSTRUMENT

"You have to have confidence in your ability, and then be tough enough to follow through." – Rosalynn Carter

This chapter describes the experimental setup designed and developed for simultaneous measurement of static and dynamic mode signal from a vibrating nanomechanical cantilever array sensor in liquid. The major parts of the setup such as fluid flow system, laser beam deflection technique and fluid cell are considered in detail. Specific information on different parts of the system for ultimate measurement of stress from static and mass from dynamic are given in the results section. The essential issues to be understood and implemented are design of a fluid chamber volume of $6 \mu\text{l}$, importance of laser beam diameter, clean resonance spectrum, higher sensitivity at higher harmonics, simultaneous measurement of static and dynamic mode.

2.1 Introduction

2.2 Sensor setup

The entire setup is divided into four blocks: sensing system, fluid flow system, detection system, and control & analysis system (Fig. 2.1). The sensing system constitutes an array of 8 microcantilevers and the fluid chamber holding it. The fluid flow system selects the chosen fluid and its rate of flow through the fluid chamber. Laser beam detection system is used to measure the nanomechanical deflections of the microcantilevers. The electronic interface system controls air pressure in the fluid flow system, as well as signal processing and receives signals from the detector system. NOSETools software written in IGOR Pro is used to analyze the frequency response of the resonating cantilever and their corresponding static deflections. Detailed schematics of the setup are shown in Fig. 2.2.

2.2.1 Microcantilever sensing system

Microcantilever is a sub-millimeter-sized beam like structure which is fixed at one end and free to move at the other end. Usually its length \gg width \gg thickness. Owing to tiny inertial mass it is extremely sensitive to its various physical parameters like mass, spring constant and deflection, which can be monitored from changes in its nanomechanical properties. Mass and spring constant are determined by monitoring its resonance

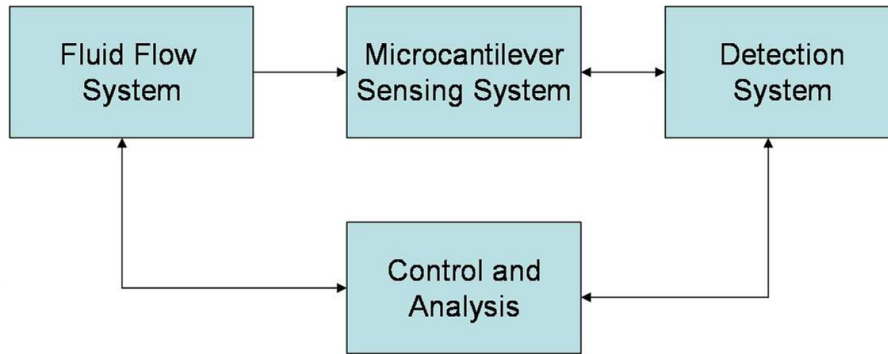


Fig. 2.1: Block diagram of the setup

frequency and deflection from bending of the beam. For biological applications sensor is operated in liquid. The use of cantilever array renders much more reliable results and is more efficient because several experiments can be performed at the same time.

Cantilever Array Sensor

Scanning electron microscope (SEM) images of the cantilever sensor array used are shown in the Fig. 2.3. They were microfabricated at the Micro and Nanomechanics group, IBM Zurich research laboratory in Rüschlikon, Switzerland. Each chip consists of eight cantilevers at a pitch of $250\ \mu\text{m}$. The dimensions of the cantilevers are $500\ \mu\text{m}$ in length and $100\ \mu\text{m}$ in width. Different thicknesses of $7\ \mu\text{m}$, $4\ \mu\text{m}$, and $1\ \mu\text{m}$ have been investigated. The cantilever arrays of $7\ \mu\text{m}$ and $4\ \mu\text{m}$ thick were wet etched out of Si wafer while $1\ \mu\text{m}$ thick cantilevers were dry etched out of Silicon on Insulator (SOI) wafer. For their resonance frequencies and spring constant values see chapter 3.

Liquid chamber

Four different mechanical parts including a clamp (to hold the cantilever chip) made of polyetheretherketone (PEEK) material are assembled together to form a liquid chamber of $6\ \mu\text{l}$. PEEK is a grey, opaque, biologically inert, electrically insulating, easy machinable and high temperature resistance semi crystalline high purity polymer material. A U-shaped structure made of glass which can slide in machine-cut groves of PEEK closes the chamber. A cross-sectional view of the chamber is shown in Fig. 2.4A. The cantilever array chip is placed inside the chamber at an angle of 45° with respect to the chamber walls to avoid influence from reflection of waves if any. The excitation energy for the cantilevers to vibrate is provided by an external piezo. A PZT-5A piezo material of industry type obtained from Olympus NDT Inc., USA, Model EBL2 with d_{33} electromechanical coefficient of $380 \times 10^{-12}\ \text{m/V}$ was used. A sinusoidal excitation energy of $10\ \text{V}_{p-p}$ is applied to the piezo. The clamp holds the cantilever chip body placed directly on the piezo by keeping only the cantilever array inside the chamber (Fig. 2.4B) and rest of the chip body outside. The piezo directly beneath the array chip body ensures good energy transfer. Laser beam enters through one wall of the glass window (clamp side) and gets reflected at the apex of the cantilever taking an angle of 90° and

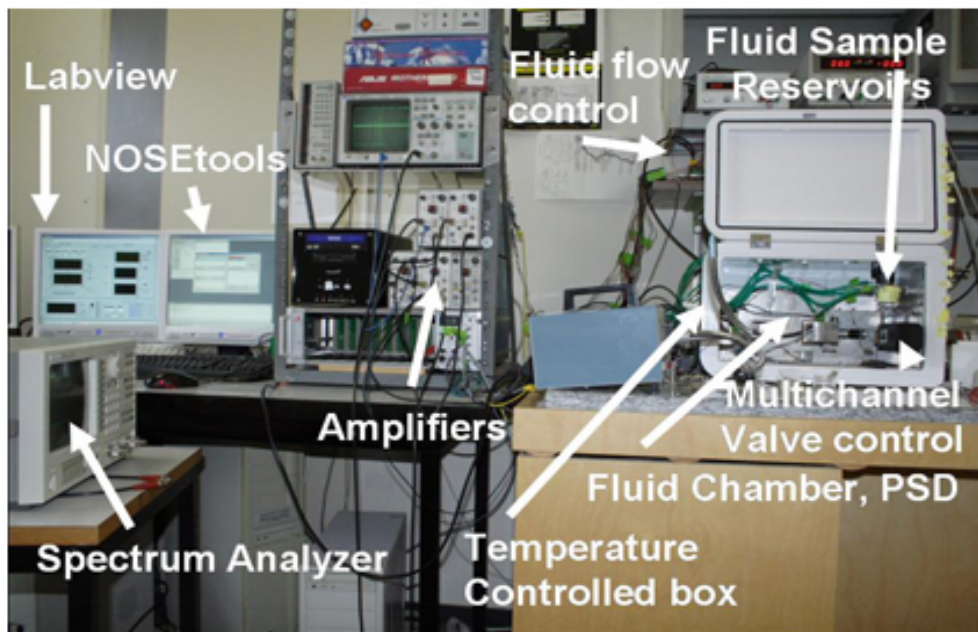
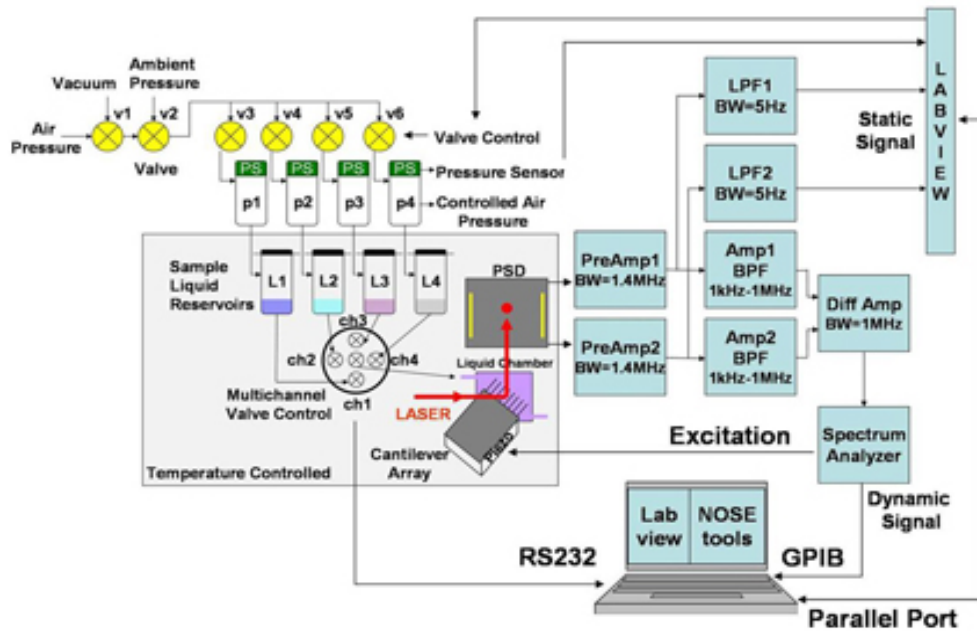


Fig. 2.2: Top: Schematic diagram of the setup. Bottom: Photograph of the setup

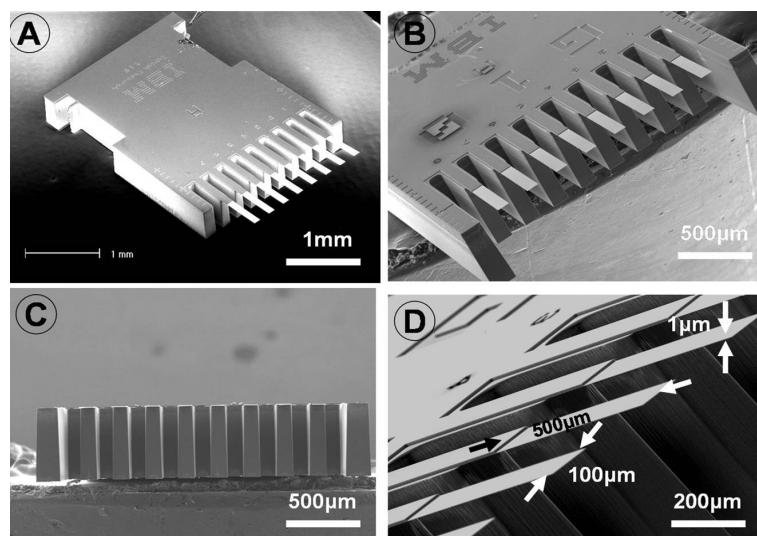


Fig. 2.3: (A) First design of Cantilever array; (B) Solid bars included on either side of CLA; (C) Front view; (D) Cantilever attached to a hinge

exits from top glass wall of the chamber. The entrance and exit of the laser beam to the chamber is perpendicular to the glass surface thus avoiding any virtual deflection artifacts due to refractive index change between air/glass/liquid interface. The fluid cell also has a 100 ohm resistive element (peltier) embedded near the chamber acts as a source for heat test. It is performed to check the mechanical properties (calibration) of the cantilevers and check their uniformity (J. Zhang et al., 2006). The assembled parts forming a liquid chamber is shown in the Fig. 2.4C.

2.2.2 Fluid flow system

Sample liquid is placed in glass vial reservoirs of each 3 ml in capacity with a nozzle at the bottom which is connected to the liquid chamber Fig. 2.2 and Fig. 2.4C. At present liquid from 4 different vials can be injected. Air pressure maintained over the liquid inside the vials control the liquid flow rate through the chamber. The required value of pressure is maintained by carefully controlling air and vacuum through pressure valves (Fig. 2.5). In all the experiments, a pressure of about 15 mbar resulting in a flow rate of $12 \mu\text{l}/\text{min}$ was maintained. However, the flow rate can be controlled between a minimum of $5 \mu\text{l}/\text{min}$ and maximum of $30 \mu\text{l}/\text{min}$ with a resolution of $0.2 \mu\text{l}/\text{min}$. The diameter of the teflon tubing used to carry the liquid from reservoirs to liquid chamber is $180 \mu\text{m}$ in diameter. Desired sample is allowed to flow using a multichannel valve selector (Fig. 2.2). The advantage of air pressure driven fluid flow system is that the flow of liquid is smooth unlike a syringe pump which works on the stepping angles of stepper motor rotation.

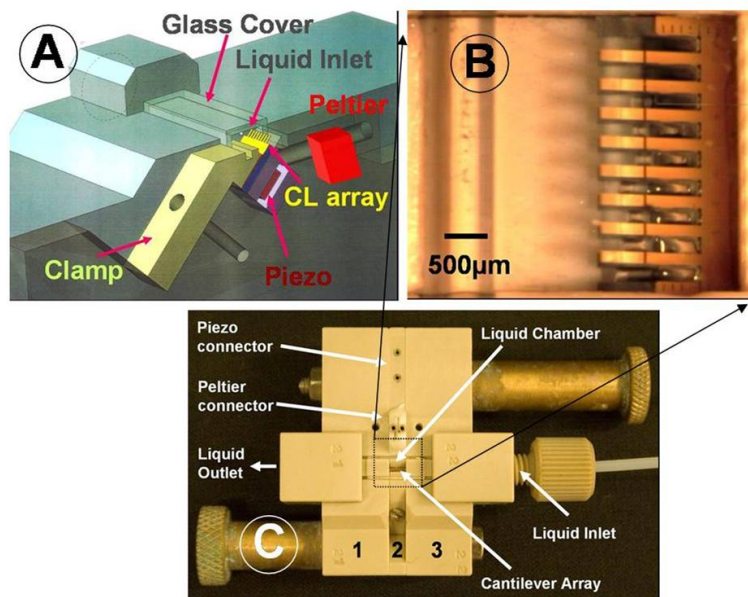


Fig. 2.4: (A) Cross sectional view of the chamber; (B) Liquid chamber with cantilever array mounted; (C) Assembled PEEK parts 1, 2 and 3 forming a chamber

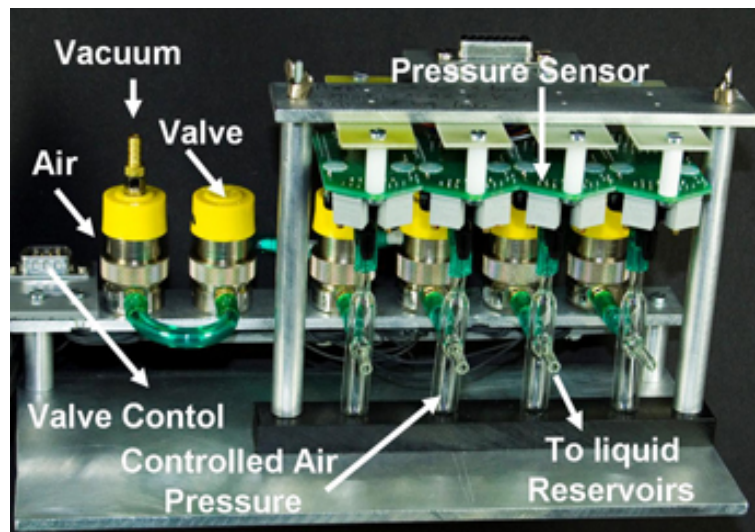


Fig. 2.5: Photograph of the air pressure controlled fluid flow system. Controlled amounts of air overpressure and underpressure are injected through the valves to maintain the pressure required for the desired flow rate. The pressure values in the glass tubes is read by pressure sensors. The outlet of the glass tubes are connected to the liquid reservoirs. In the existing setup four different liquid samples can be allowed to flow through the chamber

2.2.3 Detection System

Laser beam deflection detection technique is in vogue since 1988 (Meyer & Amer, 1988; Jr et al., 1989). It can measure deflections down to sub angstrom level. It is a very simple and elegant technique which exploits the geometrical magnification to achieve the desired sensitivity. In this technique, a laser beam is deflected from the apex of the cantilever and the deflected beam is collected on a light sensitive detector (Miyatani & Fujihiraa, 1997; Hu et al., 2004; Godin et al., 2001; Higgins et al., 2006). The position of the laser spot on the detector is calibrated for the cantilever deflection. It is a completely passive detection system which does not use any electronics to achieve the sensitivity. Considering a non-divergent laser beam, the sensitivity is limited by the distance between the reflecting surface and the light sensitive detector. For an array of eight cantilevers, a time multiplexed sequential readout method was used to read deflections of all the cantilevers (Lang, Berger, Andreoli, et al., 1998). A vertical cavity surface emitting laser array and a position sensitive detector is used to monitor the nanomechanical motion of the cantilevers.

VCSELs

Vertical Cavity Surface Emitting Laser (VCSEL) is a micromachined semiconductor laser which emits light at an angle of 90° with respect to the surface of the substrate. VCSELs of 760 nm wavelength were purchased from Avalon Photonics, Zurich, Switzerland. Light emerges from an aperture on the surface into a cone of light. The solid angle of the cone depends on the aperture size. The smaller the size of the aperture, larger the emission angle. The circular beam typically has a beam diversion of 13° at full width half maxima (FWHM). An additional external lens system consisting of two convex lenses of 35 mm focal length and 12.5 mm diameter placed next to each other were used to focus the laser beams on the apex of the cantilevers. At one focus of the lens system, VCSEL array are placed and on the other focus cantilever array is placed. A pitch of $250 \mu\text{m}$ between each VCSEL in an array of 8 matched exactly with pitch of cantilevers. Lasers were operated in single mode at 5 mA with an average output power of 1.2 mW. The I-V characteristics are shown in the Fig. 2.6.

Position sensitive detector

The PSD (Position Sensing Detector) is an opto-electronic device which can continuously track the position of an incident light spot. PSD (Sitek Partille, Sweden) is purely an analog device relying on the current generated by a photodiode divided in the resistive layer. It gives an output that is a function of the center of gravity of the total light quantity distribution on the active area. The details of the device are given in Fig. 2.7. It has three terminals, two anodes connected on the top side and a cathode on the bottom side. The active area between $X1$ and $X2$ generates photocurrents on light is incident. The amount of current on either sides is determined by the value of the resistance they experience. If $I1$ and $I2$ represent current at $X1$ and $X2$ on a PSD of active length L , the position x of the incident light is given by the equation 2.1. The position of the light spot is independent of intensity magnitude.

$$x = \left(\frac{I1 - I2}{I1 + I2} \right) \frac{L_{psd}}{2}. \quad (2.1)$$

A PSD of $10\text{mm} \times 10\text{mm}$ was used in the setup. Owing to the divergence of the laser beam used, the size of the laser spot reaching the PSD placed at a distance of 38.8

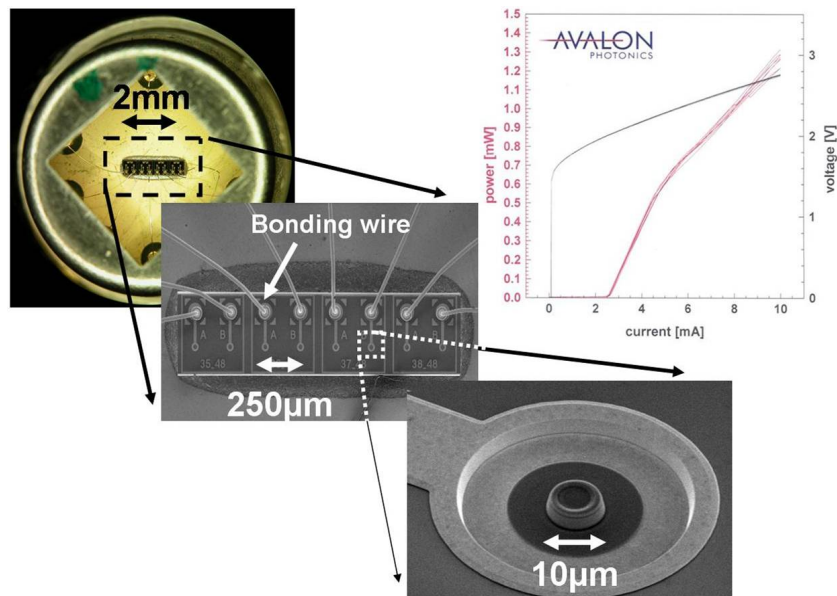


Fig. 2.6: VCSEL array and its characteristics

mm from the cantilever was 7.5 mm in diameter. The response characteristics of the PSD are discussed in detail in the results section.

Later the signals are split to pass through low pass filter of bandwidth 5Hz and wide band pass filter of bandwidth 1kHz to 1MHz (Fig. 2.2). The output of the low pass filter gives the average position of the laser beam on the PSD, which in turn is used to extract the static signal. The output of the wide band pass filter constituting the dynamic signal is given as an input to a network analyzer. It compares the excitation signal with the response signal from the cantilever to give amplitude and phase information. Peaks in the amplitude response corresponds to resonance frequencies of the cantilever.

2.2.4 Control and Analysis

Static and dynamic response data collected is later processed by NOSEtools software program (T. Braun, Huber, et al., 2007). The dynamic data collected are frequency spectra at intervals of 4 sec between each file for every cantilever. The NOSEtools software uses a model to extract resonance frequency, eigen frequency, quality factor, damping factor and also mass adsorbed with time (T. Braun, Barwich, et al., 2005).

Hardware

A labview card PCI 6014 from National Instruments was used to select VCSEL, read signals from PSD, pressure sensor values (GermanyAir Controls GmbH, Kempen, Germany) for flow control, temperature sensor (NTC-SEMI 833 ET, Hygrosens Instruments, Switzerland) to read from inside the box (17 L refrigerator from Interdiscount, Switzerland) encasing the setup. A voltage or current controllable power supply (E 3614A, Hewlett Packard) was used to set the peltier current of the fridge after reading

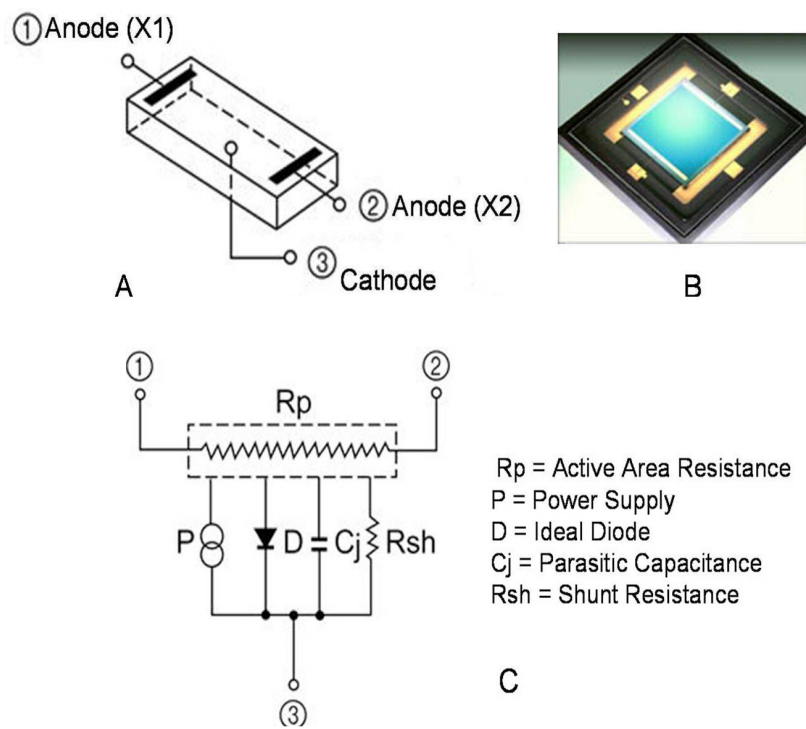


Fig. 2.7: (A) Schematic of the PSD. (B) Photograph of the PSD. (C) Electrical equivalent

temperature signal. A constant current source circuit was used to control laser power of the VCSEL. Another card (NI PCI 6503) with digital ports was used to control air pressure valves (Sensortech, Puchheim, Germany) to the fluid flow system. GPIB interface reads 400 data points (amplitude and phase) from the network analyzer (Hewlett Packard, 4589A, USA) and a RS232 serial port to control a valve selector (Vinci, USA).



Fig. 2.8: Front panel of the combined mode setup. (1) Dynamic mode section, the amplitude spectra and phase spectra read from the spectrum analyzer, with possibility to choose center frequency, span and input excitation power. (2) Static mode section, the sum and difference signal for each signal. Only the signals from one of the cantilevers are displayed at a time. The laser position on the PSD can be visualized. (3) Temperature control of the box encasing the entire setup. (4) VCSEL selection. (5) Fluid flow control panel, by choosing vacuum or air, liquid flow rate can be controlled which is displayed

NOSETools

The unique combination of different measured properties in parallel needs new software for efficient data analysis. In case of dynamic mode data the frequency is not tracked directly by a phase lock loop system (PLL), because the measurement of resonance frequencies using a PLL introduces significant deviations in mass determination. Therefore, the response spectra (amplitude, phase) for an input frequency sweep were recorded directly. From raw data, various parameters can be extracted such as damping (quality factor), spring constant and the absolute mass of the ligand bound to the cantilever. NOSEtools software developed can do semi-automated handling, processing

and presentation of such sensor data.

Measurements acquired at defined time-intervals (e.g. cantilever deflection versus time) and measurements acquired at different time-intervals (such as frequency spectra) need special organization of the data structure in the software for synchronization in time: Raw data are stored in so called projects and all calculations are performed in instances. All data in instances are time-scaled and can be compared directly. Dynamic mode data of recorded spectra for a specific time point has to be post-processed and the results are stored in another instance. A flow-diagram of this separation is shown in Fig. 2.9 in comparison to the graphical implementation of the software.

Recorded time series of spectra are analyzed using two methods: 1. Amplitude peak-tracking and phase-turning point tracking (Ghatkesar et al., 2004). This method involves fitting the amplitude response to a Gaussian to extract peak frequency, quality factor and damping factor; phase response to sigmoidal function to extract eigen frequency (phase turn point) Fig. 2.10A. 2. Least-mean square fitting of the spectrum. This method involved fitting of the amplitude and the corresponding phase spectrum by SHM model (Fig. 2.10B) described in chapter 3. Fig. 2.10C shows a screen shot of the software frontend.

The static deflection of the cantilever is obtained from the x_1 and x_2 signals of the PSD and the calibration factor.

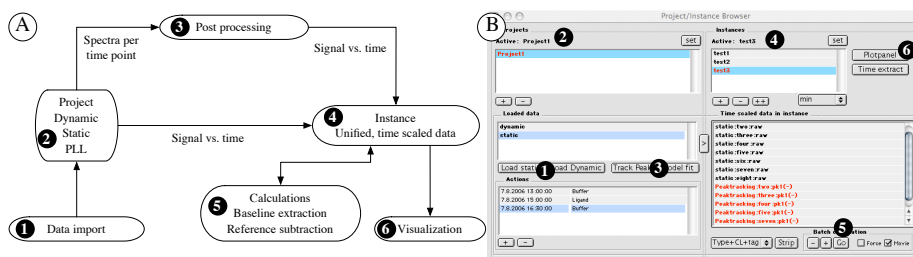


Fig. 2.9: Organization of data handling in the NOSEtool software. A) Diagram of the data flow in the software. B) User interface for the data control representing the diagram of A. (1) Data import for raw data, (2) Projects: Contains raw data and all associated informations, (3) Post processing tools for non-time-scaled data, (4) Instances: Containing time scaled data. Here all calculations (baseline correction, reference subtraction) take place (5), (6) Visualization of the time-scaled data in graphs.

2.3 Gold Coating

For biological experiments, receptor molecules have to be immobilized on the cantilever surface. Surface roughness of the gold is very important for molecules to immobilize on the substrate. Experiments were performed on gold surface deposited by e-beam, thermal deposition and sputtering. Images of these surfaces were obtained by tapping mode AFM using Veeco's nanoscope IIIa as shown in Fig. 2.11. The rms roughness was determined for all samples. For DNA experiments, smooth and less stressed gold layer obtained by e-beam is preferred over others. For large molecules like protein and vesicles, thermal or sputter deposited gold can also be used. Thermal evaporation: Balzers MED 010 thermal evaporator; Sputtering: Baltec SCD 050 for Cr (120 mA, 0.05 mbar), Baltec MED 020 for Au (50 mA, 0.02 mbar); E-beam: BOC Edwards,

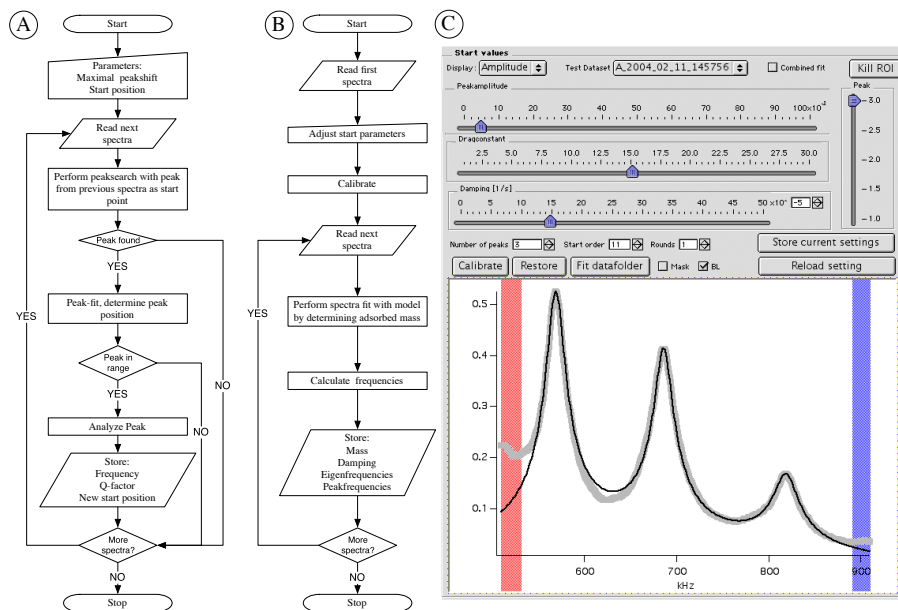


Fig. 2.10: Simplified flow diagram for peak tracking and model fit algorithms. (A) The peaktracking procedure reads in one spectrum after the other. The user provides start position and a maximal peak-shift for the peak-search which propagates from spectrum to spectrum. Note that a gauss fit or Lorentz fit is used to minimize the effect of noise instead of data smoothing. For the phase data an analogue algorithm was used. (B) work flow for mass determination by modeling a series of spectra. (C) Graphical user interface for data modeling. Note the preview-window with the raw data (thick grey line) and the fit to the model in black.

Sussex, U.K. A gold layer of 20 nm was deposited by all techniques. The adhesion layer of 2 nm used in evaporation techniques consists of titanium and in sputtering chromium was used.

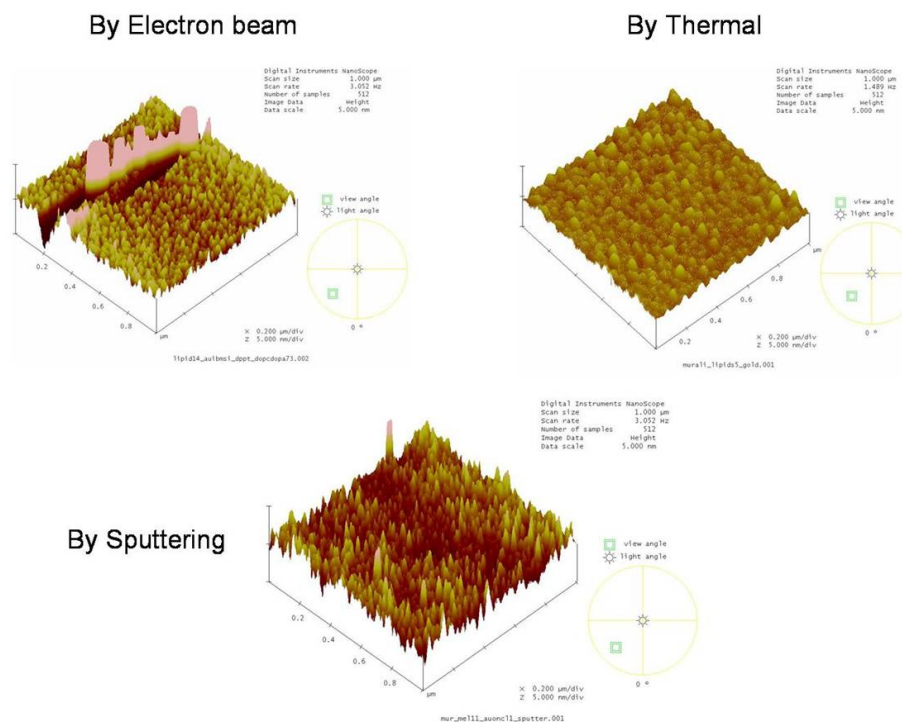


Fig. 2.11: Gold coating

2.4 Functionalization

The controlled deposition of functional layers on the gold surface is the key issue for converting nanomechanical cantilevers into chemical or biochemical sensors. For all the experiments either capillary technique or inkjet spotting technique was used to functionalize the cantilevers.

2.4.1 Capillary technique

The cantilevers of an array are immersed into the open ends of a microcapillary array filled with various coating solutions for functionalization, as shown in Fig. 2.12. The glass capillaries (Garner Glass Company, CA, USA) has an outer diameter of 0.25 mm, an inner diameter of 0.18 mm and a length of 75 mm. The design allows capillary refilling from reservoirs at the rear end of the glass capillaries compensated for evaporation losses at the front end. Owing to the complete cantilever immersion, a possible unspecific binding of molecules on the undesired side is the disadvantage of this technique (Bietsch, Zhang, et al., 2004; Bietsch, Hegner, et al., 2004).

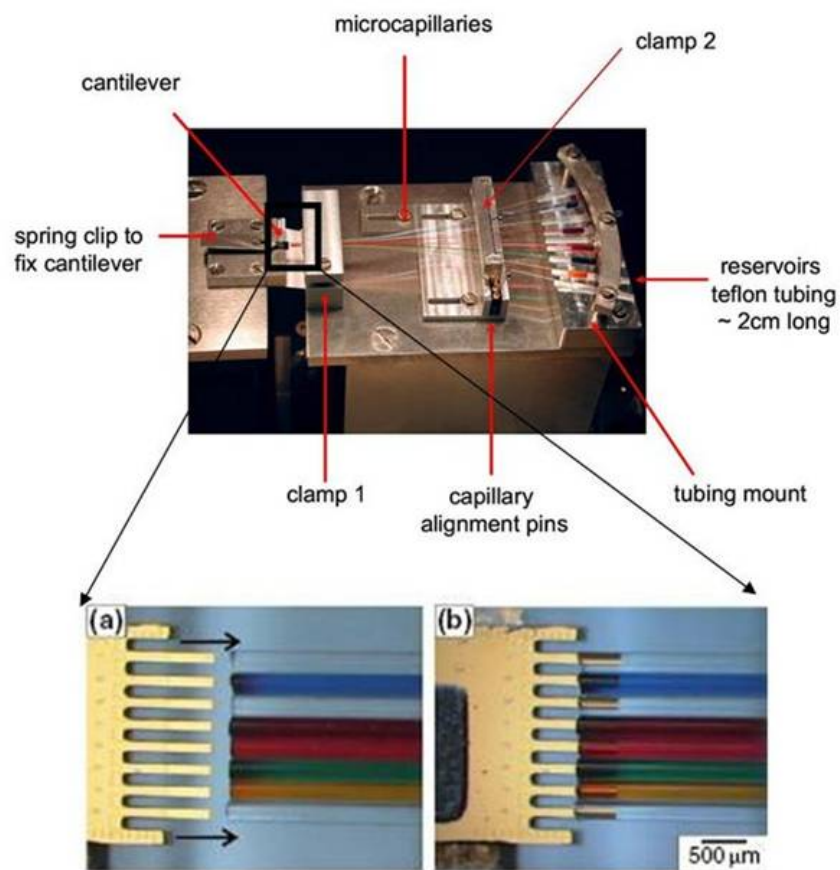


Fig. 2.12: Top: Functionalization setup using capillary technique. Bottom: Immersion of a cantilever array into an array of glass microcapillaries. (a) The cantilever array was aligned with respect to the capillary array. (b) The cantilevers are inserted into the capillaries; thus the entire array is functionalized in parallel

2.4.2 Inkjet spotting

A MD-P-705-L inkjet dispensing system (Microdrop, Norderstedt, Germany) was equipped with a three-axis micropositioning system having an accuracy of $10\ \mu\text{m}$ and piezo-driven autopipettes AD-K-501 with $70\ \mu\text{m}$ nozzle diameters. The piezo-pipettes were filled from the front side, allowing the use of small sample volumes of $5\text{--}25\ \mu\text{l}$. The pipettes can be cleaned using common agents, as their core is made of glass. In addition, the piezo-element enables cleaning by ultrasonic agitation. A stroboscopic camera system provides visual control to adjust piezo voltages and pulse durations for reliable droplet ejection and to avoid satellite drops. Single droplets with diameters in air of $60\text{--}80\ \mu\text{m}$ corresponding to volumes of $0.1\text{--}0.3\ \text{nl}$ were ejected on demand. Fig. 2.13 shows a schematic overview and illustrates how water droplets were deposited onto Si cantilevers. When droplets were spotted at a pitch smaller than $0.1\ \text{mm}$, they merged and formed continuous films. The vertical separation between the nozzle and the sample was typically $0.4\ \text{mm}$ (Bietsch, Zhang, et al., 2004; Bietsch, Hegner, et al., 2004).

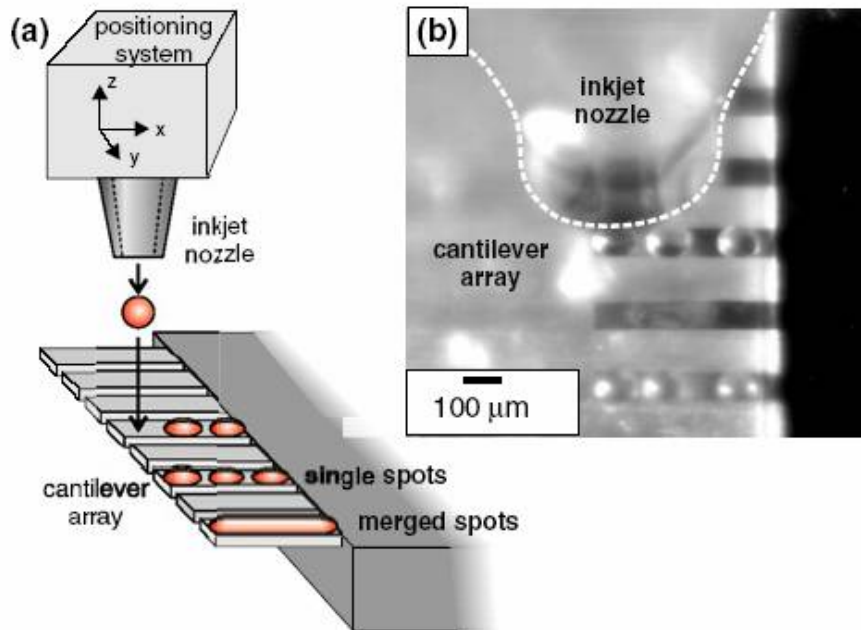


Fig. 2.13: Inkjet printing of individual droplets onto a cantilever array (a) as a scheme and (b) as seen by a video camera. A positioning system allows accurate placement of single droplets onto selected cantilevers. When deposited at a small pitch, the droplets merge into a continuous layer covering the entire cantilever length. For demonstration, three droplets of water are deposited onto selected cantilevers. Owing to the oblique view of the camera, only the central cantilever is in focus.

2.5 Modes of operation

2.5.1 Static Mode

In static mode, cantilever deflection resulting due to surface stress is measured (Stoney, 1909; Lang et al., 2005). The upper and lower surface areas of the cantilever experience different stress due to which the cantilever bends. The amount of surface stress can be obtained from stoney's formula (Eq. 2.2).

$$\sigma = \frac{Eh^2}{6R(1-\nu)} \quad (2.2)$$

where E and ν are elastic modulus and Poisson's ratio of cantilever material respectively, h is thickness, R is bending radius of the cantilever. The amount of bending depends on the spring constant k (Eq. 2.3, softer (lower the spring constant) the cantilever, larger the amount of bending).

$$k = \frac{3EI}{L^3} \quad (2.3)$$

where $I = bh^3/12$ is moment of inertia for a cantilever of width b .

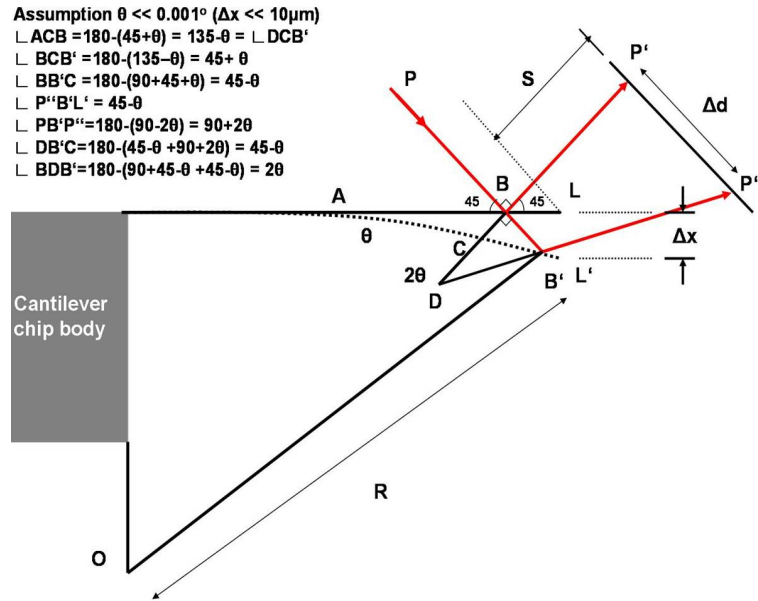


Fig. 2.14: Calibration of static deflection with optical beam deflection technique

With a bending moment M at its free end for a cantilever of length L , the angle of bending θ and deflection Δx_{max} as shown in Fig. 2.14 is given by (Timoshenko & Young, 2003)

$$\theta = \frac{ML}{EI} \quad (2.4)$$

$$\Delta x = \frac{ML^2}{2EI} \quad (2.5)$$

hence θ in terms of Δx_{max} is given by

$$\theta = \frac{2\Delta x}{L} \quad (2.6)$$

Assuming the angle of deflection to be $\theta \ll 0.001^\circ$ or $\Delta x \ll 10\mu\text{m}$ for a cantilever of $500\mu\text{m}$ in length, $100\mu\text{m}$ in width and $1\mu\text{m}$ in thickness, part of the arc can be considered as straight line for geometric simplification. With this assumption, a bending angle of θ for a cantilever from its initial position will result in an angle of 2θ between the reflected positions of the laser beam before and after bending (see the inset in Fig. 2.14). As $S \gg \Delta x$, the angle of the sector $p'Dp''$ can be written as

$$2\theta = \frac{\Delta d}{S} \quad (2.7)$$

Substituting θ in equation 2.7 from equation 2.6 and rearranging the terms results in

$$\Delta x = \frac{\Delta d L}{4S} \quad (2.8)$$

From the working principle of PSD

$$\Delta d = \left(\frac{I_1 - I_2}{I_1 + I_2} \right) \frac{L_{psd}}{2} \quad (2.9)$$

where L_{psd} is length of the PSD.

Radius of curvature of the bent cantilever is obtained as

$$R = \frac{L}{\theta} = \frac{2SL}{\Delta d} = \frac{L^2}{2\Delta x} \quad (2.10)$$

Hence surface stress from Eq. 2.2 can be calculated.

2.5.2 Dynamic Mode

For a homogeneous beam of uniform cross section, the equation of motion for flexural vibrations is a differential equation of fourth order

$$EI \frac{\partial^4 u(x,t)}{\partial x^4} + C_0 \frac{\partial u(x,t)}{\partial t} + \frac{m_c}{L} \frac{\partial^2 u(x,t)}{\partial t^2} = 0, \quad (2.11)$$

The first term represents the restoring force per unit length, whereas EI the flexural rigidity, E the elastic modulus, I the moment of inertia, C_0 the intrinsic damping coefficient per unit length that describes internal losses, m_c the mass of the cantilever, L the length of the cantilever and $u(x,t)$ the deflection of the cantilever perpendicular to the cantilever axis with x as the coordinate along the cantilever axis and t is time.

With appropriate boundary conditions, the resonant frequencies for mode n in vacuum are given by

$$f_{R,n} = \frac{\alpha_n^2}{2\pi} \sqrt{\frac{k}{3m_c}}. \quad (2.12)$$

where $k = 3EI/L^3$ and the α_n are related to the different eigenvalues of the harmonics and are the n^{th} positive root of the equation $1 + \cos \alpha_n \cosh \alpha_n = 0$ and are

fixed by the boundary conditions (Young & Felgar, 1949). ($\alpha_1 = 1.875$, $\alpha_2 = 4.694$, $\alpha_3 = 7.854$, $\alpha_4 = 11.0$, $\alpha_{5\dots n} = \pi(n-0.5)$.)

For a cantilever vibrating in a viscous fluid with the following assumptions (1) the cross section of the beam is uniform along its entire length and is rectangular in geometry; (2) the length of the beam L greatly exceeds its width b , which in turn greatly exceeds its thickness h ; (3) the amplitude of vibration is far smaller than any geometric length scale of the beam; (4) internal structural dissipative effects are negligible in comparison with those of the fluid; (5) the fluid is incompressible in nature and is unbounded in space, the equation of motion of the cantilever beam is

$$EI \frac{\partial^4 u(x,t)}{\partial x^4} + (C_0 + C_v) \frac{\partial u(x,t)}{\partial t} + \frac{m_c + m_l}{L} \frac{\partial^2 u(x,t)}{\partial t^2} = F_{ext}, \quad (2.13)$$

where C_v is additional dissipation in fluid, m_l is additional added apparent mass which cantilever has to displace in liquid, F_{ext} is the external driving force. Various theoretical models considering the 2D and 3D fluid flow across the cantilever estimate the resonance frequency values and the corresponding quality factors of various modes (Sader, 1998; Eysden & Sader, 2006, 2007; Elmer & Dreier, 1997; Paul et al., 2006; Kirstein et al., 1998; Rabe et al., 1996). Some of them are discussed in detail in chapter 4.

Owing to their small amplitude, vibrating cantilever is modeled as a damped simple harmonic oscillator (SHO) at all modes. The amplitude response of the n^{th} harmonics in dependence of the frequency of the driving force is given according to the model of a damped harmonic oscillator by

$$u_n(f) = \frac{u_{\max} f_{R,n}^2}{\sqrt{(f_{R,n}^2 - f^2)^2 + \frac{\gamma^2 f^2}{\pi^2}}}. \quad (2.14)$$

This function is also called resonance curve and has a maximum peak frequency ($f_{Rmax,n}$) at

$$f_{Rmax,n} = \sqrt{f_{R,n}^2 - \frac{\gamma^2}{2\pi}}. \quad (2.15)$$

The phase between response and driving force in dependence of the frequency of the driving force is given by

$$\varphi(f) = \arctan \frac{-\gamma f}{\pi(f_{R,n}^2 - f^2)}. \quad (2.16)$$

The eigenfrequency $f_{R,n}$ is defined at that point where the phase curve has its steepest slope. It will be called the turning point of the curve. Note that peak frequency is not same as eigen frequency.

The cantilever vibrating in liquid has to displace an additional mass of the liquid m_l apart from mass of the cantilever m_c , the eigen frequency due to this effective mass is

$$f_{R,n} = \frac{\alpha_n^2}{2\pi} \sqrt{\frac{k}{3(m_c + m_l)}}. \quad (2.17)$$

The damping factor γ of the system is

$$\gamma = \frac{C_0 + C_v}{\frac{2}{L}(m_c + m_l)} = \frac{2\pi f_{Rmax,n}}{Q} = \Delta f. \quad (2.18)$$

where Q is quality factor and Δf the frequency difference at $1/\sqrt{2}$ of the maximum amplitude.

Assuming that the spring constant does not change, due to uniform mass addition of Δm on the cantilever, the eigenfrequency $f_{R,n}$ of Eq. 2.17 is modified as

$$f'_{R,n} = \frac{\alpha_n^2}{2\pi} \sqrt{\frac{k}{3(m_c + m_l + \Delta m)}}. \quad (2.19)$$

For $\Delta m \ll m_c + m_l$ the following approximation is valid:

$$f'_{R,n} \approx f_{R,n} \left(1 - \frac{1}{2} \frac{\Delta m}{m_c + m_l} \right). \quad (2.20)$$

The mass load Δm in terms of the frequency shift Δf is calculated as

$$\Delta m = \frac{2(m_c + m_l)\Delta f}{f_{R,n}}, \quad (2.21)$$

where $\Delta f = f_{R,n} - f'_{R,n}$.

2.5.3 Combined mode

For a resonating cantilever, due to mass/spring constant change, frequency shifts. In addition, if there is a surface stress on the cantilever surface, it also bends. Monitoring the shift in the resonance frequency of the laser beam yields the change in the effective value of mass/spring constant of the cantilever and the shift in its average position gives amount of bending of the cantilever. By separating AC and DC signals of the PSD, both the dynamic and static signals of the corresponding cantilever can be obtained simultaneously (Fig. 2.2).

2.6 Results and Discussion

2.6.1 Characterization of PSD

An array of 8 VCSELs were used to detect the nanomechanical motion of the vibrating cantilever. Two convex lens system was used to focus 8 laser beams on 8 cantilevers. After reflecting from the apex of the cantilever, each focussed laser beam again diverges. Hence a proper choice of position sensitive detector (PSD) at appropriate distance is very important for correct interpretation of the signal. The implication of PSD size and size of the laser beam is shown in Fig. 2.16, Fig. 2.17 and Fig. 2.18.

The Fig. 2.16 shows response characteristics of a $5 \times 5 \text{ mm}^2$ PSD for a laser beam of 0.5 mm in diameter. As the laser beam is moved across the PSD from electrode $X1$ to $X2$, the magnitude of current at electrode $X1$ decreases and at $X2$ it increases. The corresponding sum and difference signal indicate that an effective area of 4 mm on the PSD has a linear response for the position of the laser beam. In this region, position of the laser beam can be clearly identified. The response characteristics on the same PSD for a laser beam of 7.5 mm diameter. As the laser beam diameter is larger than the size of the PSD itself, the active area is only 2 mm. Similar characteristics for $10 \times 10 \text{ mm}^2$ PSD is shown in Fig. 2.17. During the initial stages of the system setup a four quadrant detector was also characterized. However, owing to its working principle, it is useful only for the dynamic mode operation and cannot be used to get static mode (Fig. 2.18).

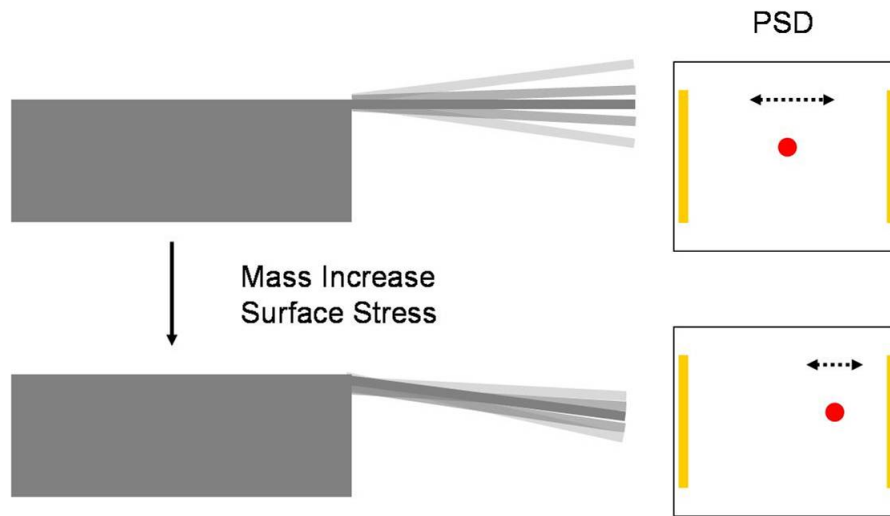


Fig. 2.15: Principle of combined mode detection. Initially the cantilever resonates at a certain frequency, the mean position of the laser is at the center of PSD. After certain distributed mass load and surface stress formation on the top side of the cantilever, the resonant frequency shifts to lower value and the average position shifts to new place

For an array of 8 cantilevers, after gold coating and different functionalization they may not be exactly parallel to each other. Moreover to make a combined mode measurement a choice of wide linear range on the PSD is preferred. Hence, we have chosen 10x10 mm PSD for all our experiments.

2.6.2 Simultaneous measurement of dynamic and static mode

The setup allows simultaneous detection of microcantilever oscillation and bending of eight cantilevers by time multiplexed optical read out. By filtering out the ac (oscillation) component, dc (bending) component is extracted, yielding information about mass and surface stress changes simultaneously.

The results of the heat test are displayed in Fig. 2.19. Panel A shows the static bending of all cantilever arrays, panel B the virtual mass of the co-moving liquid from the amplitude spectra. In the static mode, a clear bending of the cantilever is observed during the heating period. The mechanical energy for this work originates from the different thermal expansion-coefficients of gold ($14.2 \times 10^{-6} \text{ K}^{-1}$) and silicon ($2.6 \times 10^{-6} \text{ K}^{-1}$) leading to a bimetal effect. The cantilever bends towards the silicon interface as the thermal expansion coefficient of gold is larger than silicon. The uniformity of the cantilever response demonstrates the high mechanical quality of the cantilevers. In the dynamic signal, the virtual mass of the co-moving liquid is lowered by the heat pulse. This observation is in agreement with the expectations that the density of the buffer is lower and intermolecular interactions are weaker between liquid molecules at higher temperature. However, the response shows a large variation in the mass among different cantilevers. The measured mass changes increased depending on the position of the cantilever in the array: The further away from the buffer inlet the larger the mass change

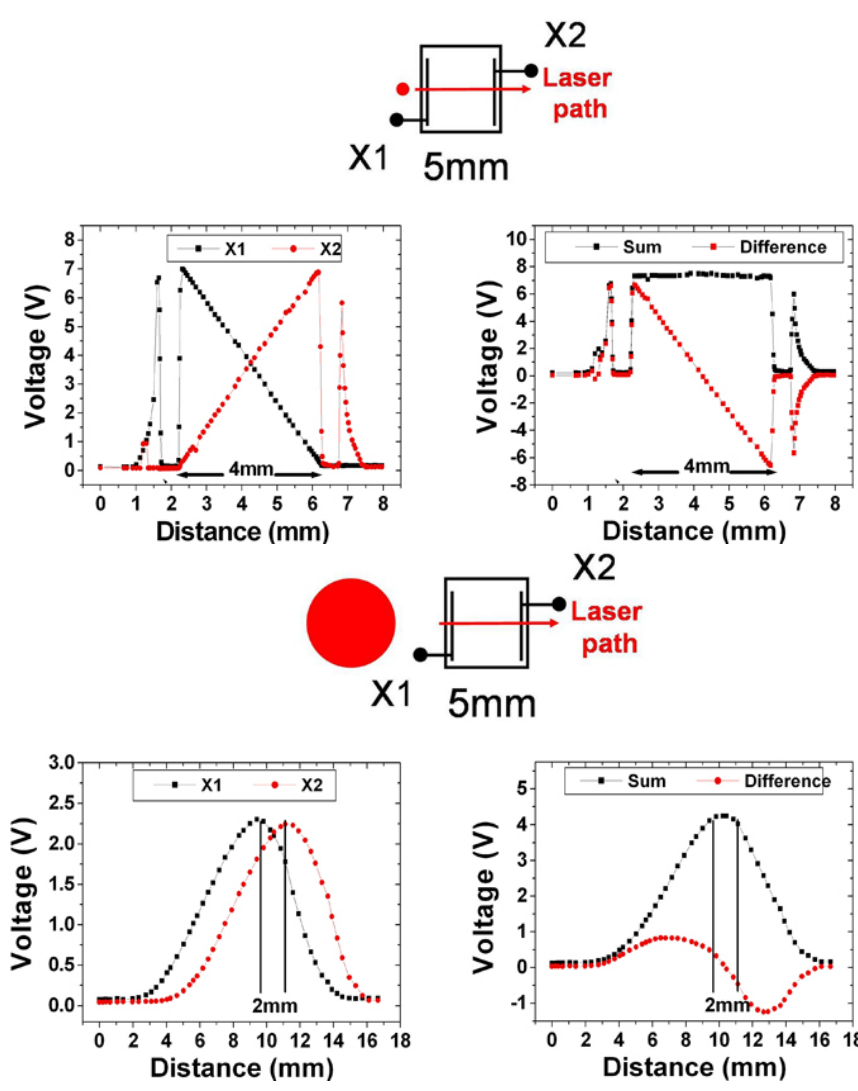


Fig. 2.16: Response characteristics of $5 \times 5 \text{ mm}^2$ PSD for a laser beam diameter of 0.5 mm (Top panel) and 7.5 mm (bottom panel). For a smaller laser beam diameter, an effective area of 4 mm and for bigger laser beam diameter only 2 mm of the total PSD provides linear response.

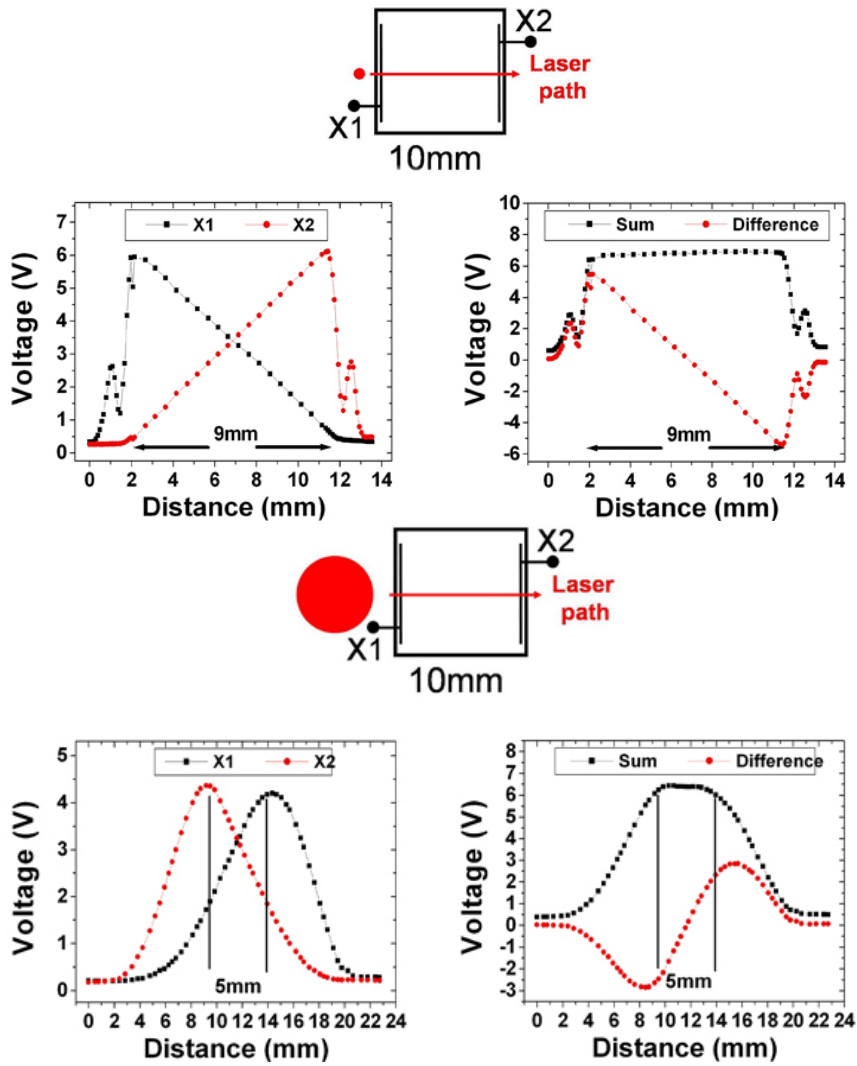


Fig. 2.17: Response characteristics of $10 \times 10 \text{ mm}^2$ PSD for a laser beam diameter of 0.5 mm (top panel) and 7.5 mm (bottom panel). For the smaller laser beam diameter, an effective area of 9 mm and for bigger laser beam diameter only 5 mm of the total PSD has linear response.

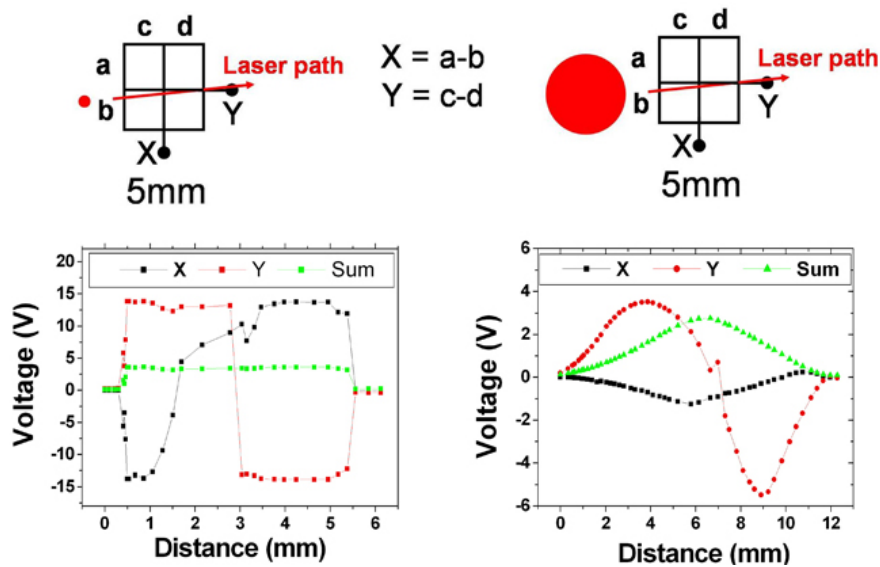


Fig. 2.18: Response characteristics of $5 \times 5 \text{ mm}^2$ four quadrant detector for a laser beam of 0.5 mm (left panel) and 7.5 mm (right panel). These kind of detectors are useful only for dynamic mode, they cannot detect static mode signals.

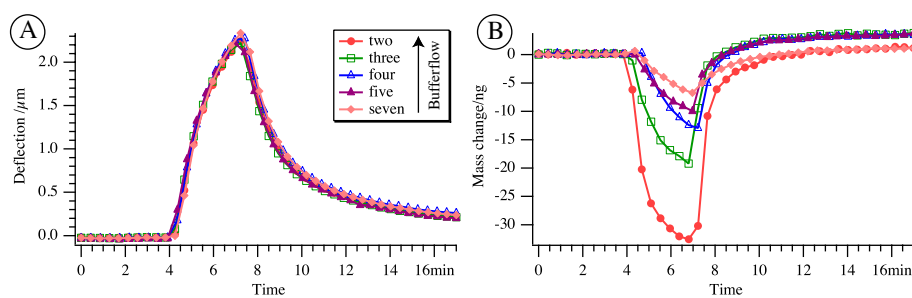


Fig. 2.19: Heat test of a cantilever array immersed in buffer. The heating period is indicated in gray. A) static deflection signal, B) Dynamic signal after post-processing by modeling the amplitude spectra. The flow of buffer is indicated in the inset.

(see inset in Fig. 2.19). The explanation is found in the temperature control of the system: The heat pulse is performed by a peltier near the cantilever array (Fig. 2.4). This ensures a good thermal coupling with the cantilever array which is heated homogeneously for all cantilevers. In contrast to that, the buffer has to be heated up first by the chamber and due to the constant buffer-flow (12 μ l/min) a temperature gradient builds in the liquid of the measurement cell (volume: 5 μ l. Therefore different cantilevers experiences different local liquid characteristics. Taken together we measured the static and dynamic signal in parallel. The response of the two modes is in good agreement reflecting the characteristics they are sensing in response to the heat test: The static mode reflects the internal reaction of the cantilever on heat, whereas the dynamic mode senses changes in the environment.

2.7 Conclusion

A quantitative nanomechanical cantilever sensor setup capable of simultaneously measuring adsorbed mass (dynamic mode) and surface stress (static mode) in liquid has been built. It is suitable to quantify certain real-time multi-step biological processes like virus binding and DNA injecting, ligand binding and protein conformation change, ligand binding as well as pore formation.

CHAPTER 3

HIGHER MODES OF VIBRATION INCREASE MASS SENSITIVITY

*"I am among those who think that science has great beauty.
A scientist in his laboratory is not only a technician;
he is also a child placed before natural phenomena
which impress him like a fairy tale." – Marie Curie*

We evaluated the potential and limitation of resonating nanomechanical microcantilevers to detect mass adsorption. As a test-system we used mass addition of gold layers with varying thickness. Our main findings are: 1. The parabolic increase in mass sensitivity with mode number, a sensitivity of $8.6 \text{ ag/Hz}/\mu\text{m}^2$ achieved at its 7th mode is two orders of magnitude higher than at the fundamental mode. 2. The quality factor increases with the mode number thus aiding to achieve higher sensitivity. 3. The effective spring constant value of the cantilever due to gold layer deposition remains constant atleast upto 2 % of the cantilever thickness.

3.1 Introduction

Microfabricated mechanical structures like cantilevers and beams operated at their resonance frequency are used as extremely sensitive mass detectors. Mass adsorption on these resonators shifts their resonance frequency. The aim is to reach maximum sensitivity (maximum frequency shift for a given mass change) and resolution (minimum detectable mass). In this pursuit, zeptogram (10^{-21} g) sensitivity obtained in vacuum has been recently reported (Yang et al., 2006). A general approach to gain higher sensitivity is to reduce the inertial mass of the resonating sensor itself. Mass sensitivity increase from pg to fg was achieved by reducing the volume of the device by ~ 1000 times (Ekinci & Roukes, 2005). Different sensor geometries and various materials are also used to measure small masses (Ilic, Craighead, et al., 2004; Craighead, 2000; Calleja et al., 2005).

Assuming that the spring constant of a microcantilever remains unchanged, the mass sensitivity is given as (T. Braun, Barwich, et al., 2005; Ghatkesar et al., 2004)

$$S = \frac{\Delta f}{\Delta m} = \frac{f_{R,n}}{2m_c}, \quad (3.1)$$

where, Δf is the frequency shift for a mass addition of Δm , $f_{R,n}$ is the resonance frequency at a mode number n for a cantilever of mass m_c . The frequency shift obtained for a unit mass adsorbed on a given cantilever is directly proportional to the resonance frequency at mode number n . Hence, for the same cantilever dimensions, the sensitivity can be increased by operating the cantilever at higher modes of vibration.

For biological and chemical applications of these sensors, distributed mass load spanning the entire cantilever surface is preferred instead of mass load at selected area (Chen et al., 1995; Wachter & Thundat, 1995; Pinnaduwege et al., 2003; Nugaeva et al., 2005; Battiston et al., 2001; Gfeller et al., 2005a). It allows to refrain from the tedious process of selective activation of the surface and avoids unspecific binding.

To mimic such situations, we used cantilevers deposited with gold layers of different thicknesses on the entire upper surface of the cantilever. Moreover, the cantilever thickness was also varied between 1 and 7 μm . The frequency response of the cantilevers was measured and evaluated at various flexural modes of vibration before and after gold layer deposition.

3.2 Experiment Details

Three different types of cantilever arrays with eight identical Si cantilevers each 500 μm long, 100 μm wide, but different thicknesses of 7 μm , 4 μm and 1 μm respectively were used. The cantilever arrays of 7 μm and 4 μm thick were wet etched out of Si wafer while 1 μm thick cantilevers were dry etched out of Silicon on Insulator (SOI) wafer. They were microfabricated by the Micro and Nanomechanics group, IBM Zurich research laboratory in Rüschlikon, Switzerland. A scanning electron microscope (SEM) image of an individual array chip is shown in Fig. 3.1A.

3.2.1 Preparation of the cantilevers

Layers of different thickness of gold were deposited on the top side of the cantilevers with an initial Titanium (99.99%, Johnson Matthey, London, UK) adhesion layer of 2 nm between Si and gold (99.999%, Goodfellow, Bad Nauheim, Germany). All depositions were done in a Balzers MED 010 thermal evaporator operated at a base pressure below 10^{-5} mbar and evaporation rates of 0.16 nm/s. Three layers of 40nm thick gold were deposited successively. A shadow mask was used to physically cover cantilevers numbered (see Fig. 3.1B) one to six for the first deposition, one to four for the second deposition and finally one and two for the third deposition. After three successive depositions, cantilevers numbered 1 and 2 were obtained with no gold, 3 and 4 with 40 nm, 5 and 6 with 80 nm and 7 and 8 with 120 nm thick gold layers respectively. The density values used for silicon, titanium and gold were $\rho_{Si}=2330 \text{ kg/m}^3$, $\rho_{Ti}=4990 \text{ kg/m}^3$, $\rho_{Au}=19320 \text{ kg/m}^3$ respectively. The corresponding elastic moduli values used were $E_{Si} = 169 \text{ GPa}$, $E_{Ti} = 110 \text{ GPa}$, $E_{Au} = 69 \text{ GPa}$ respectively.

3.2.2 Setup

Ambient thermal excitation of the cantilevers was not sufficient to detect the various vibrating modes. This is due to the fact that some of the cantilevers chosen were of high spring constant value. Furthermore, the spring constant value increases with the mode number (Rast et al., 2000). For these reasons, the cantilevers were driven externally by a piezo. The drive amplitude was kept low without invoking nonlinearities in the cantilever vibrations and satisfying simple harmonic oscillator (SHO) condition. The

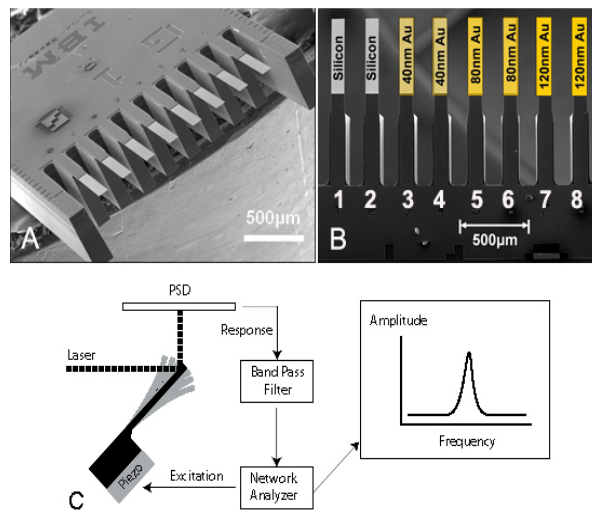


Fig. 3.1: (A) An array of 8 cantilevers having same dimensions of length, width and thickness. (B) Different thicknesses of gold coating on the cantilever array. Sets of two cantilevers each were chosen for the deposition of 40 nm, 80 nm and 120 nm thickness of gold. This was achieved using a shadow mask, exposing two cantilevers for every 40 nm of successive gold depositions. Two cantilevers were left bare silicon as reference. (C) Experimental setup for the measurement. A linear frequency sweep with sinusoidal signal from network analyzer excites the piezo beneath the cantilever. Cantilever vibrations were detected by laser beam deflection technique. The output signal detected was limited from 500 Hz to 1 MHz by a band pass filter. Input and output signals were compared in the network analyzer to give resonance spectrum.

aspect ratio of all the cantilevers was $L/b = 5$ and the amplitude of vibration is low compared to any dimension of the cantilever. The experimental setup used for the measurement is shown in the Fig. 3.1C. The cantilever array was mounted on a piezo element PZT-5A purchased from Staveley Sensors, East Hartford, CT, USA. By placing the piezo beneath the cantilever chip body in direct contact, the excitation energy was efficiently transferred to the cantilevers. For a linear frequency sweep with a sinusoidal signal from the network analyzer (Hewlett Packard, 4589A, USA), cantilevers were excited at various vibrating modes. A laser beam deflection technique was used to detect frequencies of the cantilever vibrations (Meyer & Amer, 1988). Time multiplexed laser light emitted sequentially from 8 vertical cavity surface emitting lasers (VCSEL; wavelength 760 nm, Avalon Photonics, Zurich, Switzerland) deflected from the apex of the cantilever to a 1D position sensitive detector (PSD; Sitek, Partille, Sweden) (Lang, Berger, Andreoli, et al., 1998) were used. The pitch of the VCSELs matches that of the cantilevers. The output signal current of the PSD was converted into voltage and band pass filtered (BPF) in a bandwidth range of 500 Hz to 1 MHz. The network analyzer converted the time domain signals into a frequency spectrum with peaks corresponding to the different resonating flexural modes of the cantilever.

The resonance frequencies of all cantilevers at various modes are recorded before and after gold coating. All measurements were performed in ambient air. Initially a complete spectrum with resonance peaks corresponding to all the modes was recorded. Then each mode was individually recorded to determine the corresponding resonance frequency peak value with higher resolution.

3.3 Theory

3.3.1 Resonance frequency

The resonance frequency of a vibrating cantilever at an arbitrary mode number n in vacuum is given as

$$f_{R,n}^{theo} = \frac{\alpha_n^2}{2\pi} \sqrt{\frac{EI}{m_c l^3}}. \quad (3.2)$$

where E is the elastic modulus of the material, I is the moment of inertia of the cantilever, l its length, b its width, h its thickness, m_c its mass and constants $\alpha_1 = 1.875$, $\alpha_2 = 4.694$, $\alpha_3 = 7.854$, $\alpha_4 = 11.0$, $\alpha_{5...n} = \pi(n-0.5)$ (Young & Felgar, 1949). The value $n=1$ refers to the fundamental mode or mode 1. In practice, cantilevers are never ideal, they can have internal defects or imperfections from the etching process. These features can contribute to deviation of resonance frequencies from the theoretical predicted values. To account for such deviations, we introduce a correction factor C to Eq. (4.1) as follows.

$$f_{R,n} = C \frac{\alpha_n^2}{2\pi} \sqrt{\frac{EI}{m_c l^3}}, \quad (3.3)$$

where,

$$C = \frac{f_{R,n}}{f_{R,1}} \frac{\alpha_1^2}{\alpha_n^2}. \quad (3.4)$$

with $f_{R,n}$ and $f_{R,1}$ being the resonance frequencies measured experimentally at mode n and mode 1. $C = 1$ for an ideal cantilever for all modes.

Resonance frequency and quality factor for each mode is obtained by fitting the corresponding frequency spectrum to a SHO function as shown in Eq. (3.5) with fitting

parameters being A_0 , $f_{R,n}$ and Q (Chon et al., 2000).

$$A(f) \cong \frac{A_0 f_{R,n}^2}{\sqrt{(f^2 - f_{R,n}^2) + \frac{f^2 f_{R,n}^2}{Q^2}}}, \quad (3.5)$$

where A_0 is the zero frequency amplitude of the response and Q is the quality factor of the mode. Note that SHO condition is satisfied only for $Q \geq 1$, $L/b \geq 4$ and without invoking nonlinearities in vibration (Chon et al., 2000).

3.3.2 Calculation of mass

During Au layer deposition on the microcantilevers, a quartz crystal microbalance placed adjacent to arrays determine the thickness of the layer deposited. Considering the Ti adhesion layer deposited between Si cantilever and Au layer, the mass calculated on a single cantilever is

$$\Delta m_q = \rho_{Ti} l b h_{Ti} + \rho_{Au} l b h_{Au} \quad (3.6)$$

where, h_{Ti} and h_{Au} are the thickness of Ti and Au respectively. This mass will be compared with mass obtained by resonance frequency change of the cantilever.

The mass calculation from resonance frequency shift of the cantilever vibrations is carried out in two ways termed as "mass only effect" and "mass & spring constant effect". In "mass only effect", the frequency shift obtained is considered to be only due to mass change on the cantilever, while in "mass & spring constant effect", the spring constant values of Ti and Au layers are also considered along with their respective mass. Cantilevers were considered as composite structures and from Eq. 3.3 we derive

$$\Delta m_m = C^2 \frac{\alpha_n^4}{4\pi^2 l^3} EI \left(\frac{1}{f_{R,n}^2} - \frac{1}{f'_{R,n}{}^2} \right), \quad (3.7)$$

where, Δm_m is the mass according to the "mass only effect" and $f'_{R,n}$ is the frequency after the Au layer deposition.

$$\Delta m_{mk} = C^2 \frac{\alpha_n^4}{4\pi^2 l^3} \left(\frac{\sum_{i=0}^3 E_i I_i}{f_{R,n}^2} - \frac{EI}{f'_{R,n}{}^2} \right). \quad (3.8)$$

where, Δm_{mk} is the mass due to the "mass & spring constant" effect and the sum of 3 corresponds to three different materials: Si, Ti and Au (Herman et al., 2001).

3.4 Results

3.4.1 Visualization of resonance modes

Various modes of vibration were visualized using Scanning Electron Microscope (SEM). Fig. 3.2 shows images of the first three modes obtained for a $1\mu m$ thick cantilever. Nodes and antinodes were clearly visible for mode 1 and mode 2, but they are barely visible for mode 3. Visualizing them after mode 3 was impossible using SEM as the vertical amplitude of the vibrating cantilever was beyond its resolution. The observation

| Mode | 7 μm | | 4 μm | | 1 μm | |
|------|-----------------|-----|-----------------|-----|-----------------|-----|
| | $f_{R,n}$ | Q | $f_{R,n}$ | Q | $f_{R,n}$ | Q |
| 1 | 36 | 363 | 22 | 168 | 6 | 19 |
| 2 | 206 | 730 | 138 | 455 | 40 | 73 |
| 3 | 496 | 948 | 379 | 688 | 112 | 139 |
| 4 | 868 | 821 | 710 | 603 | 220 | 220 |
| 5 | - | - | - | - | 364 | 291 |
| 6 | - | - | - | - | 552 | 300 |
| 7 | - | - | - | - | 765 | 280 |

Tab. 3.1: Resonance frequency ($f_{R,n}$ in kHz) and corresponding quality factor (Q) values of various modes (n) of 7 μm , 4 μm and 1 μm thick bare silicon cantilevers measured upto 1 MHz in ambient air. The standard deviation among 8 cantilevers in an array is $\leq 0.1\%$. In the frequency range upto 1 MHz, the cantilevers of 1 μm thick has 7 modes compared to only 4 modes for 4 μm and 7 μm thick cantilevers. The quality factor increased with mode number, the frequency spacing between adjacent modes also increased.

also indicates that not all the cantilevers have same resonance frequency. The difference was more prominent at higher modes. The observed high amplitudes of the vibrating cantilevers were due to high excitation voltage used just for visualizing the modes. Actual experiments for mass measurements were done at low amplitudes ($< 5\text{nm}$) of vibration, within limits of simple harmonic oscillator condition for a vibrating cantilever. For 4 μm and 7 μm cantilevers only first mode was observed (pictures not shown).

3.4.2 Frequency Spectra

The frequency spectra up to 1 MHz obtained for all the cantilevers are shown in the Fig. 6.3. Only four modes were observed for 7 μm and 4 μm thick cantilevers, while 1 μm thick cantilever exhibited 7 modes. As the thickness of the cantilever decreased, higher modes shifted to lower frequency values. Hence, more number of modes were visible in the same frequency range. The frequencies and the corresponding quality factors of all the cantilevers are given in Table 3.1. The values shown correspond to a single cantilever and the standard deviation of frequency among 8 cantilevers in an array was $\leq 0.1\%$. The quality factor increased with mode number. The frequency spacing between adjacent modes also increased with mode number. The spring constants calculated from the respective fundamental frequencies are $k_{7\mu\text{m}} = 9.6 \text{ N/m}$, $k_{4\mu\text{m}} = 2.3 \text{ N/m}$ and $k_{1\mu\text{m}} = 0.05 \text{ N/m}$ respectively.

3.4.3 Calibration

For a cantilever vibrating in a medium the resonance frequencies shift to lower values compared to their corresponding values in vacuum. This shift is caused mainly due to additional added apparent mass (also called as virtual mass) which vibrating cantilever has to displace in the medium. This extra mass depends on the viscosity and density properties of the medium surrounding the cantilever. In air, the deviation is found to be about 0.5 % at all modes (Chon et al., 2000; Elmer & Dreier, 1997; Maali et al., 2005). However, we neglect the effect of virtual mass of air in our present calculations.

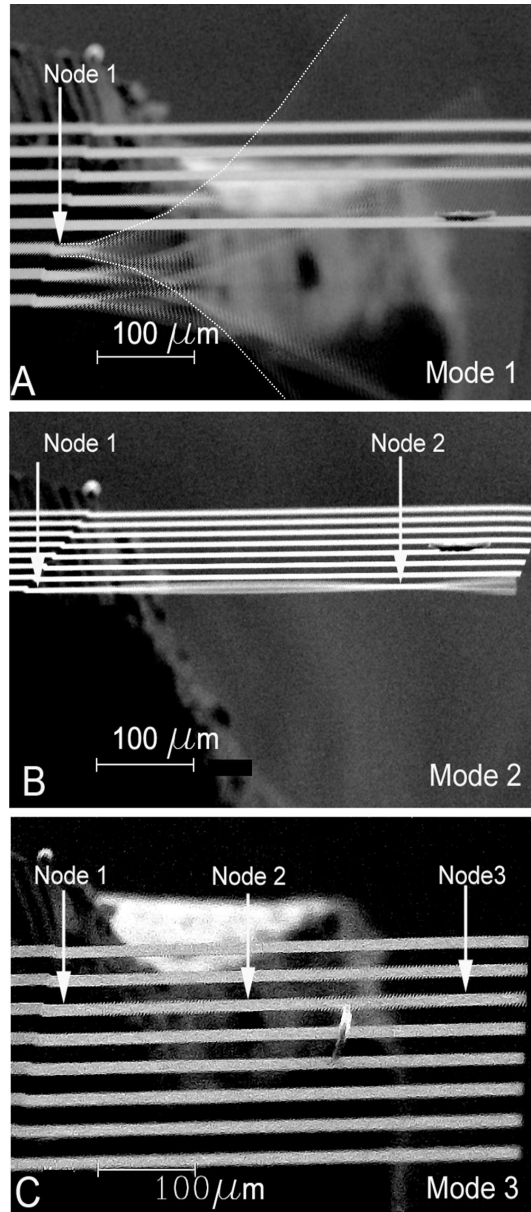


Fig. 3.2: SEM images of cantilever vibrations for the first three modes. The number of nodes defines the mode number. (A) Mode 1, (B) Mode 2, (C) Mode 3. The antinodes in Mode 3, which are very low in vertical vibration amplitude of the cantilever, are observed to be "hazy" compared to well focussed lower nodes on the indicated cantilever.

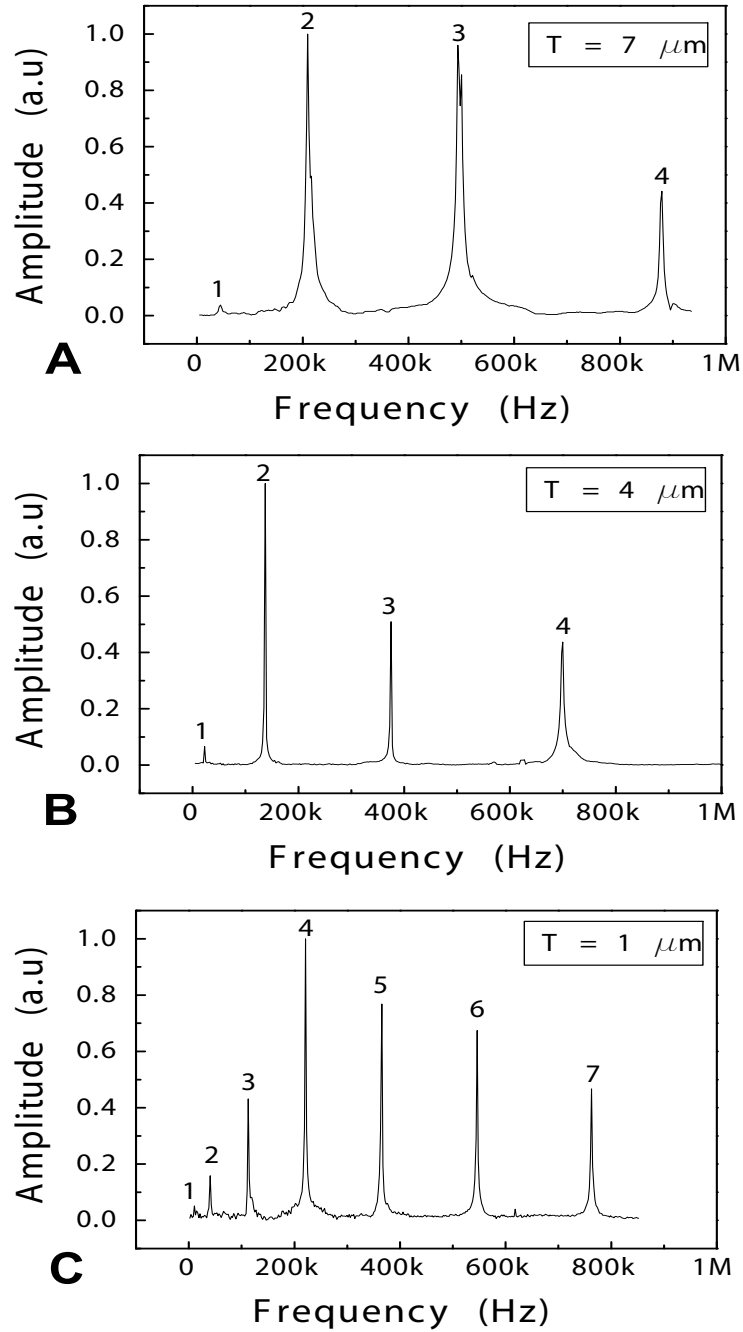


Fig. 3.3: Complete spectra of resonance frequencies up to 1 MHz. All cantilevers are $500\mu\text{m}$ long and $100\mu\text{m}$ wide. (A) $7\mu\text{m}$ thick. (B) $4\mu\text{m}$ thick and (C) $1\mu\text{m}$ thick. More number of modes were visible for thinner cantilevers. The spacing between adjacent modes increased with mode number.

| Mode | 7 μm | 4 μm | 1 μm |
|------|------------------|------------------|------------------|
| n | $f_{R,n}^{theo}$ | $f_{R,n}^{theo}$ | $f_{R,n}^{theo}$ |
| 1 | 36 | 22 | 6 |
| 2 | 224 | 139 | 39 |
| 3 | 627 | 389 | 109 |
| 4 | 1229 | 761 | 214 |
| 5 | 2031 | 1258 | 354 |
| 6 | 3034 | 1880 | 529 |
| 7 | 4238 | 2626 | 739 |

Tab. 3.2: Resonance frequencies ($f_{R,n}^{theo}$ in kHz) estimated at various modes for cantilevers of different thickness. Thickness calculated from the fundamental mode was used to estimate the higher frequency modes. From the fundamental frequency, the thickness of 7 μm thick cantilever was found to be actually 6.5 μm , the 4 μm cantilever was same as specified by manufacturer and 1 μm cantilever was found to be 1.1 μm .

| Mode | 7 μm | 4 μm | 1 μm |
|------|--------------------|--------------------|--------------------|
| n | $C_{7\mu\text{m}}$ | $C_{4\mu\text{m}}$ | $C_{1\mu\text{m}}$ |
| 1 | 1 | 1 | 1 |
| 2 | 0.9128 | 0.9857 | 1.0060 |
| 3 | 0.7841 | 0.9637 | 1.0099 |
| 4 | 0.7009 | 0.9209 | 1.0134 |
| 5 | - | - | 1.0155 |
| 6 | - | - | 1.0304 |
| 7 | - | - | 1.0223 |

Tab. 3.3: The values of the calibration constant C (see Eq. 3.4)

The highly affected parameter is its quality factor. It decreases by almost 3 orders of magnitude from vacuum to air. It is considered as one of the fitting parameter while determining the resonance frequency from the frequency response curve (Eq. 3.5).

The resonance frequencies and the quality factors measured at various modes are shown in Table 3.1. The corresponding frequency values estimated theoretically from Eq. 4.1 are given in Table 3.2. The measured values deviated from estimated values. For 7 μm thick cantilever the deviation at mode 4 was about 30% from the theoretical value, for 4 μm thick cantilevers it was about 7%, while for 1 μm cantilevers at mode 7 it was about 1%. We believe that the deviation originates from defects in the cantilever. In the first mode, as the entire cantilever is vibrating with its only node near the hinge, the minor defects inside the cantilever are not contributing for the deviation. With higher modes of vibration a larger part of the cantilever participates in the movement due to twists that it has to undergo. Hence the effect of internal defects will be more pronounced at the higher modes compared to first mode. To account for such discrepancies from the measured values of higher modes of resonance we have introduced a constant C as a calibration factor as shown in Eq. (3.3). The calibration factor values obtained are shown in Table 3.3. For 1 μm they are close to 1 indicating less defects compared to 7 μm with more defects.

3.4.4 Frequency shift for mass loading

The difference in the resonance frequency values obtained before gold coating and after gold coating is plotted in Fig. 3.4 A, C, E. They clearly indicate that for each thickness layer of gold (mass addition), the change in resonance frequency increased with the mode number.

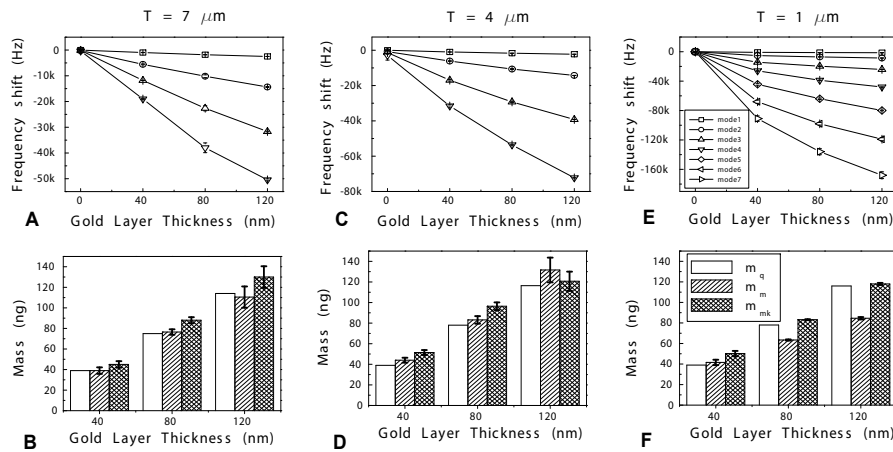


Fig. 3.4: Frequency shift measured and the corresponding mass calculated at various modes. A, C, E represent frequency shifts obtained for 40 nm, 80 nm and 120 nm thick gold layers deposited on a $7\ \mu\text{m}$, $4\ \mu\text{m}$ and $1\ \mu\text{m}$ thick cantilevers respectively. B, D, F represent corresponding average mass values calculated from all modes for each thickness. The three mass histogram columns for each gold layer thickness correspond to the values calculated considering dimensions (white column, Eq. 3.6), "mass only" change (hatched column, Eq. 3.7) and "mass & spring constant" change (meshed column, Eq. 3.8), respectively. The mass calculated from the dimensions of gold layers are 39 ng, 78 ng and 116 ng, respectively. The spring constant for $7\ \mu\text{m}$ cantilevers did not change till 120 nm of gold, but for $4\ \mu\text{m}$ cantilevers it was observed to deviate at 120 nm and for $1\ \mu\text{m}$ cantilevers already at 80 nm of gold.

Equation 3.7 and 3.8 were used to calculate the mass loaded on the cantilever. The values are compared to the mass calculated from the thickness measured with quartz crystal microbalance during deposition (Eq. 3.6). The results are plotted in a histogram as shown in Fig. 3.4 B, D, F. Each mass value is the average calculated from all the modes and the standard deviation is indicated as error bar. For a $7\ \mu\text{m}$ thick cantilever the mass measured matches quite well with the mass determined using the quartz microbalance for all thickness values of gold. For $4\ \mu\text{m}$ thick cantilever, the effect of the added layer on the spring constant is seen only at 120nm and not at 40nm and 80nm of gold layer. While for $1\ \mu\text{m}$ thick cantilever the effect on the spring constant can be observed already at 80nm of gold layer. The reference cantilevers without gold coating showed no frequency shift as expected.

3.4.5 Higher harmonics offer better sensitivity

The gold layer thickness of 40nm (distributed load of 39 ng) has resulted in "mass only" effect on all cantilevers. There was no influence of spring constant till this thickness. A 3D plot of frequency shift (actual frequency shift is negative) with mode number and cantilever thickness corresponding to 40nm of gold layer is plotted in Fig. 3.5 (unavailable values are displayed as zero). For 1 μm thick cantilever, the frequency shift of 91 kHz at mode 7 is two orders of magnitude larger than 834 Hz at mode 1. In terms of mass responsivity (inverse of frequency sensitivity), they measure 0.43 pg/Hz at mode 7 and 47 pg/Hz at mode 1. The sensitivity defined as ratio of frequency shift to unit mass loaded is a parabolic function of mode number (see Fig. 3.5).

3.5 Discussion

The three important observations in our investigation are, 1. Higher modes of vibration offer at least two orders of magnitude higher sensitivity compared to the fundamental mode. 2. The quality factor increases with the mode number thus aiding to achieve higher sensitivity. 3. The spring constant remains unaffected for a deposited distributed gold layer thickness of atleast upto 2 % of cantilever thickness.

Frequency shift of 0.8 kHz at mode 1 and 91 kHz at mode 7 was observed for 1 μm thick cantilever with 40 nm thick gold layer (Fig. 3.5A). This indicates an unprecedented increase in sensitivity by two orders of magnitude at higher modes compared to lower modes for the same amount of mass load. The corresponding mass sensitivity values are 940 ag/Hz/ μm^2 for mode 1 and 8.6 ag/Hz/ μm^2 for mode 7. This fact yields the advantage to exploit large frequency changes from higher modes and increase the sensitivity of the cantilever to measure smaller masses.

For the same 40 nm gold layer, the sensitivity of 442 Hz/ng for 7 μm , 690 Hz/ng for 4 μm and 667 Hz/ng for 1 μm at mode 4 indicates that irrespective of cantilever thickness the frequency shift obtained is about the same range specially for 4 μm and 1 μm even though their resonance frequency values are apart by 490 kHz (Fig. 3.5B and TABLE 3.1). It leads to an important conclusion that for a given length and width of the cantilever, sensitivity remains significantly same at all modes (atleast till mode 4) irrespective of cantilever thickness. The discrepancy in the sensitivity is elucidated to the fact that each array was separately coated. For a given frequency span, thinner cantilevers have more number of modes than thicker cantilevers (Fig. 6.3). This fact enables to access higher modes and exploit higher sensitivity for mass using thin cantilevers. Furthermore, upto a mass load for which spring constant remains unaffected, the sensitivity behavior is parabolic with mode number (Fig. 3.5B). The sensitivity increase is also attributed to the quality factor increase with mode number (TABLE 3.1). Similar increase in quality factor and enhanced mass sensitivity at higher modes by two orders of magnitude was also observed for point mass load on the apex of the cantilever (Dohn et al., 2005). These observations lead to an important conclusion that the mass sensitivity of cantilever sensors can be increased by working at higher modes without changing their physical parameters. Furthermore, larger physical dimensions give an added advantage of larger surface area for accommodating more adsorbates and amplify mass response.

Figure 3.4 reveals that for a gold layer thickness of atleast 2 % of cantilever thickness the spring constant value is unaffected. Increase in the effective spring constant of the cantilever compensates for the frequency shift obtained by mass change. This fact is clear already at 80 nm gold on the 1 μm thick cantilever and 120nm gold on the 4

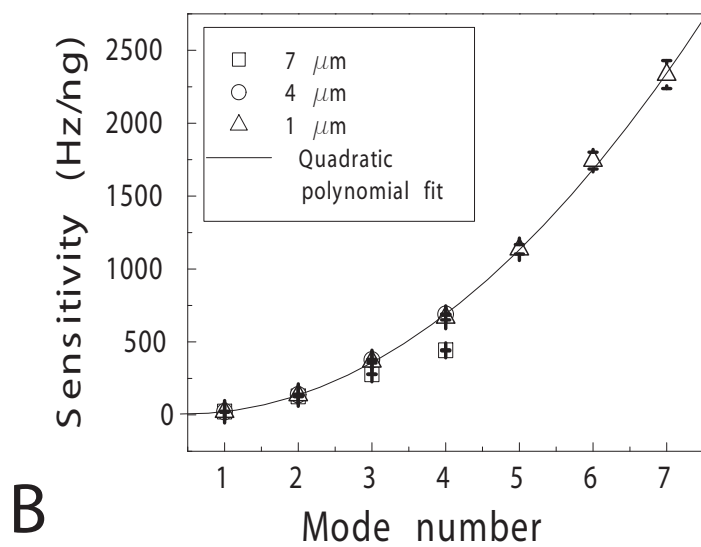
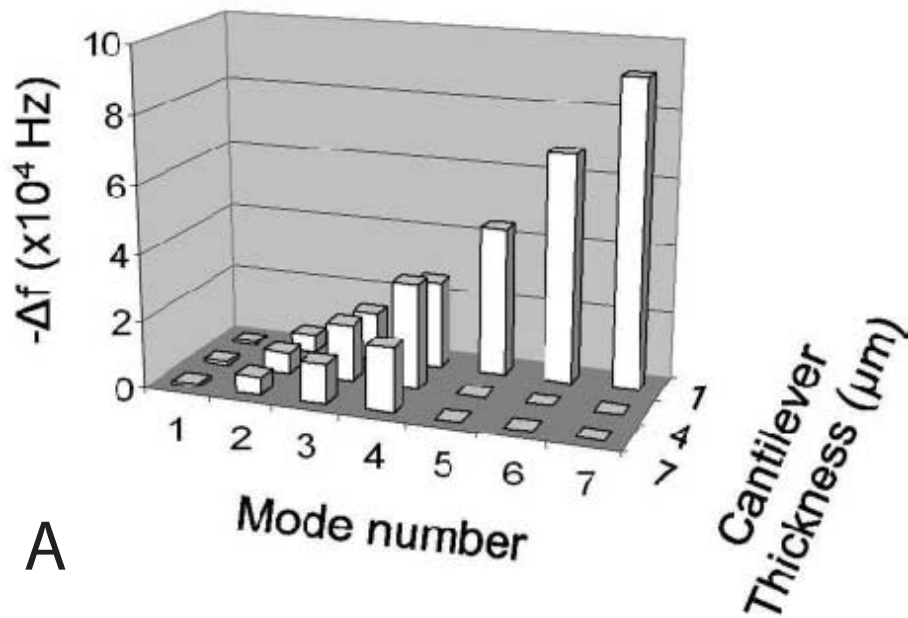


Fig. 3.5: (A) The frequency shifts measured as a function of mode number and cantilever thickness corresponding to a distributed mass load of 39 ng (unavailable values are shown as zero). (B) The sensitivity as a function of mode number is parabolic for every cantilever thickness.

μm thick cantilever. Hence, as soon as the spring constant of the cantilever starts to get affected, the linear dependence of negative frequency shift on mass ceases. The mass value calculated due to "mass only" effect (m_m) is underestimated if stiffness is affected and "mass & spring constant" effect (m_{mk}) is overestimated if stiffness is not affected. Results also imply that linear range of mass detection for thin cantilevers is smaller than those of thick cantilevers (40 nm for 1 μm cantilever and 120 nm for 7 μm cantilever). However, it should be noted that the limiting factor for maximum thickness of the deposited layer before it changes the effective stiffness of the cantilever also depends on the elastic modulus of the deposited layer. For the soft biological molecules like DNA, protein or cell, the elastic modulus is at least six orders of magnitude smaller than for gold (Takai et al., 2005). Hence for a monolayer of biological molecules on the cantilever the effect of stiffness can be neglected. The frequency shift obtained involving measurements of biological samples will be only due to mass with the present cantilevers investigated.

Using cantilever arrays, statistics of a particular behavior can be obtained in a single experiment. Furthermore, by selectively functionalizing them for sensing applications, multiple target sensing at the same time is possible including the reference for better interpretation of results. In the present investigation, we have used different thicknesses of gold layers along with bare uncoated cantilevers for reference in a single cantilever array (Fig. 3.1 B). For an array as shown in Fig. 3.2, not all the cantilevers have exactly same resonance frequency. This indicates the dependency of the resonance frequency on mechanical properties. Even though all the cantilevers are microfabricated in a similar way to obtain same dimensions, they can never be exactly the same due to process limitation. These small nuances are noted in the $< 0.1\%$ deviation of the resonance frequencies in a single array. Furthermore, absence of anomalous peaks in the resonance peak spectrum (Fig. 6.3) for the cantilevers used indicates that the spectra are devoid of any resonance frequencies from other parts of the measurement system. The amplitude distribution of the peaks is a sensitive parameter of the laser beam position on the cantilever. As the laser beam position is fixed on the cantilever apex during the entire sweep, small variation around this position results in different amplitudes of the resonance peaks. A optimized position is chosen to achieve maximum amplitude for all modes. Also, the amplitude of vibration at higher modes is large for thinner cantilevers making it possible to detect using optical techniques.

Theoretically estimated values of frequency at higher modes did not match with the measured values (TABLE 3.1 and TABLE 3.2). We attribute this to internal defects in the cantilever. These defects will affect the resonance frequencies specially at higher modes due to increase in the number of nodes and antinodes. They decrease the effective stiffness of the cantilever decreasing their resonance frequency of vibration. This argument is supported by the observed etching artifacts in cantilevers using optical microscope (figures not shown). These defects were more pronounced for 7 μm and 4 μm thick cantilevers compared to 1 μm cantilever. This may be because 7 μm and 4 μm were wet etched while 1 μm were dry etched. To compensate for such defects we have introduced a calibration factor as shown in Eq. 3.3. The calibration factors (TABLE 3.3) indicate more defects for 7 μm thick cantilever.

3.6 Conclusions

A clean frequency spectrum with peaks corresponding to various modes of vibration are obtained for different cantilever thickness. The vibrations of fundamental and next two modes were visualized using SEM. For a fixed length and width, thinner cantilevers exhibit more number of modes in a given frequency span. For a uniform gold deposition on the cantilever, the mass sensitivity increase is parabolic with mode number. A sensitivity increase of two orders of magnitude is obtained from mode 1 to mode 7 with a minimum sensitivity of $8.6 \text{ ag/Hz}/\mu\text{m}^2$ at mode 7. Our results indicate that mass sensitivity using resonating nanomechanical microcantilevers can be increased by operating them at higher modes. Thus keeping the larger dimensions of the cantilever and exploiting the larger surface area required for biological sensing.

CHAPTER 4

RESONANCE FREQUENCIES OF CANTILEVER ARRAY VIBRATING IN LIQUID

"You must be the change you want to see in the world." – Mahatma Gandhi

A study of nanomechanical cantilevers vibrating at various resonating modes in liquid is presented. Resonant frequency spectrum with 16 well resolved flexural modes is obtained. Quality factor increased from 1 at mode 1 to 30 at mode 16. The theoretical estimate of resonance frequency using the Elmer-Dreier model matches well at higher modes from mode 9. The apparent mass of the liquid dragged by the oscillating cantilevers decreases asymptotically with mode number. The results indicate that micro-cantilevers vibrating in liquid can be used as potential mass sensors for biomolecules in physiological conditions.

4.1 Introduction

The driving factors for the development of cantilever array sensors are high sensitivity, real time portability, multiple target sensing, diverse applicability and low cost. This versatile tool has already found application in the field of genomics (J. Zhang et al., 2006; Fritz, Baller, Lang, Rothuizen, et al., 2000; McKendry et al., 2002), proteomics (Arntz et al., 2003; Backmann et al., 2005), food engineering (Nugaeva et al., 2007) and chemistry (Berger et al., 1997). Surface stress (static mode) and mass change (dynamic mode) are the important parameters of interest for cantilever as a sensor (Lang et al., 2006). The focus of this article is on the dynamic mode. It is a challenging task to vibrate a cantilever array in liquid environment. Successful operation requires efficient coupling of external excitation energy to the cantilevers avoiding anomalous additional acoustic frequencies originating from liquid chamber. It also needs a bubble free fluid flow system, optimally focussed parallel laser beams and sufficient laser power to pass through air-liquid-air interface for optical detection of cantilever motion. We have successfully operated a cantilever array in liquid by overcoming these difficulties. A clear and well resolved frequency spectrum with 16 resonant modes of vibration with their corresponding quality factors is obtained. Furthermore, the knowledge of exact

mode number corresponding to the resonating frequency is very essential to determine the subsequent mass adsorption correctly. Hence experimentally obtained resonance frequency values at various modes have been compared with those obtained from analytical expressions of various theoretical models. As a result, the added apparent mass on the cantilevers at various modes is calculated.

4.2 Results

Arrays of 8 cantilevers, each 500 μm long, 100 μm wide and 1 μm thick, were used for the measurements. The laser beam deflection detection technique is adapted to monitor resonance frequencies of the eight individual cantilevers placed in a tiny chamber volume of 6 μl . Liquid was continuously flown at a rate of 10 $\mu\text{l}/\text{min}$ (T. Braun, Barwich, et al., 2005). A spectrum of the resonance peaks with corresponding phase information spanning 16 flexural modes till 1 MHz is shown in Fig. 4.1. The phase values are wrapped between 180° and -180° . A phase change of 180° across every peak with a steep slope at the peak position is clearly observed. By exciting the cantilever driven by an external piezo across the resonance frequencies, the position of the laser beam on the apex of the cantilever may not be optimal for certain modes. Hence, the laser beam is adjusted for an optimized position to obtain a significant amplitude for all the peaks corresponding to the different modes of vibration. Furthermore, the amplitude of vibration decreases with mode number making it difficult to detect further higher modes (H.-J. Butt & Jaschke, 1995). The resonance frequencies and their corresponding quality factors are shown in Fig. 4.2 and Fig. 4.3, respectively. The inset shows the exact values measured for the corresponding peaks of a single cantilever. The resonant frequencies deviated by less than 1 % among 8 cantilevers in an array indicating their similar physical characteristics. The quality factor increase from 1 to 30 for mode 1 to mode 16 indicates that damping effect from surrounding medium decreases with mode number. The difference between the two adjacent resonance frequencies increased, while the quality factors were linearly spaced.

$$f_{R,n} = \frac{\alpha_n^2}{2\pi} \sqrt{\frac{EI}{l^3 m_c (1 + \frac{\pi \rho b}{4 \rho_c h} \Gamma(f))}}. \quad (4.1)$$

where E is the elastic modulus of the material, ρ is the density of the liquid, ρ_c is the density of the cantilever, l its length, b its width, h its thickness, m_c its mass and $I = bh^3/12$ is its moment of inertia. The constants $\alpha_1 = 1.875$, $\alpha_2 = 4.694$, $\alpha_3 = 7.854$, $\alpha_4 = 11.0$, $\alpha_{5\dots n} = \pi(n-0.5)$ are solutions of the equation $1 + \cos\alpha_n \cos\alpha h_n = 0$ (Young & Felgar, 1949). Each model has different expression for $\Gamma(f)$.

The thickness of the cantilever measured by scanning electron microscopy is $0.817 \pm 0.02 \mu\text{m}$. The spring constant value calculated from resonance frequency of 4.5 kHz in air is $k = 0.018 \text{ N/m}$. The Reynolds numbers determined by $Re = 2\pi\rho f_{wat} b^2 / 4\eta$ (Sader, 1998) at various resonance modes ranges between [14, 14570]. The density and viscosity values of nanopure water used were 997.8 kg/m^3 and $9.772 \times 10^{-4} \text{ kg/m}^{-1} \text{ s}^{-1}$ respectively.

The frequency measurements were performed on various cantilever arrays. The values obtained for two such arrays are shown in in Fig. 4.6 and 4.7. The deviation of frequency at various modes is less than 1 % among 8 cantilevers indicating similar mechanical properties. The inviscid model underestimates the frequency values. The viscous model initially overestimates and at higher modes it underestimates. It matches the experimental value at mode 11. At higher modes, the best estimate is obtained by

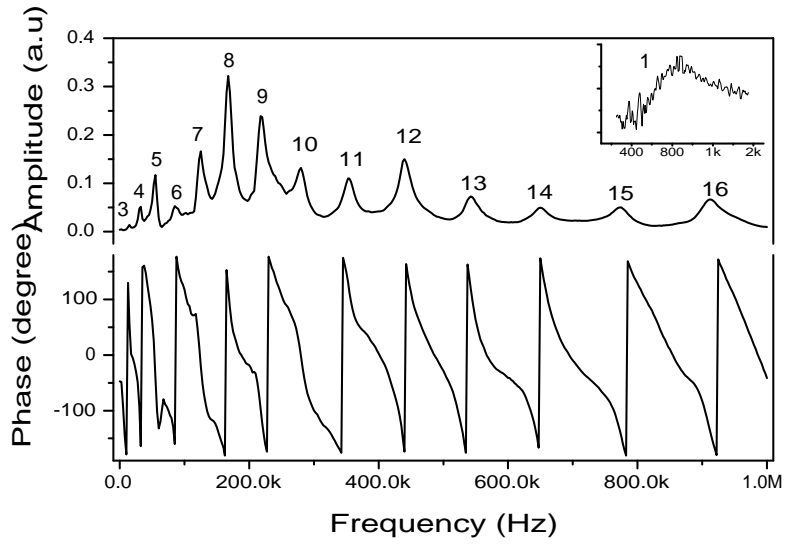


Fig. 4.1: Cantilever resonance spectrum in water

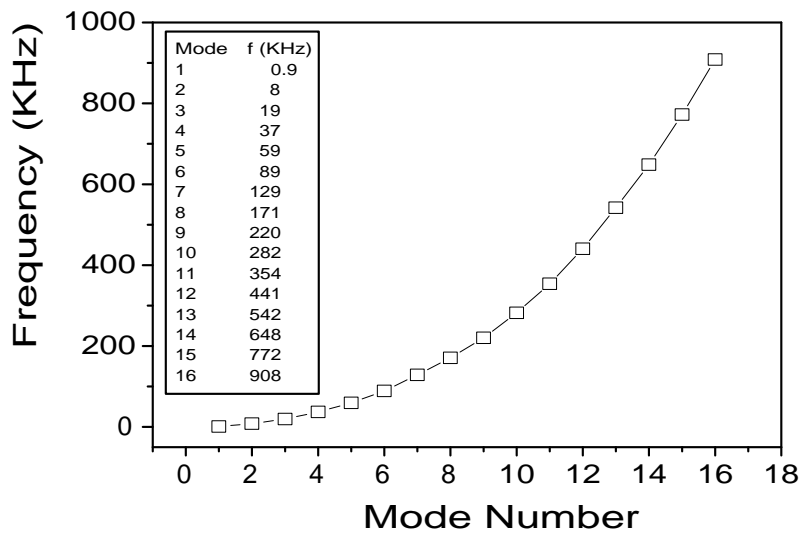


Fig. 4.2: Resonance frequency values depending on mode number

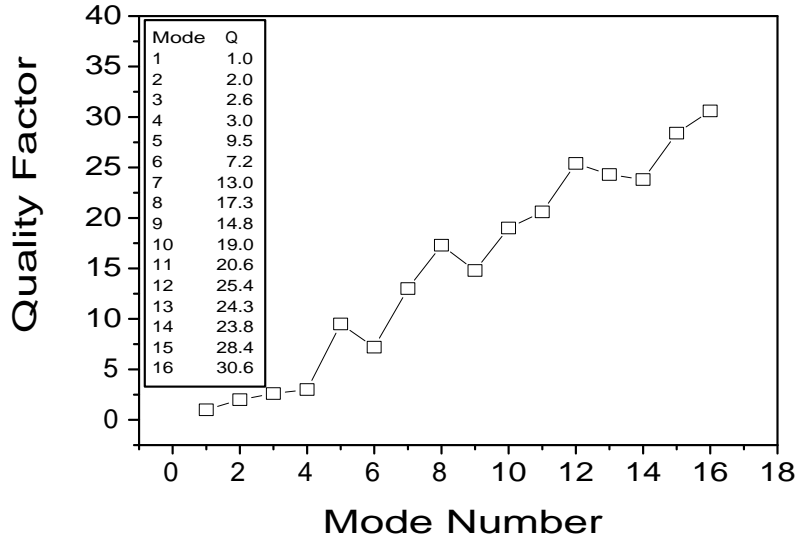


Fig. 4.3: Quality factor values as a function of vibrating mode number

the Elmer-Dreier model. The analytical expressions derived by Sader for this model were used to calculate the frequencies. Sader's extended viscous model also predicts correctly the modes following the Elmer-Dreier model.

An analytical expression is available for the viscous and the extended viscous models to estimate the quality factors. It does not exist for the Elmer-Dreier model. The estimated values by viscous model matched quite well with measured data as shown in Fig. 4.8.

Flexural modes and torsional modes estimation by the Elmer-Dreier model are plotted in Fig. 4.9. A torsional mode exist immediately after a flexural mode. However, we measured only flexural modes.

The difference in the frequency with the next higher mode value is plotted in Fig. 4.10. It linearly increases with mode number.

4.3 Discussion

For a microcantilever vibrating in fluid, there is a strong coupling between the fluid and the cantilever resulting in an added apparent mass (also called virtual mass) which cantilevers have to displace owing to the density and viscosity of the surrounding medium. Therefore, the resonance frequency values in a medium are lower compared

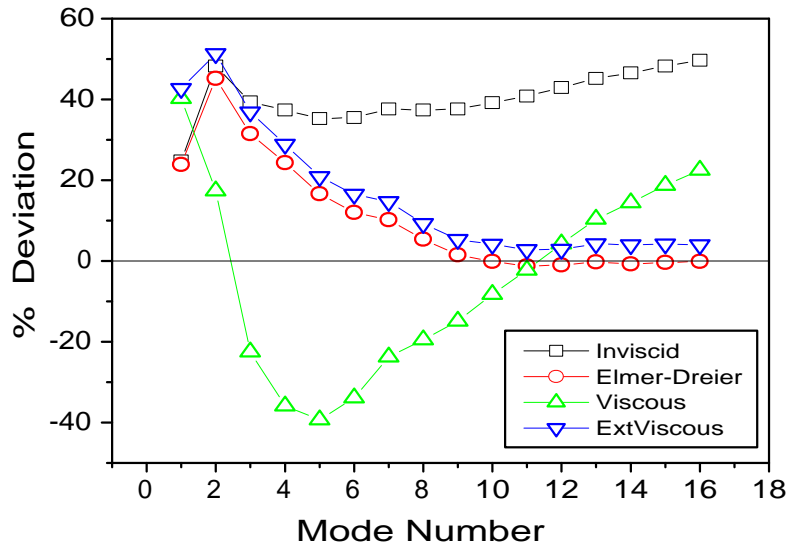


Fig. 4.4: Measured values of resonance frequencies are compared to estimated theoretical values by various models. A straight line is drawn at zero as a guide to eye

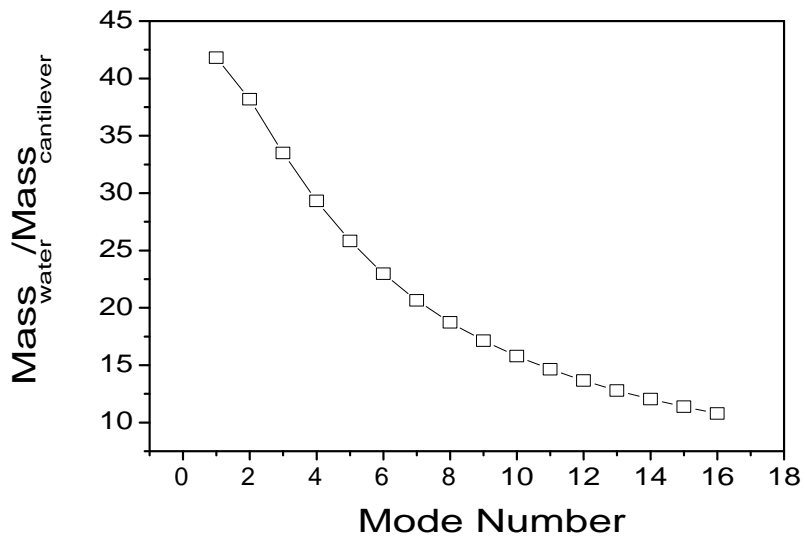


Fig. 4.5: Ratio of virtual mass of liquid to the mass of cantilever

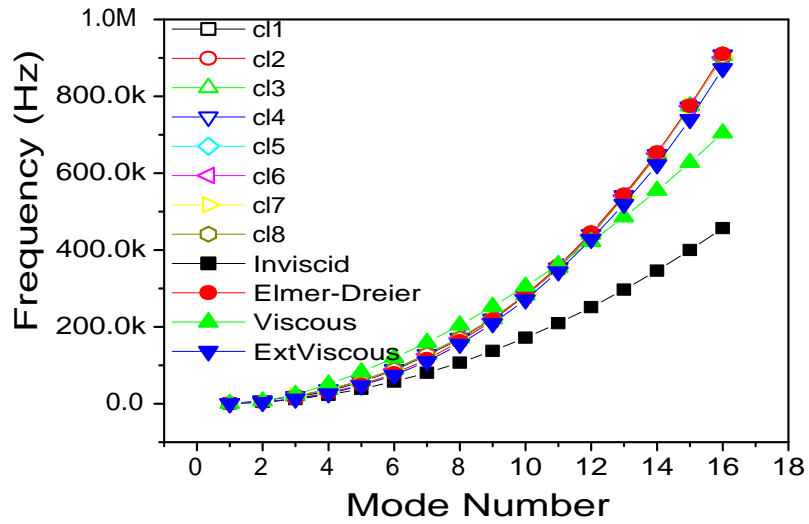


Fig. 4.6: Resonance frequency values depending on mode number for cantilever array 1

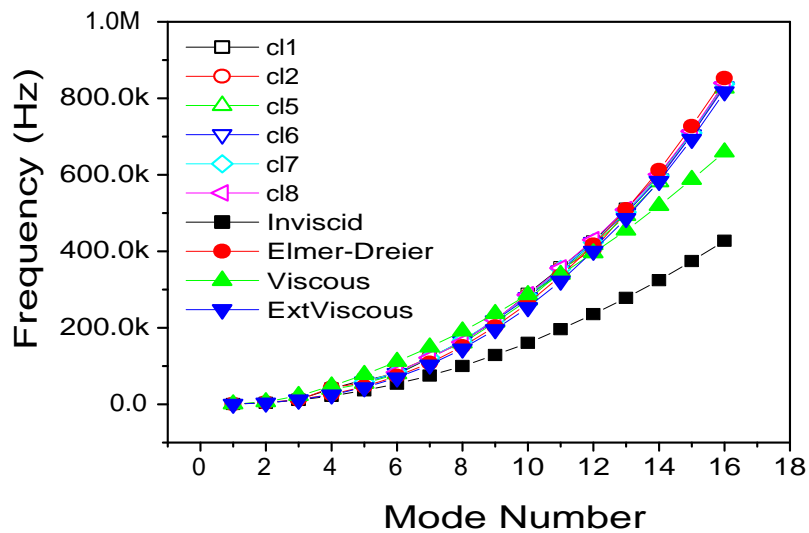


Fig. 4.7: Resonance frequency values depending on mode number for cantilever array 2

| <i>mode</i> | <i>Frequency</i> ¹ <i>Measured</i> | <i>Frequency</i> <i>Inviscid</i> | <i>Frequency</i> <i>Elmer – Dreier</i> | <i>Frequency</i> <i>Viscous</i> | <i>Frequency</i> <i>ExtViscous</i> | <i>Reynolds</i> <i>Number</i> |
|-------------|--|-------------------------------------|---|------------------------------------|---------------------------------------|----------------------------------|
| 1 | 892 | 677 | 685 | 537 | 516 | 14.4 |
| 2 | 8250 | 4244 | 4492 | 6778 | 3995 | 131.5 |
| 3 | 19395 | 11885 | 13430 | 24005 | 12368 | 314.4 |
| 4 | 36556 | 23290 | 28136 | 50509 | 26435 | 596.3 |
| 5 | 59140 | 38499 | 49553 | 82809 | 47043 | 953.5 |
| 6 | 88840 | 57511 | 78477 | 119360 | 74416 | 1429.9 |
| 7 | 128440 | 80325 | 115620 | 159340 | 109860 | 2065.0 |
| 8 | 170515 | 106940 | 161620 | 204130 | 155070 | 2739.9 |
| 9 | 220634 | 137360 | 217060 | 253050 | 344030 | 3533.8 |
| 10 | 282200 | 171580 | 282470 | 305470 | 270500 | 4526.2 |
| 11 | 353975 | 209610 | 358340 | 361950 | 356000 | 5677.4 |
| 12 | 439671 | 251430 | 445140 | 422010 | 427870 | 7066.8 |
| 13 | 539953 | 297060 | 543280 | 485880 | 519100 | 8694.4 |
| 14 | 648500 | 346490 | 653180 | 554720 | 622610 | 10401.0 |
| 15 | 773900 | 399720 | 775200 | 627260 | 739800 | 12386.0 |
| 16 | 903778 | 456760 | 909710 | 704070 | 872300 | 14570.0 |

Tab. 4.1: Comparison of frequencies till mode 16 between measured and calculated values from different models (all the frequency values are in kHz). A thickness value of $0.805 \mu m$ was used in all models.

| <i>mode</i> | <i>Measured</i> | <i>Viscous</i> | <i>ExtViscous</i> |
|-------------|-----------------|----------------|-------------------|
| 1 | 1.0 | 2.3 | 2.2 |
| 2 | 2.0 | 5.9 | 5.2 |
| 3 | 2.6 | 7.6 | 7.5 |
| 4 | 3.0 | 8.5 | 9.8 |
| 5 | 9.5 | 9.3 | 11.9 |
| 6 | 7.2 | 10.4 | 13.7 |
| 7 | 13.0 | 11.9 | 15.7 |
| 8 | 17.3 | 13.2 | - |
| 9 | 14.8 | 14.7 | - |
| 10 | 19.0 | 16.3 | - |
| 11 | 20.6 | 18.0 | - |
| 12 | 25.4 | 19.9 | - |
| 13 | 24.3 | 21.8 | - |
| 14 | 23.8 | 23.7 | - |
| 15 | 28.4 | 25.7 | - |
| 16 | 30.6 | 27.8 | - |

Tab. 4.2: Comparison of quality factor measured with calculated values by different models.

| <i>mode</i> | <i>Measured</i> | <i>Flexural</i> | <i>Torsional</i> |
|-------------|-----------------|-----------------|------------------|
| 1 | 900 | 685 | 1086 |
| 2 | 8200 | 4492 | 6850 |
| 3 | 19600 | 13430 | 19434 |
| 4 | 37176 | 28136 | 38779 |
| 5 | 59450 | 49553 | 65499 |
| 6 | 89150 | 78477 | 100180 |
| 7 | 128750 | 115620 | 143410 |
| 8 | 170825 | 161620 | 195750 |
| 9 | 220325 | 217060 | 257730 |
| 10 | 282200 | 282470 | 329870 |
| 11 | 353975 | 358340 | 412620 |
| 12 | 440600 | 445140 | 506430 |
| 13 | 542075 | 543280 | 611720 |
| 14 | 648500 | 653180 | 728880 |
| 15 | 772250 | 775200 | 858280 |
| 16 | 908375 | 909710 | 1000300 |

Tab. 4.3: Flexural and Torsional resonant frequencies (in kHz) calculated using Elmer-Drier model. The values are compared to measured flexural frequencies.

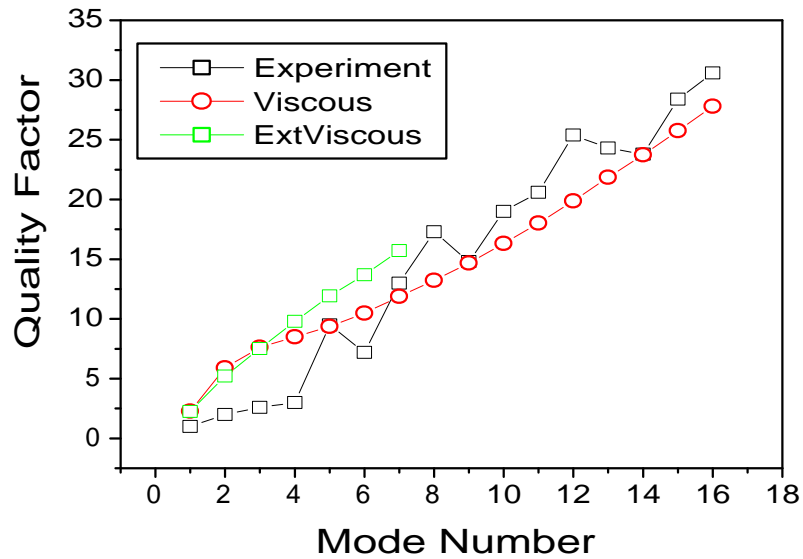


Fig. 4.8: Quality factors obtained by experiment are compared with the viscous and the extended viscous model. Quality factors beyond mode 5 for extended viscous model could not be determined.

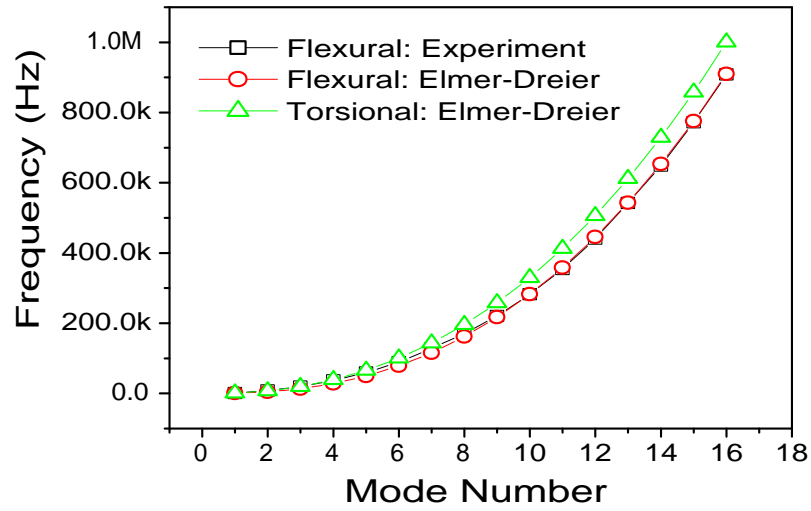


Fig. 4.9: Flexural and Torsional modes of resonance values depending on mode number

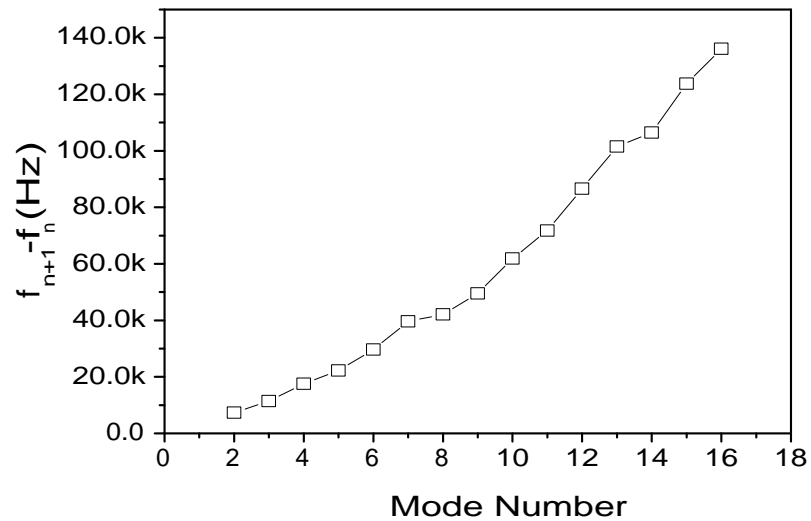


Fig. 4.10: Difference in the resonance frequency to the next higher mode

to those in vacuum. The associated quality factors of the frequency response contain dissipation of the vibrations. The motion of the fluid is complex and the modal analysis is quite difficult. Computational fluid dynamic models with sophisticated numerical techniques considering a 3D fluid motion around the cantilever have been reported (Paul et al., 2006; Maali et al., 2005; Basak et al., 2006). In our study, we used analytical expressions from different models which can be readily implemented and compared with experimental data. Models considered are the inviscid model from Chu (Chu, 1963), the Elmer-Dreier model (Elmer & Dreier, 1997) for which analytical formulas were derived by Sader (Eysden & Sader, 2006), Sader's viscous model (Sader, 1998) and Sader's extended viscous model for an arbitrary mode number which accounts for the 3D nature of the flow field around the cantilever beam (Eysden & Sader, 2007). The general expression given by all the models for resonance frequency of a vibrating cantilever at an arbitrary mode n in a medium accounting for added apparent mass is (Sader, 1998)

The percentage deviation of frequency values obtained from all the models compared to experimentally obtained resonance frequencies is shown in Fig. 4.4. A thickness value of $0.805 \mu\text{m}$ was used for all the models with the criteria of matching the number of modes and measured frequencies. Among all the models, the Elmer-Dreier model matched quite well from mode 9 and higher. This is in agreement with the validity of the theory for mode number ≥ 4 above which the effect of viscosity was neglected (Elmer & Dreier, 1997). The large deviation in the estimation of frequency by viscous model due to its validity only for low Reynolds number of the order $O(1)$. Moreover it is derived only for fundamental mode (Chon et al., 2000). The inviscid model deviated more than 40 % and underestimated the resonance frequencies. It considers a constant added apparent mass ($\Gamma(f) = 1$) for all modes, which was proved to be not the case for microcantilevers by later models. Finally, Sader's extended viscous model also seems to estimate the frequencies quite well at higher modes. The fundamental frequency matches with the viscous model and for higher modes it follows the Elmer-Dreier model. This indicates that the extended viscous model takes viscosity into consideration at low Reynolds number similar to the viscous model and neglects at higher modes similar to the Elmer-Dreier model (the definition of Reynolds number is different in the viscous model and the extended viscous model). Hence the extended viscous model describes well for both the lower and higher Reynolds number ranges for the microcantilevers used. We used the Elmer-Dreier model to calculate the added apparent mass on the cantilever and its value compared to the cantilever mass (93 ng) is shown in Fig. 4.5. The added apparent mass becomes asymptotically smaller at higher modes. A cantilever has to displace almost 40 times of its mass at fundamental and about 10 times at mode 16.

4.4 Conclusion

In conclusion, we present here a well resolved resonance spectrum for cantilevers vibrating in water. The resonance frequency values of 16 flexural modes and their corresponding quality factors in the range up to 1 MHz are measured. We found that the resonance frequencies estimated by the Elmer-Dreier model fit well at mode 9 and beyond. Sader's extended viscous model also describes the measured value well at higher modes. With the knowledge of correct mode number, the mass loaded during subsequent experiment can be discriminated from the apparent (dragged liquid) mass and can be calculated correctly. The results indicate that cantilevers can be used as a quantitative biosensor measuring real time binding kinetics of mass adsorption in

physiological environment. Moreover, mass sensitivity is at least couple of orders more at higher mode frequencies (Dohn et al., 2005) than at fundamental mode. The ultimate grand challenge is to measure the mass of single molecules in real time and simultaneously detect different types of molecules. Furthermore, if device microfabrication can reach the ultimate sensitivity of mass detection, a portable non-destructive liquid mass spectrometer can be envisaged.

CHAPTER 5

RHEOLOGICAL EFFECTS OF LIQUID ON RESONATING NANOMECHANICAL MICROCANTILEVERS

"Human existence depends upon compassion and curiosity leading to knowledge, but curiosity and knowledge without compassion is inhuman and compassion without curiosity and knowledge is ineffectual." – Victor Weiskopf

We demonstrate the effect of viscosity and density of the liquid surrounding vibrating cantilevers on the eigenfrequency, peak-frequency and damping. The effects were monitored in real time by resonance frequency and quality factor shifts during the injection of various liquids with different density or viscosity into the measurement chamber. Results show that viscosity not only influences the damping but also contributes to the added apparent mass (also referred as virtual mass) around the cantilever. This influence of viscosity increases with mode number. The effect of the liquid density contributed to the apparent mass as expected and also increased with mode number. We achieved a resolution of 3 % in viscosity and 0.06 % in density of water. Our findings suggests the use of micromechanical cantilevers in preventive medicine to measure blood rheology of patients at risk.

5.1 Introduction

Nanomechanical microcantilevers are widely used in sensing applications like mass, stress, temperature to mention a few (Lang et al., 2006). Another important application of these sensors is the rheological measurement on liquids (Bergauda & Nicu, 2000; Quist et al., 2006; Boskovic et al., 2002; Koenig et al., 2001; Oden et al., 1996). As an example, in blood rheology, viscosity is predictive of coronary heart disease, stroke, hemostatic disturbance and inflammation (Shih et al., 1994; Junker et al., 1998; Koenig et al., 1998; Baskurt, 2003). Measurement of blood rheology can provide prognostic value for diagnostics and preventive medicine.

Dynamic mode operation in liquid environment is more difficult than in air, because

of the large damping of the cantilever oscillation due to the high viscosity of the surrounding media. This results in a low quality factor Q of the oscillation and resonance frequency shift is difficult to track with high resolution.

The theoretical effect of damping on amplitude and phase response of a resonator is shown in Fig. 5.1. The higher the damping, the lower the quality factor. This results in reduction of peak amplitude and broadening of resonance curve. It effects the phase response by reducing its steepness. Apart from this an important fact to be observed is that as damping increases the peak frequency of resonance curve is no longer identical to the eigen frequency corresponding to the steepest slope (turning point) of phase curve. This implies that eigen frequency is purely a function of effective mass of the cantilever while the peak frequency is a combined effect of mass and damping.

In literature there are many reports on the study of rheological effects (Bergauda & Nicu, 2000; Quist et al., 2006; Boskovic et al., 2002; Koenig et al., 2001; Oden et al., 1996; Shih et al., 1994; Junker et al., 1998; Koenig et al., 1998; Baskurt, 2003). Generally the contributions of viscosity (η) and density (ρ) were changed together which will not reveal their independent effect on the peak or eigen frequency. Popular choice to characterize the sensors is using various concentrations of glycerol or ethylene glycol, but using different concentrations of only either of these compounds for measurement will give only cumulative effect (Oden et al., 1996; Quist et al., 2006). However, mathematical models have been reported to separate these effects from the measured value (L  v  que et al., 2000) but no experimental evidence was found.

In this article, we studied the effect of viscosity and density independently on peak and eigen frequencies. Further we examined the sensitivity of microcantilever to these effects at various modes of resonance.

5.2 Materials and Methods

Arrays of 8 silicon cantilevers, each 500 μm long, 100 μm wide and 1 μm thick, were used for the measurements. The laser beam deflection detection technique was used to monitor resonance frequencies of the eight individual cantilevers placed in a tiny chamber volume of 6 μl . Liquid was continuously flown at a rate of 10 $\mu\text{l}/\text{min}$. The cantilever array was mounted on a piezo element. A sinusoidal signal generated from a network analyzer sweeps the required frequency range vibrating the cantilevers at resonance thus giving amplitude and phase response as output. The details of the entire setup is shown elsewhere (T. Braun, Barwich, et al., 2005). At 20 $^\circ\text{C}$, different concentrations of glycerol ($\rho = 1250 \text{ kg}/\text{m}^3$, $\eta = 1.42 \text{ kg}/\text{m}\cdot\text{s}$) and ethylene glycol ($\rho = 1113 \text{ kg}/\text{m}^3$, $\eta = 18 \times 10^{-3} \text{ kg}/\text{m}\cdot\text{s}$) in nanopure water ($\rho = 997 \text{ kg}/\text{m}^3$, $\eta = 0.913 \times 10^{-3} \text{ kg}/\text{m}\cdot\text{s}$) were chosen. Glycerol at 5 % and ethylene glycol at 12% concentration had same density but different viscosity. The viscosity of ethylene glycol solution was 19 % more than glycerol solution. Similarly, glycerol at 5 % and ethylene glycol at 5 % had different density but same viscosity. The density of glycerol solution was 0.8 % more than ethylene glycol solution. The corresponding ρ and η values are shown in TABLE 5.1. Kinematic viscosity (m^2/s) of the liquids was measured using capillary viscometer (Schott-Ger  te GmbH, Langgswann, Germany). Time taken by liquid to move between two marked positions determine its value. Dynamic viscosity ($\text{kg}/\text{m}\cdot\text{s}$) is a product of kinematic viscosity and density.

During all the experiments liquids were injected in the following order: nanopure water, 5 % glycerol, 12 % ethylene glycol, 5 % glycerol, 5 % ethylene glycol and nanopure water. Amplitude and phase response were continuously recorded. NOSETools software (T. Braun, Barwich, et al., 2005) was used to analyze the spectra and extract

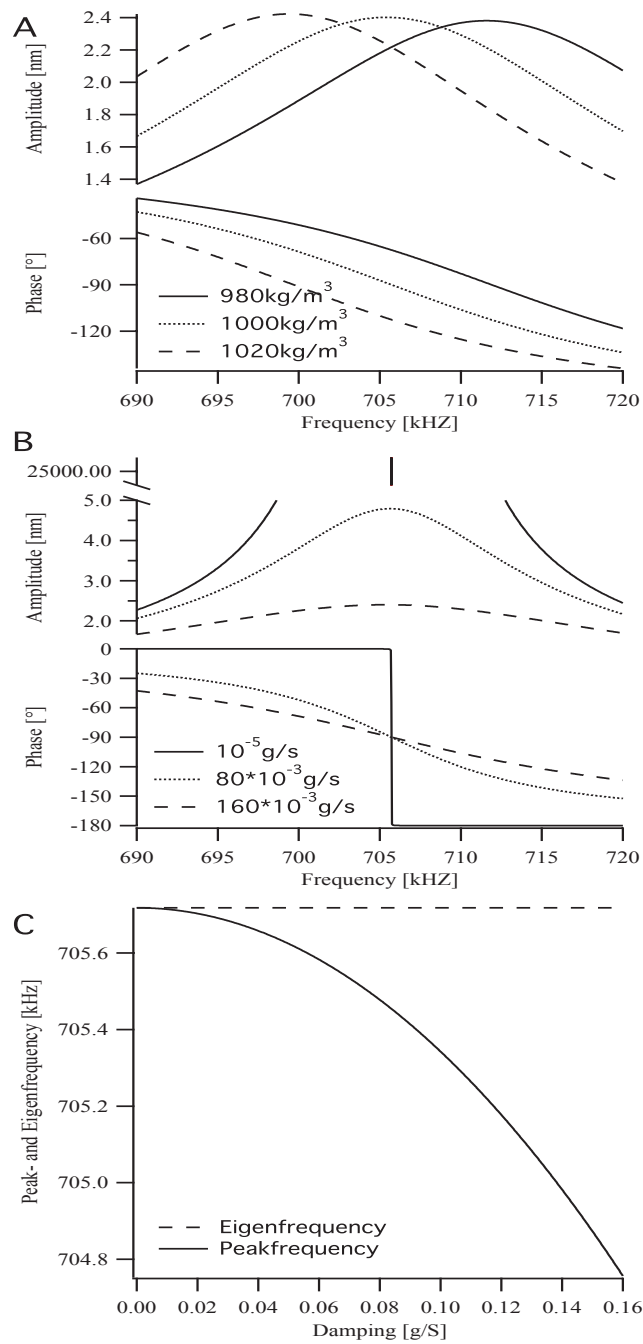


Fig. 5.1: Theoretical interpretations, (A) Increase of liquid density shifts the amplitude peak to lower frequencies, phase curve also shifts towards lower frequencies. The shape of the curves remains unaltered. (B) Increase in viscosity significantly damps the amplitude response and phase curve becomes less steep. The position of the amplitude peak and phase turning point remains constant. (C) Difference in peak frequency and eigen frequency (phase turning point). The separation between them increases with damping.

| Liquid | Density (kg/m ³) | Viscosity ($\times 10^{-3}$ kg/m-s) |
|----------------------|---------------------------------|---|
| Nanopure Water | 997 | 0.913 |
| 5 % glycerol | 1010 | 1.055 |
| 12 % ethylene glycol | 1011 | 1.257 |
| 5 % ethylene glycol | 1003 | 1.058 |

Tab. 5.1: Density and viscosity values

peak frequency from the amplitude response and eigen frequency from phase. The quality factor was also calculated for each response curve (T. Braun, Ghatkesar, et al., 2007; T. Braun, Barwich, et al., 2005).

5.3 Results

We independently studied the effects of density and viscosity of the liquid surrounding vibrating cantilevers keeping one of the parameter constant. The parameters monitored were peak frequency, eigen frequency and quality factor.

Initially, the liquid chamber around microcantilever array was filled with nanopure water. There were 16 modes (mode 1 being fundamental) of resonance frequencies in a span of 1 MHz (Ghatkesar et al., 2007). Subsequently, the effect of viscosity increase (keeping density constant) and the density decrease (keeping viscosity constant) on various modes was measured as shown in Fig. 5.2. Peak frequencies and quality factors were obtained from the amplitude response, whereas the eigen frequencies (red in color) are the steepest slope values in phase response. A peak frequency of 14.6 kHz in Fig. 5.2A represents mode 3 and 457 kHz in Fig. 5.2B corresponds to mode 12. Also the quality factor values have increased with mode number. Finally, the frequency and quality factor values are retained by injecting nanopure water.

One of the amplitude response curves and its corresponding phase response curve from the saturation region of section II (5 % glycerol) and III (12 % ethylene glycol) of Fig. 5.2B are plotted in Fig. 5.3A. These responses correspond to same density but different viscosity. It can be observed that amplitude response in higher viscous medium (red in color) has shifted to lower frequency and it became broad indicating reduction in its quality factor. The corresponding phase response has shifted to slightly lower frequency and became less steep which resulted in the cross over (marked in the figure) of low viscous phase response (black in color). Frequency shift indicates that viscosity increase contributes to an added apparent mass which the cantilever has to move; peak broadening of amplitude response or reduction in steepness of phase response indicates increased damping. Similarly, from the saturation regions of section IV (5 % glycerol) and V (5 % ethylene glycol) where density has decreased from former to later without changing viscosity, the responses are plotted in Fig. 5.3B. The amplitude response (red in color) in less dense medium shifted towards higher frequency without changing its quality factor. The corresponding phase response also simply shifted horizontally to higher frequency without any crossover. This indicates that apparent mass around the cantilever has decreased but viscosity remained constant.

The rheological effect of the liquid at the first few modes and the last few modes of

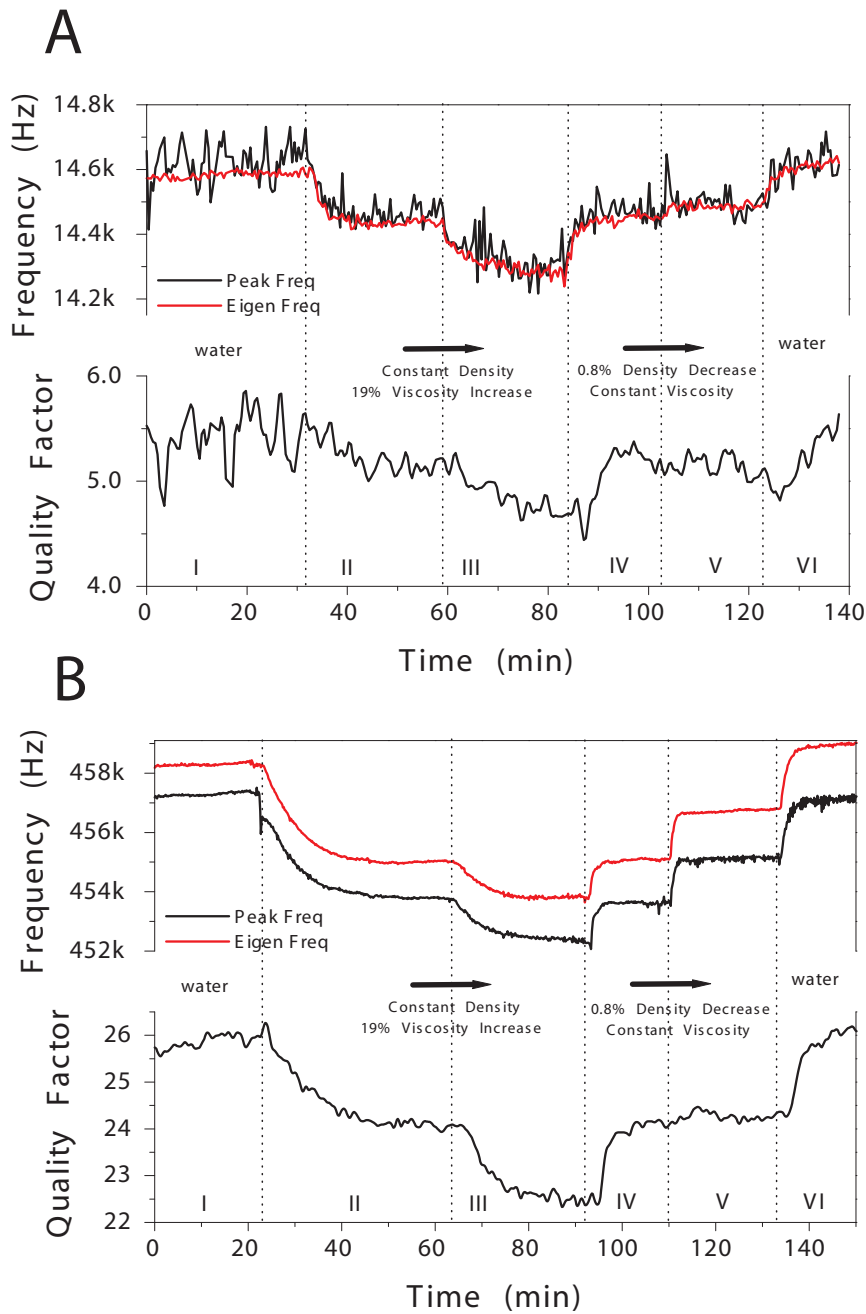


Fig. 5.2: Frequency and quality factor behavior for different rheology of the liquid A. mode 3 and B. mode 12. Various injections are separated by dotted lines I. nanopure water, II. 5% glycerol, III. 12% ethylene glycol, IV. 5% glycerol, V. 5% ethylene glycol and VI. nanopure water. Peak frequencies and quality factors are obtained from the amplitude response while eigen frequencies are extracted from the phase response. The fact that eigen frequency is higher than resonance frequency at mode 12 is due to damping effects. A 16% change in viscosity has a significant effect both at low and high modes, whereas a 2% change in density was in the noise range at low modes while it was quite significant at mode 12. Correspondingly quality factors decreased during viscosity increase and they remained constant during density decrease.

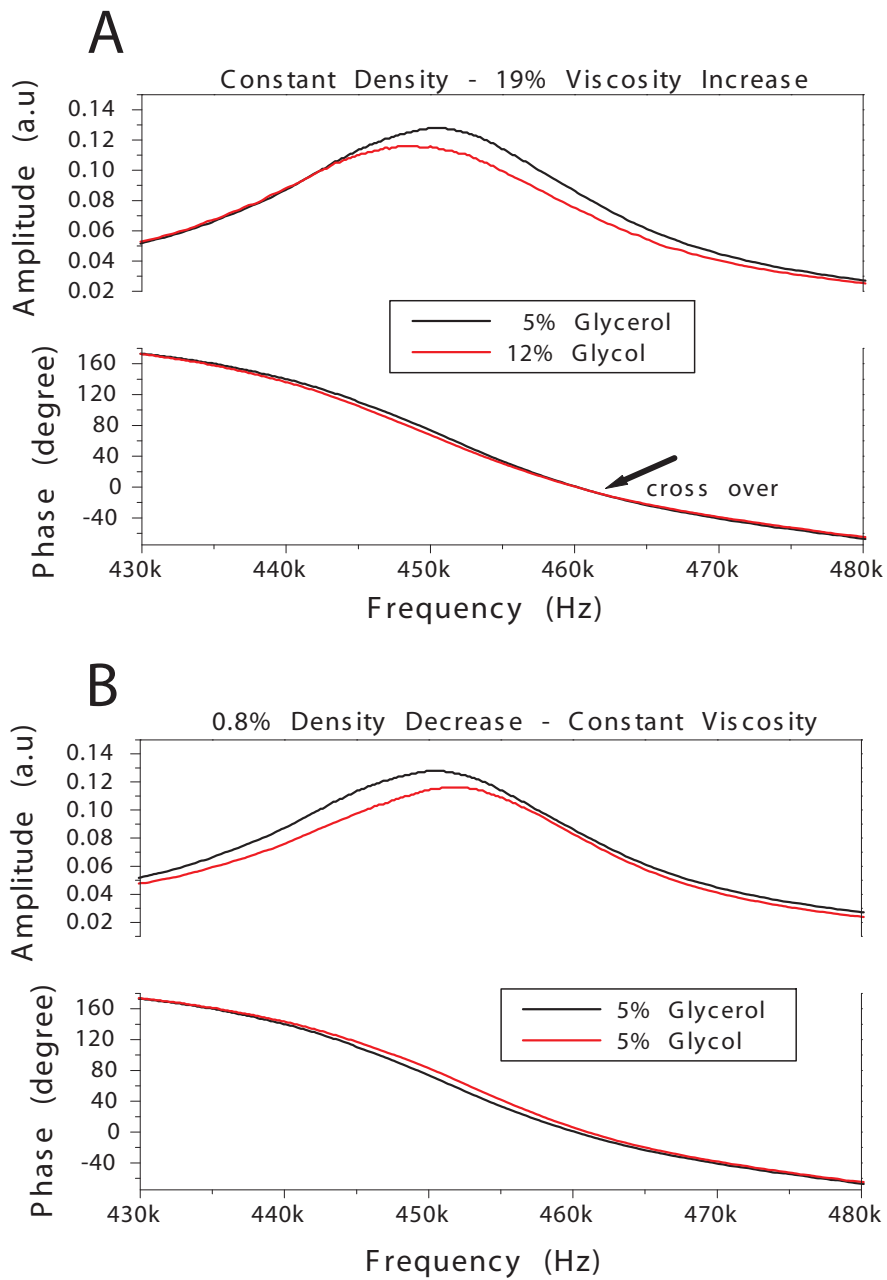


Fig. 5.3: Amplitude and phase response for (A) viscosity increase. (B) density decrease. Viscosity increase broadens the amplitude response and reduces steepness of the phase response. The arrow in panel A indicates the cross over of the phase response due to increase in damping. For decreasing density of the liquid (panel B), the amplitude response shifts towards higher frequency keeping quality factors constant whereas the corresponding phase response shifts to higher frequency. The shift of the phase response to higher frequency without changing its steepness is due to decrease in the apparent mass change around the cantilever by keeping damping constant.

resonance is shown in Fig. 5.4. The frequency and quality factor shifts plotted are the differences obtained between two equilibrium regions during flow of a particular liquid. Results obtained for increase in viscosity is shown in panel A and for decrease in density in panel B. For a viscosity increase and density remaining constant, the frequency shift is negative and the difference increased at higher mode number. This is also reflected in its quality factor behavior. Density decrease resulted in positive frequency shift due to lower apparent mass around the cantilever. Again these shifts were more pronounced at higher modes. The quality factor remained almost constant at all modes.

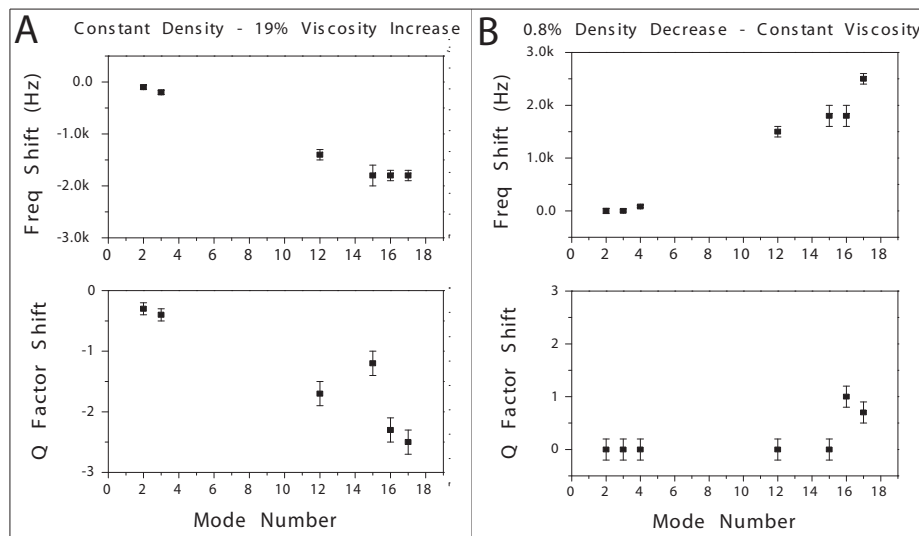


Fig. 5.4: Constant density and viscosity increase

5.4 Discussion

The main observations in this study are 1. Density change contributes to frequency shift which increases with mode number; it does not effect quality factor. 2. Apart from affecting quality factor, viscosity changes also contribute to mass change and get amplified at higher modes.

In Fig. 5.2, peak frequencies obtained from the amplitude response at mode 3 (panel A) are more noisy than at mode 12 (panel B). This is due to the fact that the amplitude response of lower modes is lower in magnitude than higher modes. This low magnitude is the result of low angles of antinodes at lower modes than at higher modes with respect to principle axis of the cantilever (Dohn et al., 2005). The number of nodes and antinodes over the length of the cantilever increases with mode number. The reflected laser beam from the apex of the cantilever will have more magnitude of deflection at higher modes owing to higher deflection angles resulting in higher magnitude of amplitude response. Amplitude response from high modes is limited either by the amount of energy needed to resonate the cantilever or the bandwidth of the electronics used. In our setup, it is limited by 1 MHz bandwidth of the amplifiers used.

In Fig. 5.2B, eigen frequency obtained from phase is greater (0.2%) than peak frequency obtained from amplitude. This is due to the fact that for a given viscosity &

density of the liquid, the amplitude response has a peak frequency which is the effect of both apparent mass and damping, while the eigen frequency from phase response is only due to mass (see Fig. 5.1). This difference at mode 3 is about 30 Hz which is clearly in the noise range and hence not clearly visible. For a viscosity increase from section II to III, apart from quality factor change, frequency also decreased indicating that viscosity contributes to mass change. Furthermore, Fig. 5.4 reveals that frequency shift obtained for viscosity change is higher at higher mode number. The change in the frequency remained at constant value at higher modes. This is an important observation as it contradicts theoretical considerations of neglecting viscous effects at higher mode numbers compared to inertial effects (Eysden & Sader, 2007; Elmer & Dreier, 1997). A 19 % viscosity increase has resulted in 1.3 kHz (± 100 Hz) frequency shift at mode 12. For a minimum detectable frequency shift of 200 Hz, a viscosity change of (3 %) can be well resolved (blood plasma viscosity for a smoker and non smoker differs by about 3 % at 1.258×10^{-3} kg/m-s (Koenig et al., 1998)). For a density change of 0.8 % from section IV to V, the frequency shift is as expected. This is due to change in the apparent mass of the liquid.

The behavior of shift in the resonance frequency and quality factor with mode number is given in Fig. 5.4. The effect of viscosity and density independently has increased with mode number. With a frequency shift of 2.5 kHz (± 100 Hz) at mode 17 for 0.8 % change in density, possible minimum detectable density change would be 0.06 % change in density.

The amplitude and phase response in Fig. 5.3 indicate that the response can be modelled by a simple harmonic oscillator at mode 12. Phase traverses by 180° during frequency sweeps indicate eigen frequency at positions where phase exhibits its steepest slope.

5.5 Conclusion

Rheology of liquids has been determined *in situ* in extremely small volumes within a few minutes using microcantilever sensors. They can clearly measure a density change of 0.06 % and a viscosity change of 3 % in water. We also conclude that viscosity contributes to mass change and is significant at higher modes. The sensitivity to changes in density increases with mode number. These sensors can be used to measure blood and plasma rheology for medical applications. The rheology of the liquids does not effect the measurements when cantilever is used as a mass or stress sensor, because for a mass/stress change on the cantilever the frequency/deflection permanently shifts to a new value after retaining the initial condition of liquid environment (buffer) around the cantilever.

CHAPTER 6

BINDING KINETICS OF LATEX BEADS BY BIOMOLECULAR INTERACTION IN PHYSIOLOGICAL ENVIRONMENT

"The four basic factors that I am convinced are involved in successful outcomes: goal-setting, positive thinking, visualizing, and believing." – A P J Abdul Kalam

Micromechanical cantilever arrays are used to measure time-resolved adsorption of tiny masses based on protein-ligand interactions. Here, streptavidin-biotin interactions are investigated in a physiological environment. A new measurement method is introduced using higher flexural modes of a silicon cantilever in order to enhance the sensitivity of mass detection. Modeling the cantilever vibration in liquid allows the measurement of absolute mass-changes. We show time-resolved mass adsorption of final (7 ± 0.7) ng biotinylated latex beads. The sensitivity obtained is about 2.5 pg/Hz measuring at a center frequency of 750 kHz.

6.1 Introduction

Proteomic and medical research has a large demand for biosensing tools which allow label-free detection of analytes in real time together with the possibility of massive parallelization of the measurement. In 1994, a new technique based on micromechanical cantilever arrays evolved (Gimzewski et al., 1994; Thundat et al., 1994). These developments provided a versatile approach for measuring forces on a nanonewton scale using cantilevers (small springs, with a width and length in the micrometer range but a thickness of 300 nm up to few micrometers). The following changes of physical properties taking place on the cantilever surfaces can be measured, even simultaneously: 1. Surface stress inducing bending of the cantilever (static mode) and 2. mass load that changes the eigenfrequencies (dynamic mode).

In recent years, it has been demonstrated in static mode that this technique is suitable to detect a single base pair mismatch in DNA hybridization experiments and to compare eight DNA sequences in parallel (Fritz, Baller, Lang, Rothuizen, et al., 2000; McKendry

et al., 2002) as well as to detect specific cardiac biomarker proteins (Arntz et al., 2003). In dynamic mode, mass determination of a single airborne virus particle was performed in vacuum (Gupta et al., 2004) and the active growth of microorganisms was measured in real time in humid air (Gfeller et al., 2005b).

In contrast to other micro-array techniques that measure mass adsorption, such as surface plasmon resonance detectors (SPR) (Nelson et al., 2001) and quartz crystal microbalances (QCM) (Bizet et al., 1998), micromechanical cantilever arrays can be operated in parallel in both static and dynamic modes (Battiston et al., 2001). Thus mass adsorption and surface stress are measured at the same time. This unique combination of measuring different physical properties simultaneously will allow the design of a new generation of bio-sensors. We envisage the investigation of membrane proteins in a more sophisticated way: Many of the receptors bind ligands detectable by a mass change in dynamic mode. At the same time they transmit an external signal into the cell, causing conformational changes (Alberts et al., 2002) that are observable in parallel in static mode (T. Braun, Kaufmann, et al., 2005).

Until now, dynamic mode measurements with cantilever arrays were restricted to vacuum or gaseous environments. However, bio-sensors are required to operate in aqueous solutions. Dynamic mode measurements in fluid still represent a challenge mainly because of the damping of the cantilever oscillation caused by the liquid.

Due to the inertial effect of water molecules in the fluid, the effective mass of the vibrating cantilever will increase. This results in lowering of the resonance frequency. The additional mass the cantilever experiences apart from its solid mass is termed as added apparent mass. Other authors have interpreted it as co-moving mass or virtual mass (R.-J. Butt et al., 1993; Chen et al., 1994; Elmer & Dreier, 1997; Weigert et al., 1996).

In this article we report time-resolved mass adsorption measurements of biofunctional latex beads in a physiological environment using the biotin-streptavidin interaction. Parallel measurements of this interaction are performed using sensitized and in situ negative control reference cantilevers to provide differences in mass responses. Furthermore the proposed theory allows the recording of absolute mass-changes on the cantilever in real time.

6.2 Theory

Here we present a quantitative description of a cantilever vibrating in liquids for higher modes. The vibration dynamics of a cantilever in vacuum are characterized by the equation of motion, which is given by

$$EI \frac{\partial^4 u(x, t)}{\partial x^4} + C_0 \frac{\partial u(x, t)}{\partial t} + \frac{m_c}{L} \frac{\partial^2 u(x, t)}{\partial t^2} = 0. \quad (6.1)$$

The first term represents the restoring force per unit length, whereas EI is the flexural rigidity, with E Young's modulus and I the moment of inertia. C_0 is the intrinsic damping coefficient per unit length that describes internal losses, m_c is the mass of the cantilever

and L the length of the cantilever. $u(x, t)$ is the deflection of the cantilever perpendicular to the cantilever axis, whereas x is the coordinate along the cantilever axis and t is time.

We focus on cantilevers vibrating in a liquid environment and driven by a piezoelectric crystal plate, which generates an external periodic force to the cantilever.

In liquid, the motion of the cantilever experiences more resistance, because of increase in its effective mass. The apparent added mass of liquid m_l on the cantilever results in an additional inertial force $g_i = -\frac{m_l}{L} \frac{\partial^2 u(x,t)}{\partial t^2}$ (Kirstein et al., 1998).

In a viscous fluid an additional dissipative force per unit length acts on the cantilever that is proportional to the velocity, $g_v = -C_v \frac{\partial u(x,t)}{\partial t}$, where C_v is the dissipation coefficient. Taking into account the forces g_i and g_v as well as $F(x,t)$, an external periodic force per unit length in Eq. (6.1), the equation of motion of a cantilever vibrating in liquid is expanded to

$$EI \frac{\partial^4 u(x,t)}{\partial x^4} + (C_0 + C_v) \frac{\partial u(x,t)}{\partial t} + \frac{m_c + m_l}{L} \frac{\partial^2 u(x,t)}{\partial t^2} = F(x,t). \quad (6.2)$$

In order to solve the problem of a cantilever vibrating in fluid completely, the apparent additional mass m_l of the cantilever in liquid and the additional damping force g_v have to be known, i.e. the coefficients p and C_v have to be determined.

Using the deflection $u(t)$, or rather the response of the cantilever, as

$$u(t) = u_0 \exp(i2\pi f_n t), \quad (6.3)$$

the resonance frequencies f_n can be determined.

The resonance frequencies of different modes n of the damped cantilever are the complex solutions of Eq. (6.2), which are as follows:

$$f_n = \frac{1}{2\pi} \left(\sqrt{\alpha_n^4 (2\pi f_0^*)^2 - \gamma^2 + i\gamma} \right). \quad (6.4)$$

The damping factor γ is defined by

$$\gamma = \frac{C_0 + C_v}{\frac{2}{L}(m_c + m_l)}. \quad (6.5)$$

f_0^* is the fundamental eigenfrequency in vacuum when the mass is concentrated in one point like for a harmonic oscillator and in the absence of damping. It is given by the relation

$$f_0^* = \frac{1}{2\pi} \sqrt{\frac{EI}{(m_c + m_l)L^3}} = \frac{1}{2\pi} \sqrt{\frac{k}{3(m_c + m_l)}}, \quad (6.6)$$

where k is the spring constant given by $k = \frac{3EI}{L^3}$.

Note that the frequencies of Eq. (6.4) are identical with the resonance frequencies of a damped harmonic oscillator except for the α_n . The α_n are related to the different eigenvalues of the harmonics and are the n^{th} positive root of the equation $1 + \cos \alpha_n \cosh \alpha_n = 0$ and are fixed by the boundary conditions (Young & Felgar, 1949). ($\alpha_1 = 1.875$, $\alpha_2 = 4.694$, $\alpha_3 = 7.854$, $\alpha_4 = 11.0$, $\alpha_{5...n} = \pi(n-0.5)$.)

For a rectangular cantilever the moment of inertia is $I = \frac{WT^3}{12}$, with W the width and T the thickness of the cantilever. Thus the eigenfrequencies of a cantilever that has a distributed mass in the absence of damping are described in analogy to the model of a harmonic oscillator by

$$f_{0n} = \frac{\alpha_n^2}{2\pi} \sqrt{\frac{k}{3(m_c + m_l)}}. \quad (6.7)$$

The amplitude of the response of the n^{th} harmonics in dependence of the frequency of the driving force is given according to the model of a damped harmonic oscillator by

$$u_n(f) = \frac{u_{\max} f_{0n}^2}{\sqrt{(f_{0n}^2 - f^2)^2 + \frac{\gamma^2 f^2}{\pi^2}}}. \quad (6.8)$$

This function is also called resonance curve and has a maximum at the resonance frequency at

$$f_n = \sqrt{f_{0n}^2 - \frac{\gamma^2}{2\pi}}. \quad (6.9)$$

Owing to damping effects, the resonance frequency f_n shifts to smaller values with respect to the eigenfrequency f_{0n} . Note that throughout the paper we distinguish between the eigenfrequency f_{0n} defined by Eq. (6.7) and the resonance (peak) frequency f_n defined by the maximum of the amplitude function of Eq. (6.8), which is specified in Eq. (6.9). Distinction between these frequencies is important because the eigenfrequency is independent of the damping caused by the liquid whereas the resonance (peak) frequency is not.

The phase between response and driving force in dependence of the frequency of the driving force is given by

$$\varphi(f) = \arctan \frac{-\gamma f}{\pi(f_{0n}^2 - f^2)}. \quad (6.10)$$

The eigenfrequency f_{0n} is defined at that point where the phase curve has its steepest slope. It will be called the turning point of the curve in the following.

In this study we detect an uptake of tiny amounts of mass distributed over the entire cantilever that is due to protein interactions at the interface. Thus the total mass which has to be accelerated is increased by the uniformly loaded mass Δm distributed on the surface of the cantilever:

$$m_{\text{total}} = m_c + m_l + \Delta m. \quad (6.11)$$

Assuming that the spring constant does not change, the eigenfrequency f_{0n} of Eq. (6.7) is modified as

$$f'_{0n} = \frac{\alpha_n^2}{2\pi} \sqrt{\frac{k}{3(m_c + m_l + \Delta m)}}. \quad (6.12)$$

For $\Delta m \ll m_c + m_l$ the following approximation is valid:

$$f'_{0n} \approx f_{0n} \left(1 - \frac{1}{2} \frac{\Delta m}{m_c + m_l} \right). \quad (6.13)$$

The mass load Δm in terms of the frequency shift Δf is calculated as

$$\Delta m = \frac{2(m_c + m_l)\Delta f}{f_{0n}}, \quad (6.14)$$

where $\Delta f = f_{0n} - f'_{0n}$.

The sensitivity of a mass-loaded cantilever is defined as

$$S = \frac{\Delta f}{\Delta m} = \frac{f_{0n}}{2(m_c + m_l)}, \quad (6.15)$$

indicating that the sensitivity increases with the order of the harmonic of the cantilever vibration.

6.3 Experimental Details

Microfabricated (Micro- and Nanofabrication group, IBM Zurich Research Laboratory, Rüschlikon, Switzerland) arrays of eight silicon cantilevers of $500\ \mu\text{m}$ length, $100\ \mu\text{m}$ width, $1\ \mu\text{m}$ thickness and having a spring constant of $0.03\ \text{N/m}$ were used in all the experiments.

6.3.1 Measurement Setup

A schematic of the setup is shown in Fig. 7.3: The array with the functionalized cantilevers is directly mounted onto the piezoelectric actuator, which is excited periodically by a frequency generator. The cantilever response is read out using a beam-deflection system: The beam of a vertical cavity surface-emitting laser (VCSEL; wavelength $760\ \text{nm}$, Avalon Photonics, Zurich, Switzerland) is reflected at the tip of the cantilever towards a position-sensitive detector (PSD; Sitek Partille, Sweden).

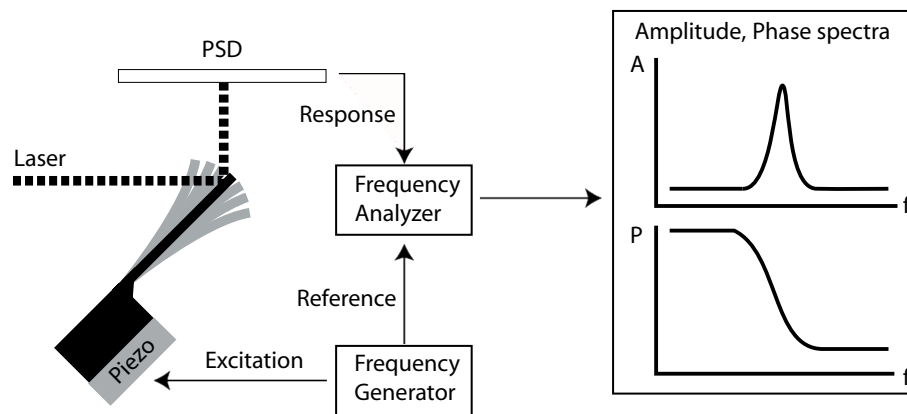


Fig. 6.1: Schematic of the setup. A frequency generator sweeps the spectrum by exciting a piezoelectric actuator located beneath the base of the microcantilever array. The response of the cantilever is optically detected with a laser using a position-sensitive detector (PSD). The frequency analyzer compares the cantilever response with the excitation from the frequency generator to determine the phase. The amplitude spectrum is recorded with the corresponding phase values.

The response of the cantilever is continuously compared with the excitation using a frequency analyzer recording amplitude and phase spectrum (Hewlett Packard, 4589A, USA). Depending on the number of cantilevers used, a spectrum is recorded every 23 s (one cantilever) or at least every 3 min (parallel measurement of all eight cantilevers). In both configurations, a sweep time of 1 s per spectrum was used. The entire setup is placed in an analysis chamber (volume $\sim 5\ \mu\text{l}$) which is kept at constant temperature (accuracy $\pm 0.02\ \text{K}$) during the experiment. A constant fluid flow rate in the cell was maintained using a syringe pump (Genie Kent, Indulab AG, Switzerland) or with a pressure driven pump-system as described (Grange et al., 2002).

6.3.2 Cantilever Functionalization

Piranha-cleaned (H_2O_2 30% : H_2SO_4 = 1 : 1) arrays were coated with a 2 nm chromium adhesion layer followed by 30 nm gold by sputtering (Baltec SCD 050 for Cr (120 mA, 0.05 mbar); Baltec MED 020 for Au (50 mA, 0.02 mbar) on both sides. Cantilever arrays were functionalized in two ways (Fig. 6.2) using a capillary device described elsewhere (Lang et al., 2006):

1) Avidin-functionalized cantilevers to bind biotinylated latex beads: On gold-coated cantilevers, home-made crosslinker dithiobis succinimidyl undecanoate (DSU) (Wagner et al., 1994, 1996)) was used to immobilize avidin. The crosslinker formed a monolayer on the cantilever gold surface via the thiol group, and avidin was subsequently immobilized by a succinimidyl group protein-lysine reaction, see Fig. 6.2 panel A.

2) With a biotin layer to bind streptavidin-coated latex beads: The freshly gold coated cantilever was incubated in a N,N-Dimethylformamide (DMF) solution containing 1 mM Biotin-HPDP (N-[6-(Biotinamido)hexyl]-3'-(2'-pyridyldithio)propionamide; Perbio Science, Switzerland) for 20 min at room temperature. For a negative control, alternating cantilevers were functionalized during 20 min at room temperature with 1 mM 11-mercaptoundecanoic acid (Sigma-Aldrich Inc., Switzerland) in DMF (Fig. 6.2, panels B and C).

6.3.3 Binding assay

For avidin-functionalized cantilevers a buffer solution containing 20 mM KPO_4 pH 7.4, 100 mM NaCl and 0.01 % NaN_3 was used during the experiment. The density ρ_f and the viscosity η_f were determined to be 1033 kg/m^3 and $9.28 \times 10^{-4} \text{ kg m}^{-1}\text{s}^{-1}$, respectively. The carboxylate-modified biotin-labeled polystyrene latex-bead suspension (Sigma-Aldrich, Inc., Switzerland) exhibiting a mean bead diameter of 250 nm was first resuspended, then diluted in the buffer described above to a final bead concentration of 6.5 pM and sonicated for 1 min.

For biotin-functionalized cantilevers: A buffer of 10 mM HEPES pH 8.0, 100 mM NaCl , 0.01 % NaN_3 , 0.25 mg/ml Casein and 0.05 % Tween-20 was used during the experiment. The carboxylate-modified and streptavidin-functionalized beads (Sigma-Aldrich, Inc, Switzerland) had an average diameter of 47 nm. During these experiments the same mass concentration and preparation as with the first binding experiments (biotin beads) and a final bead concentration of 1 nM were applied.

After the binding experiment, the cantilever array was removed from the fluid cell, washed in water to prevent salt-crystal artefacts, coated with 5 nm Pt by sputtering (Baltec, MED 020; 15 mA, 0.02 mbar) and analyzed by scanning electron microscopy (SEM, Phillips XL-30). The SEM images were analyzed with the standard particle analysis software of IGOR PRO (Wavemetrics, Portland, USA).

6.3.4 Data analysis

All data-processing algorithms were implemented in the IGOR pro data analyze environment. Recorded time series of spectra were analyzed using two methods:

1.) Amplitude peak-tracking and phase-turning point tracking (Ghatkesar et al., 2004): Here, the amplitude-peak maximum (peak frequency) and the phase-turning point (eigenfrequency) were extracted and plotted versus the time. Note that in this method all resonance peaks and phase turning points were analyzed separately. To minimize noise, the raw data was locally described with a gauss function (amplitude

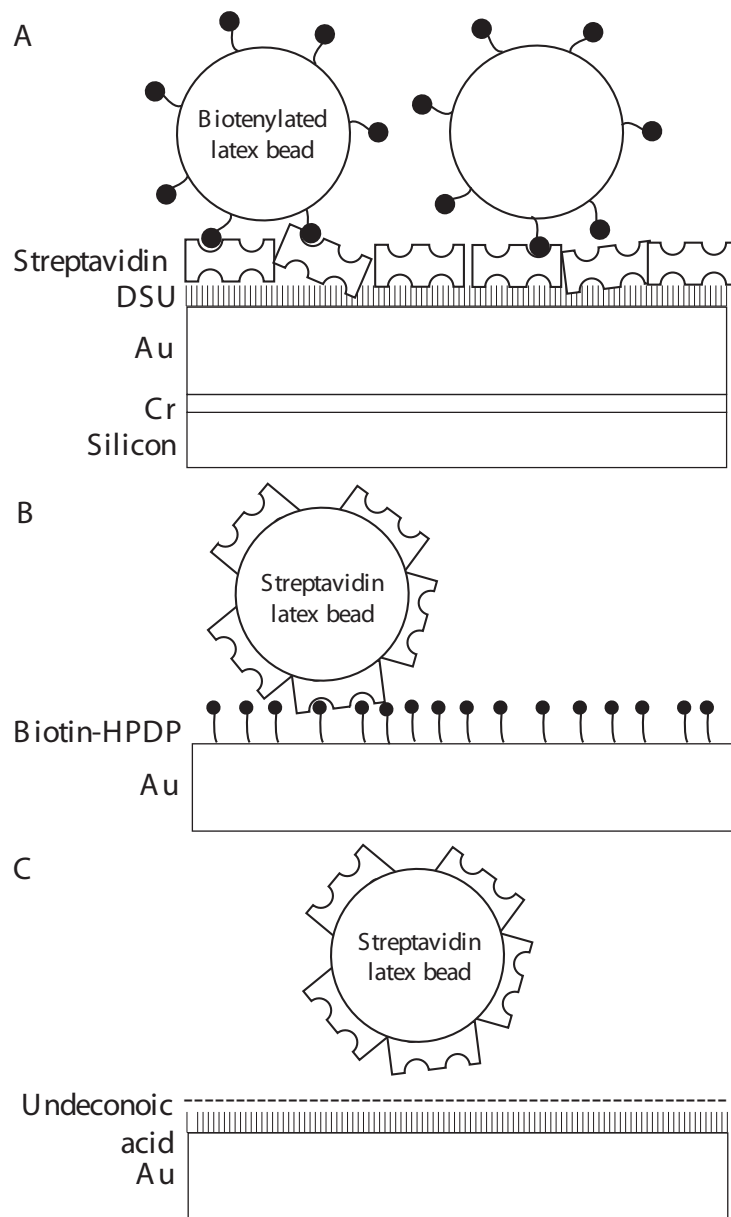


Fig. 6.2: Schematics of the functionalization methods used. Note that the silicon cantilever and the chrome adhesion layer are only shown in panel A. All binding assays are based on streptavidin-biotin interaction. A) The gold-coated cantilever was activated with DSU cross-linker, which binds to the gold via a thiol group and reacts by a succimidyl reaction with lysine groups of the protein. B) Positive functionalization for the binding of streptavidin-coated latex beads with Biotin-HPDP. C) Functionalization of the cantilever with an acid as negative control: At pH 8.0 most acid residues are negatively charged, thus repelling the sulfonate-activated latex beads by electrostatic forces.

information) or a sigmoidal function (phase information). Smoothing functions and the raw data matched well.

2.) Least-mean square fitting of the spectrum. This method involved the fitting of the amplitude and of the corresponding phase spectrum by the model described in Section 6.2. With this method, the complete spectrum was analyzed at once.

The fit function of the resonance peak of an amplitude spectrum was based on the amplitude response function $u(f)$ of Eq. (6.8). The eigenfrequencies were determined by fitting the phase spectrum with Eq. (6.10). For spectra exhibiting several peaks, a superposition of peaks or phase transitions was fitted to the complete spectra.

To determine the absolute adsorbed mass during the injection of latex beads, the system had to be calibrated. This means, initially, each spectrum acquired during the first injection step with buffer only was fitted, and various parameters were extracted for each mode. These were the eigenfrequency f_{0n} , the maximum amplitude u_{\max} , the sum of the damping constants $C_0 + C_L$, the liquid mass m_l and a phase shift in the phase spectrum. The latter is a frequency-dependent term taking a constant latency in electronic transmission of the signal into account.

In a next step, the adsorbed mass Δm was fitted for the next two injection sequences including bioreactive polystyrene beads. This was done by keeping the accelerated liquid mass constant by using the calibration from the first fit. The eigenfrequency, the maximum amplitude and the sum of the damping constants were fitted again.

6.4 Results

6.4.1 System characterization

System characterization is necessary to determine the absolute mass adsorbed in a subsequent binding experiment. This procedure is presented in Section 6.4.2. The amplitude spectra are recorded continuously together with the corresponding phase spectra. A typical spectrum including three peaks (modes 11 to 13) is shown in Fig. 6.3 with a thick gray line.

The peak frequency and eigenfrequency were determined by tracking the amplitude peaks and the phase-turning points (Section 6.3.4). The stability of the tracked frequencies was better than 0.03% over time; for a more detailed discussion see Section 6.4.2. To exclude torsional mode peaks, the square root of the eigenfrequency was plotted in dependence of the peak number. The linear relation is an indication that no torsional mode peak is included in the spectrum, Eq. (6.7).

To compare the data with the model described in Section 6.2, the data were fitted with the model. The following parameters were determined: for the amplitude as well as for the phase spectrum, the added apparent mass of the liquid and the damping factor were fitted for each mode. For the amplitude spectra, the amplitude of the peak was also fitted. For the phase spectra an additional frequency-dependent term, that takes the latency of electronics and cables into account was introduced. Fig. 6.3 shows the excellent agreement between the measured data and the fit (thin black line).

The damping factors $C_0 + C_v$ are found to vary from 1.05×10^{-4} to 1.66×10^{-4} kg/s.

6.4.2 Binding assays

Two adsorption reactions were tested: 1) The adsorption of biotinylated latex beads (diameter 250 nm) on streptavidin activated cantilevers, and 2) the adsorption of

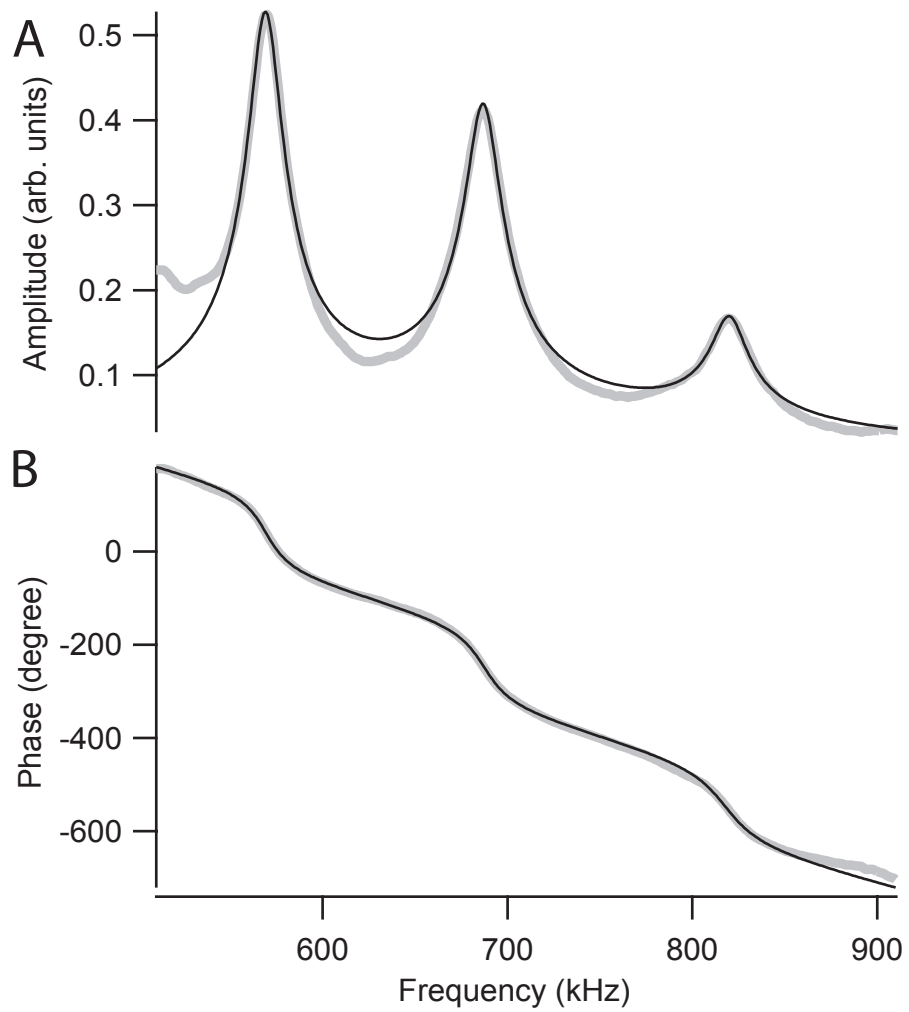


Fig. 6.3: Amplitude spectra (panel A) with corresponding phases (panel B). The raw data are shown in gray, the model fitting as thin black lines. The model is described in detail Section 6.2.

streptavidin-coated latex beads (diameter 47 nm) on biotinylated cantilevers (Section 6.4.2).

The first adsorption experiment was performed in three injection steps of 45 min each: first, injection of buffer, then the same buffer with biotinylated latex beads at a concentration of 6.5 pM, and finally buffer again. A constant flow rate of 17 $\mu\text{l}/\text{min}$ was maintained throughout the experiment, keeping the concentration of latex beads constant. The amplitude and phase spectra were recorded every 23 s.

A time-resolved plot of the frequencies is shown in Fig. 6.4 for all three modes. The eigenfrequencies are indicated by white circles (turning point tracking of the phase information) and the peak frequencies by black squares (peak tracking of the amplitude information). The lower graph shows the time evolution of the frequencies of the 11th, the middle one of the 12th, and the upper one of the 13th vibration mode. According to the three steps of injection, each plot consists of three sections of about 45 min.

The plot shows that the eigenfrequencies were found to be at higher values than the peak frequencies. The eigenfrequencies have been observed to have an average fluctuation of ± 130 Hz, whereas the peak frequencies vary by ± 180 Hz in the section before the beads were injected. This means within these 45 min the stability of the eigenfrequency was 0.015% and that of the peak frequency 0.025%.

The injection of latex beads suspension is indicated by a gray area (Fig. 6.4). During this period, simultaneously with the injection of latex-bead suspension, the frequencies shifted monotonously to smaller values. The trend in the plot of eigenfrequencies exhibited an exponential saturation behavior which was explained by the binding of latex beads to the cantilever, thus successively occupying free binding sites. In contrast to the eigenfrequencies, the peak frequencies scattered to a large extent during the time of latex-bead injection.

In the last section, while the fluid cell was flushed with buffer, the peak frequencies became stable again, immediately exhibiting average fluctuations of ± 59 Hz. The stability of the eigenfrequencies was ± 103 Hz. The data reveal a stability of 0.015% for the eigenfrequency and of approximately 0.010% for the peak frequency within this time period.

The permanent decrease in the frequency after bead binding and flushing the fluid cell with buffer indicates that the latex beads were irreversibly bound to the cantilever surface, generating a mass load on the cantilever.

In total, the eigenfrequencies shifted by -1,555 Hz from 569,561 Hz for the 11th mode, by -2,419 Hz from 686,571 Hz for the 12th mode, and by -3,130 Hz from 819,575 Hz for the 13th mode. Correspondingly, the peak frequencies shifted by -1,689 Hz from 569,296 Hz for the 11th mode, by -2,761 Hz from 686,166 Hz for the 12th mode and by -2,814 Hz from 818,507 Hz for the 13th mode.

Kinetic model

To compare the three time-resolved measurements shown in Fig. 6.4 with each other, the eigenfrequencies were normalized for all three measured modes (Fig. 6.5).

The overlay of the three time-dependent curves confirms the equivalence of the information independent of the vibrational mode used. The normalized data are interpreted as contribution of the gradual coverage of the free biotin binding sites of the streptavidin functionalization on the cantilever during injection of latex beads. To further analyze the data, a pseudo-first-order model was fitted assuming the following: (1) The concentration of the latex beads is constant as we pump the beads through the measurement chamber. (2) The beads bind irreversibly to the cantilever. (3) The binding sites on

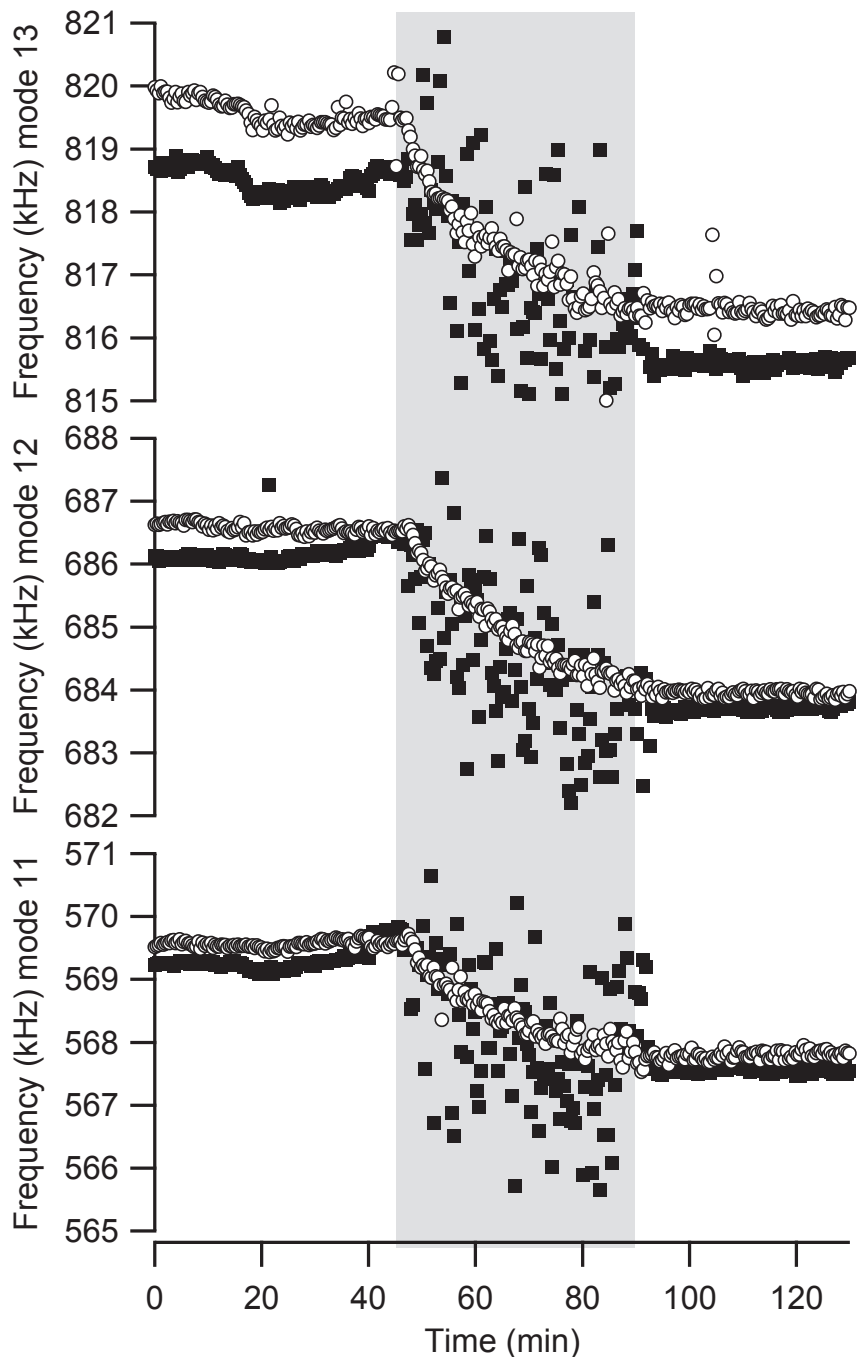


Fig. 6.4: Change of eigenfrequency (white circles) and resonance frequency (black squares) during adsorption of biotinylated latex beads. The injection time of the beads is indicated by the gray area. The panels from the bottom to top show the time evolution for the 11th, 12th and 13th mode. Note that the frequency shift increases with higher modes upon latex-bead injection. Furthermore the peak frequencies are significantly scattered during this time whereas the eigenfrequencies are recorded smoothly.

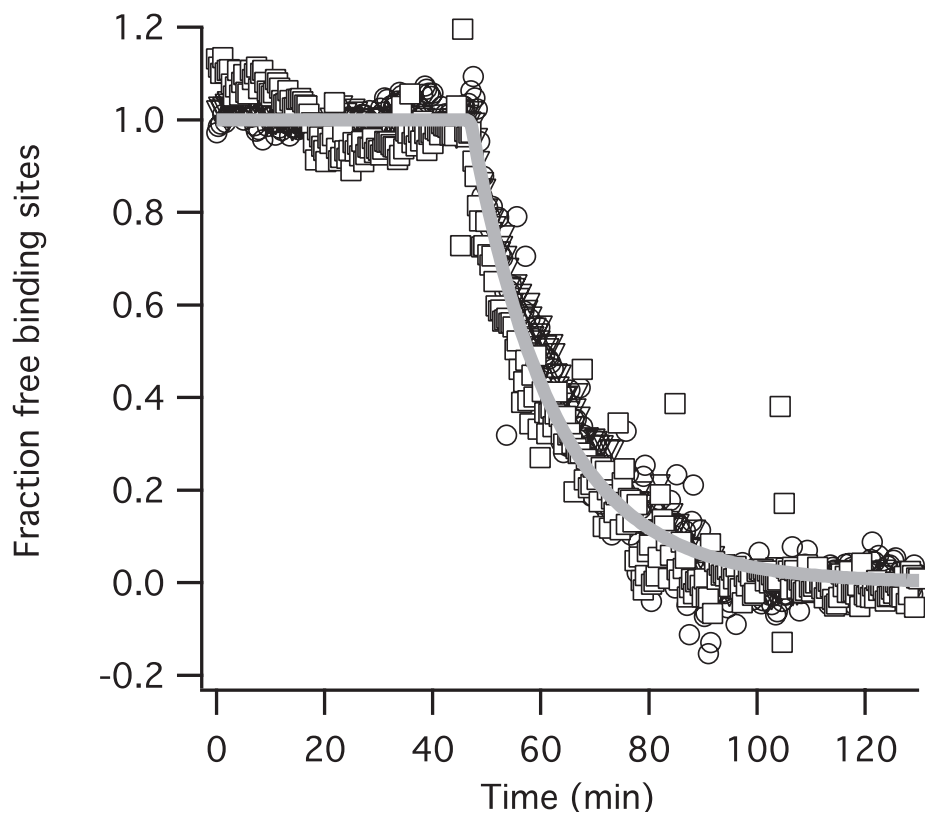


Fig. 6.5: Comparison of the frequency shifts upon mass load for different modes. The raw data of the frequency shifts have been normalized and represent the fraction of the free binding sites assuming that the cantilever is fully saturated with latex beads at the end of the experiment. Circles: mode 11; triangles: mode 12; squares: mode 13. A pseudo-first-order kinetic model was fitted to the data (thick gray line).

the cantilever are all occupied after 45min at the end of the experiment. Therefore the binding rate of the latex beads is proportional to the free binding sites, and the bead concentration is part of the rate constant. Consequently, a single parameter exponential decay, $B_{\text{free}} = B_0 e^{-\tau^* t}$, was fitted to the average of the normalized binding curves. An adsorption rate of $\tau = 0.06 \text{ min}^{-1}$ was measured. The concentration-independent rate constant is $\tau^* = 9.23 \times 10^9 \text{ M}^{-1} \text{ min}^{-1}$.

Absolute mass calculation

Each spectrum of the time series of phase and amplitude spectra was fitted using the model described in Section 6.4.1. For the calculation of the absolute mass, the previously determined added apparent mass is kept constant, but an additional mass term for the adsorbed mass is fitted, Eq. (6.11). The time-resolved absolute-mass increase during latex-bead adsorption on the cantilever is shown in Fig. 6.6A. The trend of the two curves obtained from the amplitude fits and from the phase fits is similar: a mass adsorption of $(7 \pm 0.7) \text{ ng}$ beads was measured as extracted from the fits of the phase information. However, the increase of the mass for the phase fit is $\sim 0.7 \text{ ng}$ larger than that for the amplitude fit.

The estimated number of beads of the adsorbed mass is 8 beads per μm^2 , assuming a bead density of 1050 kg/m^3 and a bead diameter of 250 nm.

After the experiment, the cantilever was removed from the fluid-chamber, dried, coated with 5 nm Pt, and imaged in the SEM. The particles were counted, yielding a coverage of 4 particles per μm^2 on average in different experiments. However, bead counting using SEM images was not very reproducible because shear forces often caused washing effects (Thomas et al., 2004) during sample preparation for the SEM: coating with latex beads was not homogeneous. We observed areas without any beads surrounded by areas with very high bead densities, followed again by an average bead density. Furthermore, the counting algorithm tends to underestimate the beads on a cantilever as beads sitting on top of each other are not counted, but have regularly been observed in the images.

Differential measurement

The second adsorption experiment was performed analogously to the first adsorption experiment but with smaller (47 nm) streptavidin-coated beads, using sensor and reference cantilevers: The sensor cantilever was functionalized with biotin (Fig. 6.2, panel B) and the negative control (reference lever) with an acid (11-thio-undecanoic acid, Fig. 6.2, panel C) introducing a negative charge on the cantilever repelling negatively-charged latex beads.

The measurements revealed a clear decrease of the eigenfrequency of the biotin-functionalized cantilever of 550 Hz compared with the non-measurable shift of the control cantilever (Fig. 6.7). Note that both cantilever eigenfrequencies were read out in parallel from the cantilever array and that the measurement was done in presence of an other protein (0.25 mg/ml casein) and detergent (0.05% Tween-20). In addition, the corresponding mass increase was determined by fitting the model to the phase information obtained from the sensitized cantilever. The mass increase on the cantilever exhibits the same qualitative behavior as the turning point tracking method. A mass increase of $(1.66 \pm 0.564) \text{ ng}$ was observed.

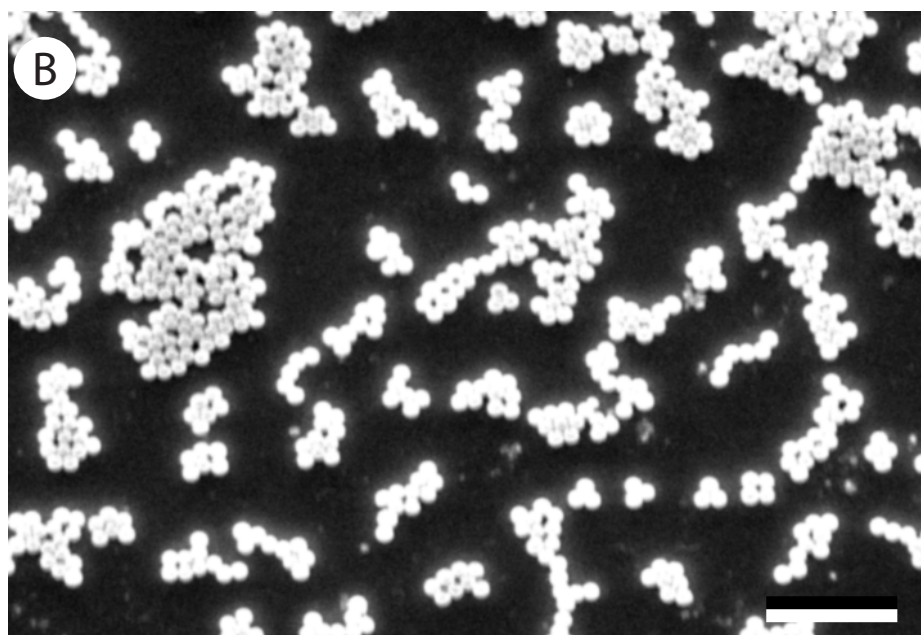
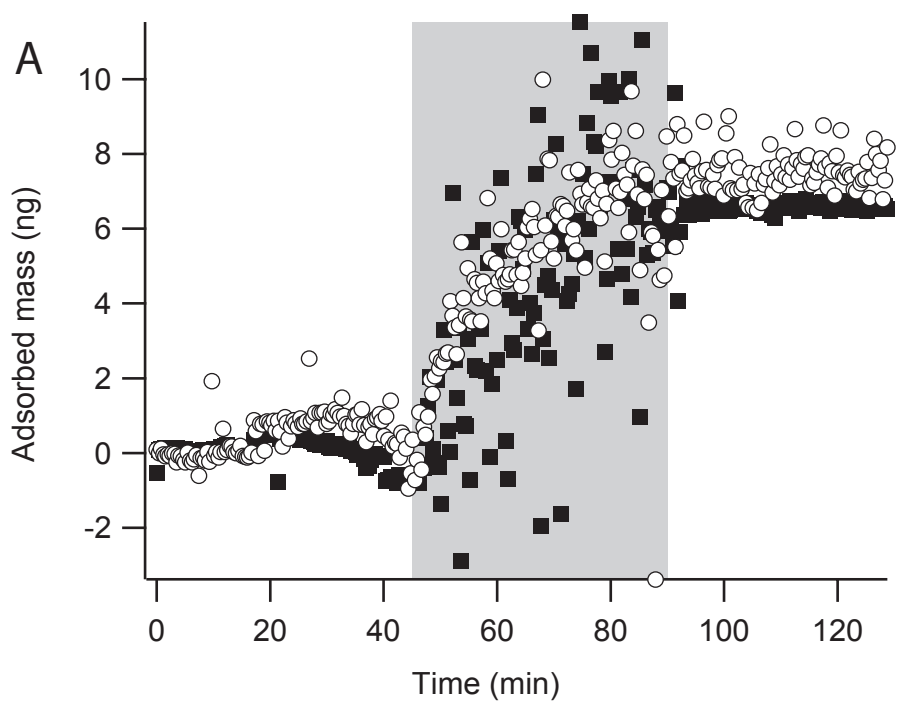


Fig. 6.6: Panel A: Absolute adsorbed mass determined by fitting the model to the phase information (white circles) and the amplitude spectrum (black squares). The gray area indicates the time frame of latex-bead injection. At the beginning of the experiment, the added apparent mass was determined with the first spectrum of the experiment. Note that every point corresponds to a fit of a complete amplitude or phase spectrum including modes 11 to 13. Panel B: Scanning electron micrograph of a typical cantilever covered with latex beads (diameter: 250nm) after experiment. The scale bar corresponds to $2\mu\text{m}$.

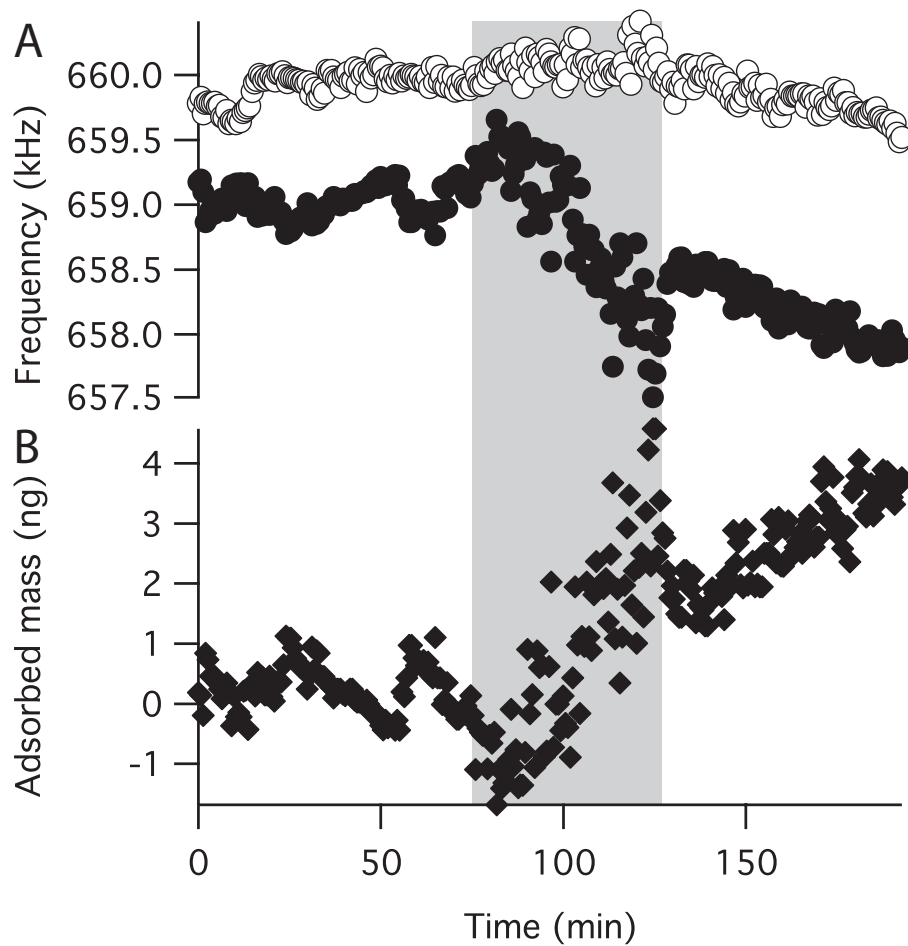


Fig. 6.7: Parallel and differential adsorption measurement of streptavidin-coated beads. Panel A: Change of eigenfrequency during streptavidin adsorption. Injection of beads is indicated by the gray area. Time evolution of the eigenfrequency extracted from the turning point of the phase. Black circles: Eigenfrequency of the biotin-functionalized cantilever. White circles: Eigenfrequency of a blocked cantilever. Panel B: Absolute mass adsorbed on the cantilever measured by fitting the phase information of panel A with the model.

6.5 Discussion

Here we describe experiments to measure mass adsorption under physiological conditions in real time. Two methods were used to analyze the time-series of recorded spectra (Fig. 7.3): The first method reads out peak and eigenfrequencies (method 1, Section 6.3.4), the second determines the absolute adsorbed mass (method 2).

The analysis of the frequency in dependence on time (method 1) revealed a clear shift to lower frequencies upon latex-bead adsorption. A clear and exponential decay of the eigenfrequencies immediately after bead injection was observed following a saturation behavior. This was seen by a shift in eigenfrequency and peak frequency (Fig. 6.4). Thereby, three phenomena were observed: (1) The frequency shift upon mass binding increased for higher modes. (2) The values of the eigenfrequency (determined from the phase data) were higher than those of the peak frequency (determined from the maximum peak amplitude). (3) During bead injection, the peak frequencies from the amplitude information scattered significantly, whereas the eigenfrequencies obtained from phase information were recorded smoothly.

Phenomenon 1 confirmed Eq. (6.15), which describes the enhanced mass sensitivity of cantilever vibrations at higher modes. Phenomenon 2 proved Eq. (6.9), namely, that the damping shifts the peak frequencies to lower values with respect to the eigenfrequencies, which are independent of damping. The last phenomenon, the scattering of the peak frequencies, was due to significant noise in the amplitude spectra during bead injection. This was interpreted as a rapid change of the external damping C_v during the one-second-long sweep of the spectrum. The damping fluctuation was due to the change of the interaction of the cantilever with the surrounding medium, in our case, the collisions of the 250-nm latex beads with the 1- μm -thick cantilever resulting in a higher noise level. This observation is completely described by the theory (see section 6.2). Therefore we conclude that the eigenfrequencies should be measured instead of peak (resonance) frequencies to obtain a better signal to noise ratio.

Normalization of the extracted frequency changes revealed clearly that the information obtained at different modes is equivalent (Fig. 6.5). Therefore an evaluation of more than one peak minimizes the error of the data interpretation (fraction of binding sites, mass-adsorption determination).

To determine the adsorbed mass (method 2), the added apparent mass due to liquid has to be considered. This was done by a least mean square fit of the phase and amplitude data before the latex beads were injected. For every mode, the added apparent mass was determined.

It was found to be $\sim 80 \mu\text{g}$ for a 1- μm -thick ($\sim 6 \mu\text{g}$) cantilever. In other words, effective mass of the cantilever increases by about 13 times when taken from air to fluid (in our case buffer).

We assume that during the latex-bead experiment, the thickness of the water layer is not changed because the molecules or the latex beads, are much smaller and the measured added apparent mass is much larger than the adsorbed mass Δm . This allows a direct tracking of newly and gradually adsorbed mass by fitting the phase spectra while keeping the added apparent mass on the cantilever due to the liquid constant.

The limitations of our model are the assumptions that the binding mass is distributed homogeneously along the entire cantilever and that the cantilever is perfectly rectangular-shaped. Furthermore we assume that the cantilever spring constant k does not change throughout the experiment. Intuitively, at a complete coverage of the cantilever surface with the analyte, the spring constant k might increase, which means that the cantilever gets stiffer.

The development of the mass increase in time displayed in Fig. 6.6 (method 2) shows the same qualitative behavior as the changes of the eigenfrequencies (method 1) observed during latex-bead adsorption do, Fig. 6.4. As expected the masses determined from the amplitude information scattered more during latex-bead injection (see discussion above). Furthermore, the final mass differs by -0.7 ng ($\sim 10\%$) when extracted from the amplitude information rather than from for the phase data. This can be explained by the fact that the damping factor also varies during the fitting of the amplitude information: The shift of the peak frequency can be interpreted as an increase in mass but also in damping. Therefore fitting the amplitude information tends to overestimate damping and underestimate adsorbed mass.

The number of latex beads as counted from the SEM images of the cantilever used and the estimated adsorbed mass thereof corroborate the mass determined by method 2. This is also in good agreement with calculations for the maximum possible number of binding sites on the cantilever assuming a perfect hexagonal arrangement (1.85×10^6 beads/cantilever). Compared with our data, this means that 45 % of the cantilever was covered with beads.

Combining the kinetic model evaluating the eigenfrequencies (method 1) with the absolute mass evaluation (method 2) allows a new level of quantitative data analysis for biological reaction. The number of adsorbed beads can be calculated (8.58×10^5 for the entire cantilever). Thus, absolute rates (number of beads) adsorbing to the cantilever for every point in time during the adsorption experiment can be given.

We presented also the differential measurement between positive and negative control functionalized cantilevers in a complex mixture of latex beads (47 nm in diameter), protein (0.25 mg/ml casein) and detergent (0.05% Tween-20), see Fig. 6.7. These data demonstrate the potential of our technique for massive parallelization and real-time measurements with high precision to measure absolute masses. High-density two-dimensional arrays of cantilevers already have been presented (Despont et al., 2004), and there is in principle nothing that would preclude going even to three-dimensional cantilever-array stacks.

The sensitivity of our technique is 220 to 400 Hz/ng, depending on the oscillation mode measured, Eq. (6.15). This corresponds to a sensitivity of 2.5 pg/Hz at a center frequency of about 750 kHz. The sensitivity of our measurements (Fig. 6.6) per sensor area is $70 \text{ fg}/\mu\text{m}^2$ or $0.025 \text{ fg}/(\mu\text{m}^2 \text{ Hz})$, taking into account the double-sided functionalization of the cantilever. Furthermore we detected latex-bead particles in the low picomolar range in a $5 \mu\text{l}$ analysis chamber.

As an outlook, we expect a resolution in the frequency range of 0.01 Hz, as reported earlier using a phase-locked loop system (PLL)(Tamayo et al., 2001)). This would correspond of a mass resolution of 25 fg or $0.25 \text{ ag}/\mu \text{ m}^2$, using a PLL operating at around 750 kHz. The resolution can also be increased if the measurements are done at higher frequencies. Using a PLL would also increase the resolution in time: As the damping in the system is high, a fast tracking in the millihertz range should be feasible. For measurements of the absolute mass, the frequency changes recorded in this way can be calibrated by the method described above (method 2).

It is interesting to compare our data with the sensitivity and resolution of other micro-array techniques such as surface plasmon resonance (SPR) imaging and quartz micro-balance (QCM) techniques. A direct comparison with QCM, thus measuring frequency shifts, is possible: A recent publication (Xiaodi et al., 2005) described a sensitivity of $0.17 \text{ fg}/(\mu\text{m}^2\text{Hz})$ measured at frequencies of up to 35 MHz under physiological conditions. For SPR, a comparison is more difficult because different physical properties are measured than in our technique and there is no absolute relation

between the measured signal and the adsorbed mass. The resolution of SPR in general is supposed to be around $1 \text{ ag}/\mu\text{m}^2$ (Homola et al., 1999).

6.6 Conclusions

A simple and efficient technique is proposed to measure time-resolved mass adsorption independent of the chemical nature of the adsorbant. The absolute bound mass could be measured at a sensitivity of 2.5 pg/Hz at a center frequency around 750 kHz . This micro-array technique combines a potential high-throughput screening method with high-precision mass measurement under physiological conditions. The expected resolution is comparable to or even better than SPR, and the sensitivity is better than that obtained in optimized QCM measurements. Measuring at higher frequencies will further improve sensitivity and mass resolution. Furthermore, measuring in combination with other nano-mechanical property changes such as surface stress (combination with static mode) (Battiston et al., 2001), an even more advanced level of sensitivity and resolution can be achieved. Such a tool will be especially useful to measure membrane-protein ligand interactions.

CHAPTER 7

T5 PHAGE VIRUS BINDING TO FHUA MEMBRANE PROTEIN

"Time is nature's way of keeping everything from happening at once." – Woody Allen

The outer membrane protein FhuA was purified, reconstituted in artificial lipid membranes and functionally immobilized on cantilever based sensors. The T5 bacteriophage was used as reporter for immobilized protein functionality. Quantitative and time-resolved mass measurements of bacterial virus T5 adsorption were successfully performed. Furthermore, we were able to measure the adsorption of the low-molecular weight ligand ferrichrome.

7.1 Introduction

Biological membranes fulfill two main functions: (i) To separate the cell from the surrounding environment and to subdivide the (eucaryotic) cell into compartments. (ii) Communication and interaction with the environment or different compartments. These seemingly contradictory functions are closely related to the structural and chemical composition of biological membranes: The first is a property of the membrane lipids, which build up a hydrophobic barrier for water and water soluble solvents. The second function is primarily mediated by proteins embedded in the lipid bilayer. They are responsible for transport of matter, energy conversion, cell adhesion and signal transduction.

Therefore it is not surprising that around 30% of the sequenced genes appear to code for membrane spanning proteins. However, the knowledge about these proteins is in huge contrast to their medical importance: For instance, around 30% to 50% of all modern therapeutics are targeted to G-protein coupled receptors (GPCRs), but only 10% of all known GPCRs can be addressed by drugs (Wise et al., 2002). This finding demonstrates the high medical interest to find more drugs acting on these proteins. Two hurdles have to be overcome in the drug research to find new antagonists: First, the hydrophobic nature of the inner of biological membranes dictates the general architecture of membrane proteins: The trans-membrane part of these proteins contains a hydrophobic belt, whereas the water exposed parts are mostly hydrophilic. This amphiphilic nature of these proteins makes it delicate to work with them. Furthermore, they are highly unstable if taken out from their natural environment. Second, the lack

of suitable instrumentation limits the experimentation with these proteins and is often limited to tests with soluble protein fragments.

Membrane proteins change two, sometimes three physical properties upon ligand binding: 1. Mass change of the complex by the additional mass of the ligand. 2. Structural change of the membrane protein, by which the signal is transduced from the outside into the cell. 3. Change of the Membrane-potential due to channel openings.

We postulate that all these changes can be tracked by micromechanical cantilever arrays sensing the nanomechanical changes of these proteins as following: 1. Mass change of the membrane protein ligand complex by measuring the resonance frequency (also called dynamic mode). This allows the detection of natural ligands, antagonists (drugs) and of virus particles if the corresponding receptors are used for the sensitization of the sensor interface. 2. Structural changes can be measured by detecting the surface-stress change induced by the conformational changes of membrane proteins attached natively to the cantilever interface (also called static mode). 3. Membrane potential change or the effect of membrane potential change can be measured by controlling the electronic potential between the cantilever surface and the surrounding buffer.

Since the physical properties measured are directly correlated to biologically meaningful properties, the results can be quantitatively interpreted. This is proven for the absolute adsorbed mass (T. Braun, Barwich, et al., 2005) and for the structural changes (T. Braun et al., 2006; Y. Zhang et al., 2004).

Dynamic mode cantilever sensors were successfully used in biology to determine the mass of a single virus in vacuum (Gupta et al., 2004), the growth of microorganism in humid air (Gfeller et al., 2005a) and mass adsorption of neutravidin coated beads on biotin activated cantilevers in liquid (T. Braun, Barwich, et al., 2005).

To measure the ligand mass-adsorption in dynamic mode we have chosen the outer membrane protein FhuA from *E. coli* (Boulanger et al., 1996; Wagegg & Braun, 1981) as a test-system (7.1). This protein is responsible for the first step in the iron uptake (V. Braun & Braun, 2002) in form of ferrichrome chelated Fe^{3+} . Besides the binding of this regular ligand, a variety of effectors, mostly harmful for the bacterial cell, are using the FhuA protein as receptor: The different ligands exhibit a range of the molecular mass from low molecular antibiotics, such as rifamycin (Ferguson et al., 2001), small antimicrobial proteins (Mirocin J25, (Destoumieux-Garzón et al., 2005)), colicin M proteins up to large bacterial virus (T5-phage, (Böhm et al., 2001; Lambert et al., 1998; Bonhivers et al., 1998)). Here we report the specific detection of T5 (high mass) and ferrichrome (low mass) adsorption to FhuA sensitized cantilevers by quantitative dynamic mode measurements using cantilevers.

7.2 Materials and Methods

7.2.1 FhuA preparation

The protein was overexpressed and purified in n-Octyl- β -D-glycopyranoside (OG) as described before (Boulanger et al., 1996). The FhuA protein was complemented with isolated *E. E. coli* lipids (containing 67 % Phosphatidylethanolamine, 23.2 % Phosphatidylglycerol and 9.8 % Cardiolipin; Avanti Polar lipids, USA) with a lipid to protein ratio (LPR) of 0.1 to 0.9 and dialyzed in a continuous flow dialyzing device (Jap et al., 1992) against a functionalization buffer using the following temperature profile: 25 °C for 12h, 40 °C for 24 h and a linear decrease to 25 °C over 6 h. The outcome of the reconstitution trials was examined in the transmission electron microscope (TEM): For negative stain analysis 3.5 μl of the reconstituted protein sample was adsorbed for 1 min

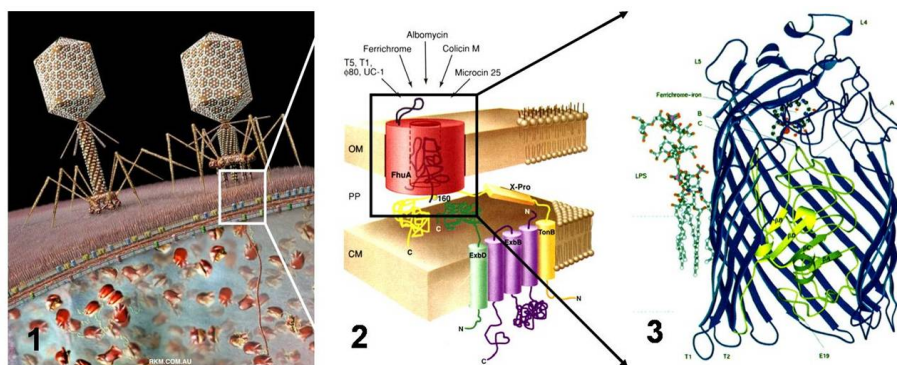


Fig. 7.1: (1) T5 phage virus binding to a cell membrane and injecting its DNA . (2) FhuA membrane protein in the outer membrane bilayer. (3) Structure of FhuA membrane protein.

onto glow discharged (20 s) carbon film-coated copper grids, washed three times for 3 s in distilled water (18 M Ω) and stained with 2 % uranyl acetate for 2×12 s. Images were recorded with a Hitachi H-8000 TEM at 200 kV and nominal magnification of 50,000 (calibrated magnification of 52,000) on Kodak SO-163 films. For further processing, the proteoliposomes were purified by sedimentation at 12000 rpm in a table centrifuge (Eppendorf Centrifuge 5415, Dr. Vaudois AG, Switzerland) for 20 min at 4 °C. This cleaning procedure was repeated twice. The buffer used for this cleaning process was adjusted to the subsequent experiments.

7.2.2 Functionality assay

Before using the proteoliposomes were used for binding experiments, the functionality was tested by phage binding assays: 3 μ g of FhuA protein reconstituted in proteoliposomes were resuspended in 10 μ l binding buffer containing 20 mM Tris HCl pH 8.0, 5 mM MgCl₂, 5 mM CaCl₂, 100 mM NaCl and 0.01 %NaN₃ and sedimented for 20 min at 12000 rpm in a table centrifuge at 4 °C. The proteoliposomes were resuspended in 15.5 μ l binding buffer, 0.5 μ g DNase I and 0.8×10^9 PFU (plaque forming units) of T5 phage prepared as described before and incubated for 2 h at room temperature. The proteoliposomes with the attached T5 phage were purified twice from unbound phage particles by sedimentation as described above. The binding assay was evaluated in the TEM by negative stain as described above.

7.2.3 Functionalization

Microfabricated arrays of eight silicon cantilevers of 500 μ m length, 100 μ m width, 1 μ m thickness and a spring constant of 0.03 N/m were used in all experiments (Micro- and Nanofabrication group, IBM Zurich Research Laboratory, Rüschlikon, Switzerland).

The cantilever arrays were cleaned in Piranha solution (2 parts concentrated H₂S O₄96% in 1 part H₂O₂31%) for 10 min. Subsequently the cantilevers were washed first in a 30 %NH₃ solution to remove charged particles and then twice in water (18 M Ω) for 5 min each. After cleaning in Piranha solution the cantilevers were coated on their upper side with 2 nm of Ti (99.99 %, JohnsonMatthey) followed by 20 nm of Au (99.999 %, Good-fellow) using an Edwards L400 e-beam evaporator operated at a base pressure below

10^{-6} mbar and evaporation rates of 0.07 nm/s. Subsequent a home-made crosslinker dithiobis-succinimidyl-undecanoate (DSU, molecular weight 629 g/mol; (Wagner et al., 1994, 1996)) was used to biofunctionalize the cantilever gold surface. To this end, the cantilever array was immersed in 1.5 ml of a 1 mg/ml DSU solution in water free Dioxan (Fluka, Switzerland) for 1 h at room temperature and subsequently cleaned in Ethanol from the Dioxan (2 quick washes by dipping in Ethanol, two times prolonged washes for 5 min. Afterwards the prefunctionalized cantilever array was dried under Argon.

FhuA proteoliposomes (nominal concentration after reconstitution: 1 mg/ml) were applied on the pre-functionalized cantilever interfaces by an ink-jet spotting MD-P-705-L dispensing system (Microdrop, Norderstedt, Germany) as described previously (Bietsch, Zhang, et al., 2004; T. Braun et al., 2006). A humidity chamber which allowed to stabilize the relative humidity at more than 95 % prevented the sample from drying. A schematic is shown in Fig. 7.2.

Ten droplets (estimated volume of 0.1 nl) were applied on every second cantilever using a nozzle with 70 μ m inner diameter at a spotting distance of 50 μ m resulting in complete wetting of the upper prefunctionalized cantilever surface. The cantilevers were incubated for at least 15 min at room temperature 22 °C. To prevent unspecific binding the complete cantilever array was immersed in a 1 mg/ml casein solution prepared the day before (usb corporation, USA) for 5 min at room temperature. To quench the remaining succinimidyl groups from the prefunctionalization step the cantilever was stored in binding buffer (see above) with Tris containing free amino groups.

7.2.4 Characterization of functionalization

To characterize the quality of functionalization, the cantilever were washed in H₂O and air-dried. Tapping mode AFM (Nanoscope, Multimode 3a) in ambient conditions was used to visualize the proteoliposome coverage across the cantilever. Such cantilever arrays were not used for subsequent measurements.

7.2.5 Binding assay

A schematic of the setup is shown in Fig. 7.3: The array with the functionalized cantilevers is directly mounted wet in the liquid chamber (5 μ l) without allowing them to dry. The piezoelectric actuator placed beneath the cantilever array chip body is excited periodically by a frequency generator. The cantilever response is read out using a beam-deflection technique: A beam of a vertical cavity surface-emitting laser (VCSEL; wavelength 760 nm, Avalon Photonics, Zurich, Switzerland) is reflected from the apex of the cantilever towards a position-sensitive detector (PSD; Sitek Partille, Sweden).

The response of the cantilever is continuously compared with the excitation wave using a network analyzer recording amplitude and phase spectrum (Hewlett Packard, 4589A, USA). Depending on the number of cantilevers used, a spectrum is recorded every 23 s (one cantilever) or at least every 3 min (serial measurement of all eight cantilevers). In both configurations, a sweep time of 1 s per spectrum was used. The cantilever array is mounted onto the piezoelectric actuator in such a way that only the cantilevers are within the analysis chamber, but not the chip body. The measurement chamber (volume \sim 5 μ l) is kept at constant temperature (accuracy \pm 0.02 K) during the experiment. A constant fluid flow rate in the cell was maintained using a pressure driven pump-system as described in (Grange et al., 2002; T. Braun, Barwich, et al., 2005).

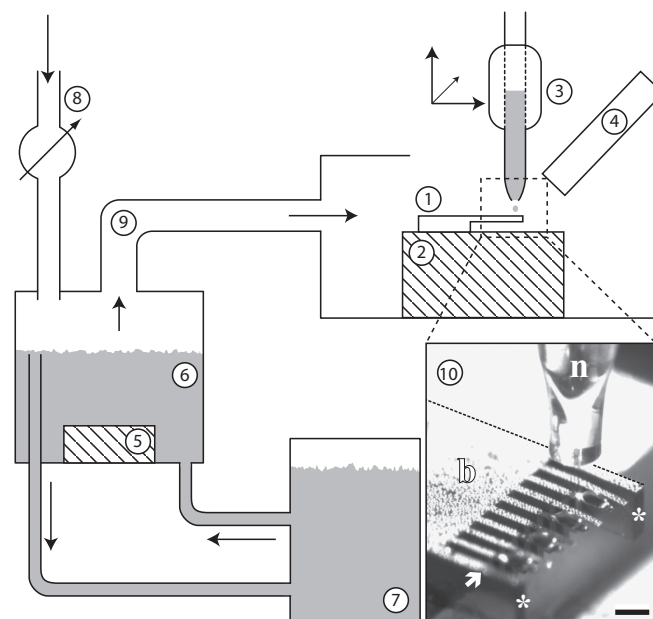


Fig. 7.2: Humidity chamber for functionalization of cantilevers with membrane-proteins. The cantilever array (1) is placed on a temperature controlled (peltier) cantilever holder (2). The ink-jet spotter nozzle (3) deposits droplets (10×0.1 nl) on the cantilevers and can be moved in all directions. The functionalization procedure can be controlled by a CCD camera through a magnifying optic (4). To prevent drying of the biological functionalization layer, small water droplets (18 M Ω) water were generated by a piezoelement driven membrane (5) placed in a small water bath (6). The water of the bath was continuously exchanged by a pump system from a cooled storage bath (7). The vapor generated above the humidifying bath was blown by a regulated air stream (8) through a connection tube (9) to the functionalization chamber with the cantilever array (1). The inset (10) shows a cantilever array after functionalization and the nozzle (n) through the camera (4). The start of the cantilever beam is marked by an arrow. The small water droplets on the base of the cantilever array (b) were generated by the humidity chamber. Every second cantilever was functionalized (large droplets). Note that only the upper interface is wetted by the spotter. The stars (*) mark the projection bars at the side from the cantilevers. The right handed periphery of the chip body is indicated by a dotted line. The scalebar corresponds to 500 μ m.

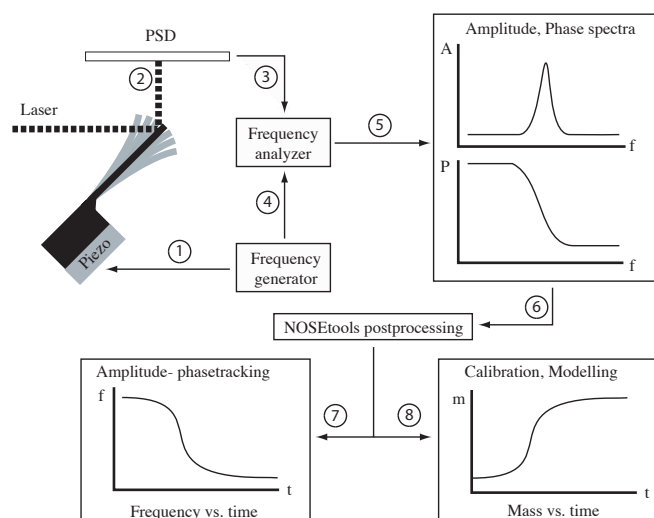


Fig. 7.3: Schematic of the cantilever based measurement setup. A frequency generator sweeps the spectrum by exciting a piezoelectric actuator located beneath the microcantilever array (1). The response of the cantilever is optically detected using a laser (2) and a position-sensitive detector (PSD). The frequency analyzer compares the cantilever response (3) with the excitation from the frequency generator (reference, 4) to determine the phase. The amplitude spectrum is recorded together with the corresponding phase values (5). The raw data was analyzed by postprocessing software called NOSEtools (6) in two ways: First, by tracking the resonance peak frequency or the turn-point frequency of the phase (7). Second by calibration for the co-moving mass and modeling, resulting in the absorbed mass (8).

Two kind of binding assays were performed: 1. Binding of T5 phages to the FhuA receptor, 2. Ferrichrome adsorption on the FhuA functionalized cantilever. All experiments were performed in binding buffer described above. The corresponding ligands were solved at specific concentrations (see results) in binding buffer. A typical binding experiment was performed at least in three sequences: A) Binding buffer (baseline 1) B) ligand injection(s) and C) again binding buffer (baseline 2). T5 phages were prepared as described before and ferrichrome was purchased from Sigma, Switzerland.

7.2.6 Data processing

All data-processing algorithms were implemented in the IGOR Pro data analysis environment in a package called NOSEtools (T. Braun, Ghatkesar, et al., 2007). Recorded time series of spectra were analyzed using two methods (postprocessing):

1. Amplitude peak-tracking and phase-turning point tracking (Ghatkesar et al., 2004) (Fig. 7.3 (8)): Here, the amplitude-peak maximum (resonance frequency) and the phase-turning point (eigenfrequency) were extracted and plotted versus time. Note that in this method all resonance peaks and phase turning points from individual cantilevers and higher order modes of individual cantilever respectively were analyzed separately. To minimize noise, the raw data was locally described with a gauss function (amplitude information) or a sigmoidal function (phase information). In all our evaluations here the smoothing functions and the raw data matched well.

2. Least-mean square fitting of the spectrum (FIG. 7.3 (8)). This method involved the fitting of the amplitude spectrum (including several resonance peaks) by the model and calibration method described in (T. Braun, Barwich, et al., 2005). This fitting method was used first for instrument calibration: During buffer injection at the beginning of the experiment, the virtual mass which co-moved with the cantilever sensor was determined and kept constant for the rest of the experiment.

7.3 Results and Discussion

7.3.1 Receptor preparation and protein functionality tests

The OG solubilized FhuA protein was reconstituted in *E. coli* by dialysis and examined in the electron microscope (Fig. 7.4 panel A). Depending of the lipid-to-protein ratio (LPR), small vesicles (LPR > 0.5) or large vesicles (LPR < 0.5, diameter > 200 nm) were observed. With an lipid to protein ratio (LPR) of ~ 0.1 sheets besides of vesicles were obtained. The addition of 5 mM MgCl₂ led to higher crystallinity of the reconstituted protein. Depending of the lipid to protein ratio and the reconstitution experiment, the vesicles revealed partial crystallinity (1 to 2 diffraction orders) or high crystallinity in the case of sheets in the power-spectra. For the binding experiment, samples with FhuA reconstituted in pure vesicles were used. Figure 7.4 panel B shows an control SDS-PAGE of reconstituted FhuA showing a strong band at ~ 70 kDa (corresponding to the nominal molecular weight of the membrane protein)

T5 phage were used as biological activity reporter for the FhuA membrane protein. These assays revealed a clear interaction of the virus to FhuA protein containing vesicles (Fig. 7.4 panel C and D) in solution. Only a few viruses were observed unbound in the background. Panel D shows the tight binding of the phage base-plate and the ample flexibility of the tail. Some phage obviously injected the DNA as indicated by an arrow in Panel D.

T5 binding to FhuA was also tested *in situ* on cantilever gold interfaces Fig. 7.4.

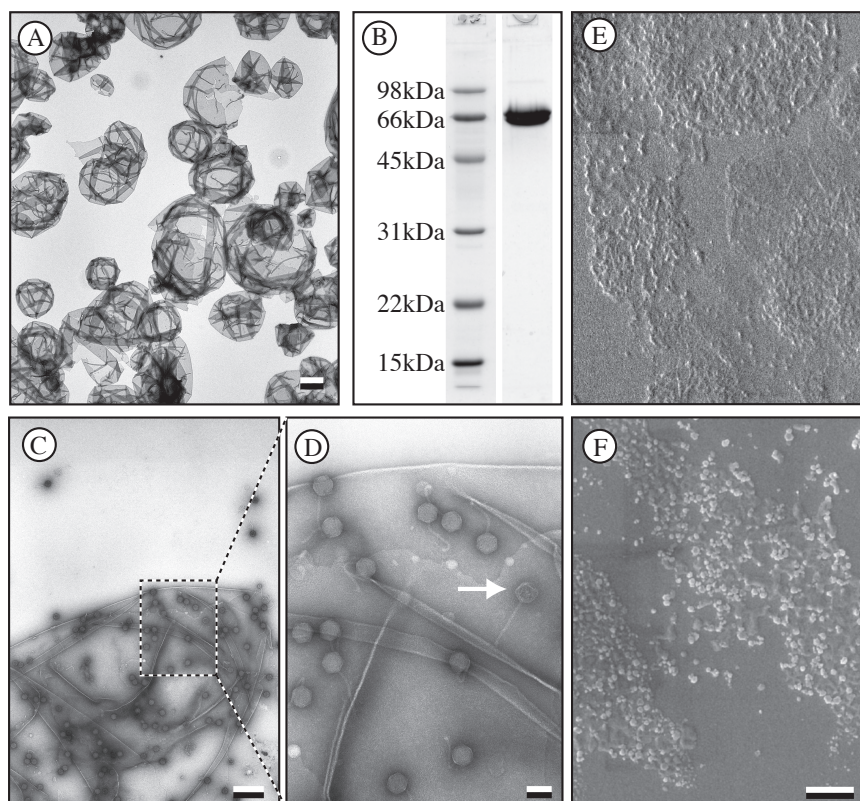


Fig. 7.4: Preparation of FhuA receptors for cantilever functionalization. Panel A: Vesicles of reconstituted FhuA. Panel B: Coomassie-blue SDS-PAGE of reconstituted FhuA protein. Panel C: Functionality assay for T5 phage binding to FhuA containing vesicles in solution. Scalebar: 500 nm. Panel D: Larger magnification of region indicated in panel C. Scalebar: 100 nm Panel E: Functionality assay for T5 phage binding to FhuA containing vesicles *in situ* on the gold interface. Panel F: Same as in panel E but with DSU crosslinker between the gold and the vesicles. Scale bar corresponds to 1 μm

To this end FhuA containing proteoliposomes were immobilized on one hand directly on gold (panel E) and on the other hand through the crosslinker DSU onto the gold interfaces (panel F). The results were visualized using scanning electron microscopy (SEM). These tests were performed at the resolution limit of the SEM. However, only with the DSU monolayer on the gold octahedral structure with the size of T5 heads were observed. On non-monolayer not pre-functionalized samples, vesicle like structures have been seen but no phage viral capsids (panel E). All subsequent immobilization experiments were performed with a DSU protection layer.

7.3.2 Functionalization of cantilevers

The functionalization of cantilevers was performed using an ink-jet spotter ((Bietsch, Hegner, et al., 2004)) for coating with ~ 1 nl proteoliposome containing buffer per cantilever sensor. To prevent drying out of the spotted droplets and subsequent denaturation of the membrane proteins, a humidity chamber was built around the cantilever arrays keeping the cantilevers surface wet for at least 30 min at a relative humidity of > 95 % (see Fig. 7.2). The set-up was temperature controlled at two different locations to prevent condensation of the humidity at the nozzle: First, the water bath with the mist generator (Fig. 7.2 7) and second, the cantilever holder itself (2). With the additional control of the airstream (Fig. 7.2 8) the humidity and temperature conditions in the functionalization chamber can be tightly controlled. Note that this set-up allows an excellent control of the wetting of the cantilevers and thus the upper surface of the cantilever can be selectively functionalized with incubation times of up to one hour.

To maintain the functionality of FhuA which is a mandatory prerequisite for native measurements (see section before), the cantilevers were pre-functionalized with the hetero bi-functional cross-linker DSU after gold coating (Fig. 7.5 panel A). Quality of cantilever functionalization with FhuA proteoliposomes was performed using tapping mode AFM. Figure 7.5 (panel B) shows a topography image recorded from a functionalized cantilever surface in the center of the cantilever bar. The image reveals typical shapes of FhuA proteoliposomes as observed by TEM (Fig. 7.4 panel A). The corresponding height profile indicated by the line in panel A exhibits height-steps of 5 nm (corresponding to the thickness of a bilayer containing membrane proteins). Comparing the profile with the image shows that the cantilever is covered with vesicles which only partially broke up. The inkjet spotter enabled a coverage of the cantilever interface of at least 64 %. However, the vesicle functionalization degree is from cantilever to cantilever complicating the comparison between measurements done with different arrays.

7.3.3 Binding experiments

To explore the potential of cantilever mass adsorption measurements in combination with membrane proteins, two ligands were tested: 1. For high molecular weight ligands, the adsorption of T5 phages was measured ($\sim 5 \times 10^{-17}$ g/virus, a rough estimate of the mass by adding molecular weights of the proteins). 2. For low molecular weights the adsorption of the ligand ferrichrome (687.7 Da).

Note that not only the positive functionalization of the cantilevers with native receptor molecules are needed, but also negative controls that are blocked for unspecific binding.

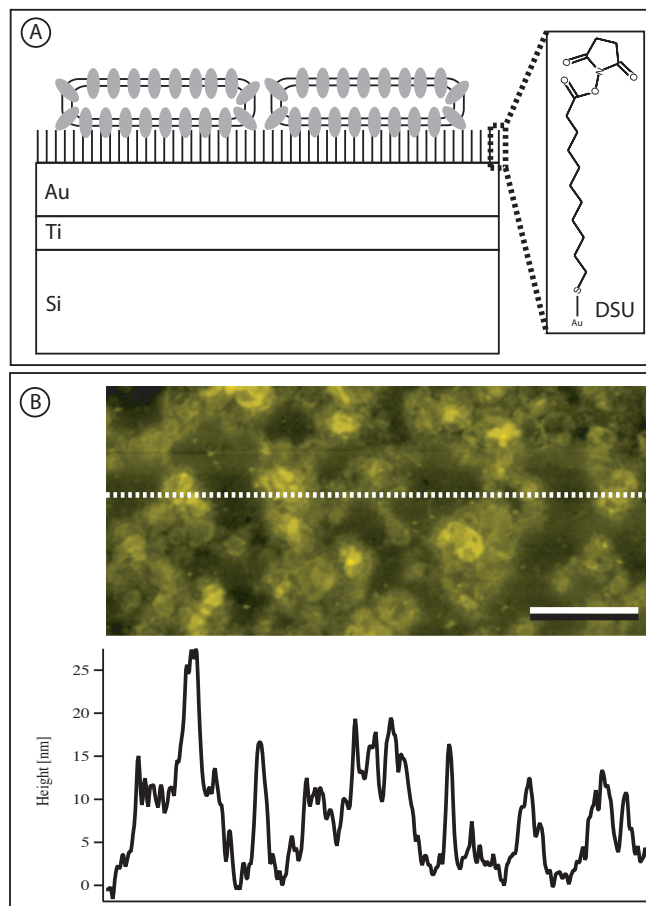


Fig. 7.5: Functionalization of cantilevers with FhuA proteoliposomes. Panel A: Schematic of cantilever functionalization. The gold interface of the cantilever was pre-functionalized with a self-assembling DSU cross-linker, which binds to the gold via a thiol group. It reacts by a succinimidyl reaction with primary amino or lysine groups of the FhuA protein reconstituted in the lipid-vesicles. The inset shows the chemical structure of the used DSU cross-linker. Panel B: Tapping mode AFM of the cantilever surface at the center of the cantilever bar. FhuA containing proteoliposomes are clearly visible similar to the one as seen in the TEM of Fig. 7.4 panel A. The line indicates the position of the recorded height-profile shown in the lower part of the panel. Scale bar is x micro meter

T5 phage binding experiments

Initially baseline was recorded in buffer for calibration of the co-moved liquid virtual mass ((T. Braun, Barwich, et al., 2005)), a solution containing 3 pM plaque forming units (PFU) of T5 phage was injected. An immediate change of the eigenfrequencies (data not shown) and therefore of the mass adsorbed to of the FhuA functionalized cantilever to lower values was recorded (Fig. 7.6). The qualitative development for frequency tracking and mass modeling is the same. A characteristic binding-curve with saturation behavior was observed. Neither the negative control nor the positive control after the final buffer injection revealed significant frequency changes. Please note that in a liquid environment the binding of a virus to the 1000 nm thick cantilever beam does not alter its spring constant as observed in other experiments under dry conditions (Tamayo et al., 2006; Ramos et al., 2006). Furthermore we observe a homogeneous phage binding to the whole cantilever interface. We measured and evaluated the resonance peak around 750 kHz which corresponds mode 15 for our cantilever design in aqueous solutions. The average of two positively functionalized cantilevers and one negative cantilever is shown. The error bars represent the estimated standard errors of the measurement. Other experiments performed in a similar way showed the same qualitative results. However, a direct comparison is difficult.

Note that under the measured conditions applied casein blocked efficiently unspecific virus adsorption. However, we experienced some adsorption also with negative controls using old casein stock solutions (older than one week, data not shown).

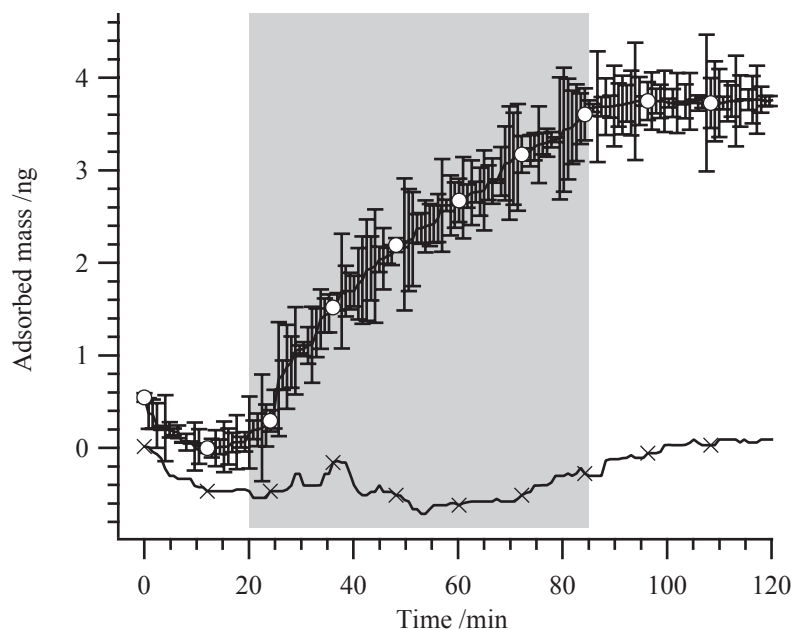


Fig. 7.6: Adsorption kinetics of T5 phage on FhuA functionalized cantilevers. FhuA the average of FhuA functionalized cantilevers is marked by white circles, the negative control with crosses. The error bars represent the estimated standard error of two cantilevers. Note that only every 15th data point is labeled by a marker.

FhuA was successfully purified and reconstituted in proteoliposomes. For immobilization functionality had to be preserved. We used bacteriophage T5 as a reporter for the native embedding in lipids and subsequent covalent immobilization on the sensor interface. The results have shown that the crosslinker DSU indeed is not only useful for immobilization but also is helpful as protection layer between the protein and the gold interface. Note that these finding must be related by the observation that the measurements with immobilized proteoliposomes with low crystallinity led to better adsorption results than the usage of highly crystalline sheets (data not shown). Functionalization with proteoliposome vesicles provides an additional inherent protection layer explaining this finding. Current models of phage adsorption propose that during phage binding a transmembrane protein is inserted at the side of the FhuA protein.

Ferrichrome adsorption

After recording the baseline in binding buffer, apo-ferrichrome at two different concentrations (1 nM and 1 μ M) were subsequently injected. At the end, the measurement chamber was flushed again with binding buffer.

The results are shown in Fig. 7.7. The negative control (casein blocked) shows no significant changes throughout the experiment.

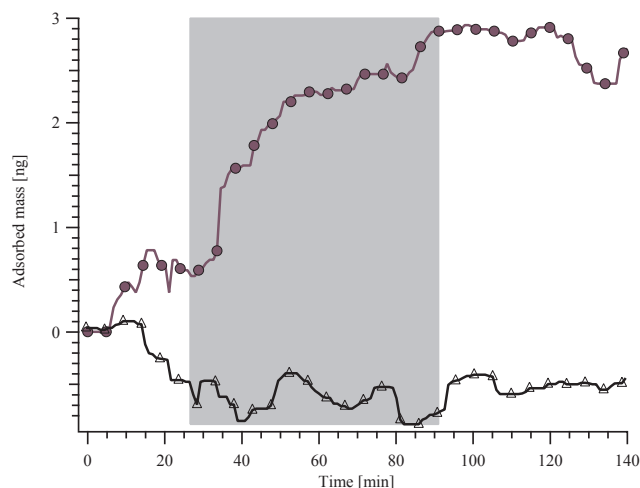


Fig. 7.7: Ferrichrome binding to FhuA functionalized cantilever (filled circles) and casein blocked cantilevers (triangles).

Also the positive control (FhuA functionalized cantilevers) did not respond significantly after injection of a 1 nM ferrichrome solution. Nonetheless, after injection of a 1 μ M ferrichrome solution, a clear change towards lower frequencies was observed. Neither the positive nor the negative control exhibited significant changes of the frequency after injection of buffer, resulting in a straight baseline.

7.4 Conclusion

We demonstrate the functionalization of cantilever gold-surfaces with the native trans-membrane protein FhuA by a binding assay with T5-phage reporters and SEM microscopy. Binding assays of natural ligands to FhuA sensitized cantilevers show that microcantilever sensors can measure small ligands (Ferrichrome, 700Da) and large ultrastructures (T5-phage, $1.5 \cdot 10^{-17}$ g) label-free and in real-time. We envision the reconstitution, immobilization and characterization by nanomechanical cantilevers as a general method for the measurement of membrane-protein ligand interactions.

CHAPTER 8

DETECTION OF MULTISTEP PROCESS IN BIOSYSTEMS: COMBINED STATIC AND DYNAMIC MODE

"Anyone who has never made a mistake has never tried anything new." – Albert Einstein

When a ligand binds to a receptor two physical properties change: The mass increases and the structure of the receptor changes to transduce the signal of the ligand. We developed a nanomechanical sensor for biological and medical research which not only monitors the binding event of effector molecules to their target but also the subsequent action and effect on a biological system *in vitro*. This label-free method follows mass and surface stress on the sensor interface simultaneously and is based on cantilever technology. The mass is measured by tracking the resonance frequency of the cantilever (dynamic mode). Structural changes are detected by the static bending of asymmetrical functionalized cantilevers. To prove the concept we measured lipid vesicle ($\sim 748 \times 10^6$ Da) adsorption on the sensor interface followed by subsequent binding of the bee venom peptide melittin (2850 Da) to the adsorbed vesicles. Our results show a) that microcantilevers can measure very heavy ultrastructures as well as small peptides successively and b) combined detection of mass adsorption and structural changes provides comprehensive information about the binding event which cannot be detected by other techniques. We foresee that this microarray method can be used to analyze other (bio-)systems in general such as receptor ligand or enzyme antagonist interactions.

8.1 Introduction

Molecular interaction and recognition are the key principles in biology and are found in every aspect of life. Examples are enzyme-substrate interaction for chemical reactions, Protein-DNA binding for gene activation or ligand docking to receptors for signal transduction. These interactions take place in two steps: First, the two partners bind to each other via molecular recognition and, second, structural changes of the complex

involve further actions such as chemical reactions, gene expression or activation of further downstream components of a signal transduction cascades.

It is not surprising that an arsenal of techniques were developed for biological, medical and chemical research to detect and characterize interactions between molecular partners. This includes *in vivo* techniques such as the two hybrid system (Fields & Song, 1989) which reveals potential interacting partners during a cloning process. However, for more precise analysis *in vitro* systems are used. This involves techniques depending on labels, such as the Enzyme-Linked ImmunoSorbent Assay (ELISA)(Engvall & Perlman, 1971) for rapid detection of known markers or spectroscopic assays for time-resolved measurements (Van Holde et al., 2006). Most of these techniques depend on labels which must be introduced prior to the experiments and can change the behavior of the partners. Label free techniques are therefore an important alternative for real-time experimentation. Such techniques include surface plasmon resonance (Jordan & Corn, 1997), ellipsometry (Wang & Jin, 2003), surface acoustic wave sensors (Gronewold et al., 2006) and quartz micro balance (QCM) (Marx, 2003) systems. These systems depend on the immobilization of one of the partners on the transducer interface. All the techniques referred above merely detect an interaction of two molecular partners but fail to provide information about effects and biological implications. Therefore we developed a cantilever based sensor (Lang et al., 2006) which can measure two signals simultaneously: First, the change in resonance frequency of the cantilever which is directly related to the adsorbed mass (dynamic mode) (T. Braun, Barwich, et al., 2005). Second, induced deflection of the cantilever due to structural changes (static mode) (T. Braun et al., 2006; Y. Zhang et al., 2004). The static mode bending of the cantilever occurs owing to the difference in surface stress between the upper and lower cantilever surface, as it can be transduced by structural changes of receptor molecules on one of the cantilever interfaces. We postulate that the concurrent measurement of these two modes allow a comprehensive interpretation of binding events and their biological effects.

We used the well characterized Melittin(Raghuraman & Chattopadhyay, 2006) as model system, a small peptide of 26 amino acids (2.8 kDa) from honey bee (*apis mellifera*). It was first described as hemolytic peptide and is responsible for the toxicity of the bee venom. Its action is developed in four steps: (a) The amphiphilic peptide adsorbs on the lipid-liquid interface (b) before it takes an α -helical conformation, inserts into the lipid bilayer (c) and forms channels by oligomerization of the helices in the lipid bilayer responsible for the observed hemolysis (d) followed by cell lysis.

Here we report the successful measurement of mass and surface stress changes induced first by vesicle adsorption followed by the binding and insertion of melittin into the lipid-phase of the vesicles and the subsequent formation of channels.

8.2 Materials and Methods

Materials

Lipids Dioleoylphosphatidylcholine (DOPC) was purchased from Avanti Polar Lipids (Alabama, USA). Melittin, Nanopure water, 11-Amino 1-undecane thiol (AUT) and 99.99 % Ethanol from Sigma-Aldrich (Buchs, Switzerland). Silicon cantilever arrays containing 8 cantilevers, each 500 μm long, 100 μm wide and 1 μm thick with spring constant 0.03N/m were microfabricated at Micro and Nanomechanics group, IBM Zurich research laboratory in Rüschlikon, Switzerland. Gold depositions were done in Balzers MED 010 thermal evaporator operated at a base pressure below 10^{-5} mbar and evaporation rates of 0.16 nm/s. A home made extruder (Department of Chemistry,

University of Basel) with 25 mm diameter polycarbonate membrane filters track-etched with pores of diameter 100 nm from Whatman Nucleopore, Middlesex, England was used to prepare vesicles. Dynamic light scattering technique was used to measure vesicle size. A buffer solution of 50 mM Tris and 100 mM NaCl at pH 7.6 was used for both vesicles and melittin. As a negative control, milk protein Casein (23 kDa) was used. It was dissolved in the above mentioned buffer and used in the concentration of 1 mg/ml. It takes about 90 min on a shaker to dissolve casein. Mild heating of the solution at about 40 °C will increase its dissolving speed. Powder AUT stored at -40 °C is brought to room temperature before using. Owing to its long chain length it dissolves better in organic solvents like ethanol. A solution of 1 μ M in concentration was prepared in ethanol.

Vesicle preparation

Chloroform dissolved DOPC lipids were dried under Argon. They were kept under vacuum overnight to remove any traces of chloroform. The dried lipid films were hydrated with buffer at a concentration of 10 mg/ml. DOPC has a gel-liquid crystal transition temperature (T_c or T_m) of -20°C. The solution was thoroughly vortexed until it turned milky white. The resulting large multi-lamellar vesicles (LMV) were subjected to 6 freeze thaw cycles in liquid nitrogen and warm water. The solution was diluted to 2 mg/ml and squeezed through 100 nm filter using an extruder. After 12 cycles of extrusion the initial milky white vesicle solution turned into dense clear liquid indicating that the LMVs have become large unilamellar vesicles (LUV). Vesicles were stored at 4 °C and were found stable for about 60 days.

Melittin preparation

Stock solution of Melittin (molecular weight of 2846.5 Dalton) was prepared in the concentration of 88 μ M. A peak at 280 nm wavelength in UV absorption spectroscopy with an absorption coefficient of 5570M⁻¹cm⁻¹ was obtained (Rex & Schwarz, 1998). Protein was stored at -20° C and further diluted to different concentrations were made before the experiment.

Functionalization

Before functionalizing the cantilevers, following cleaning procedure was followed to remove any unwanted organic layer formed on the cantilever surface. Step 1: The cantilever arrays were cleaned in piranha solution (1:1 ratio of concentrated H₂SO₄ 96% and H₂O₂ 31%) for 20min. Step 2: Washing in nanopure water. Repeated steps 1 and 2 for another 20min. Step 3: To remove the residues of H₂SO₄, samples were cleaned in 1:1:1 of NH₃ 30%, H₂O₂ 31% and nanopure water for 10min. Again the samples were thoroughly washed in nanopure water. Step 4: Cleaning in isopropyl alcohol for 5min and drying in air. Gold layer of 17 nm with a Titanium adhesion layer of 2 nm was deposited on top side of the cantilever. Immediately after that, they were incubated in microcapillaries. Four of the cantilevers were incubated in 1 mM AUT dissolved in ethanol for 60 min. Later the entire array was thoroughly washed in ethanol and dried. Subsequently, to block the other four cantilevers without SAM layer of AUT, entire cantilever array was incubated in 1 mg/ml casein for 30 min.

Setup

see chapter 3

Experiment

The functionalized cantilever array was carefully mounted in the liquid chamber without allowing it to dry. Cantilevers were equilibrated in a constant flow of buffer at 11 $\mu\text{l}/\text{min}$ for about one hour in a temperature controlled box. After constant base line of resonance frequency was reached, vesicles were injected. Later, the entire chamber was again thoroughly washed by injecting buffer to remove any unspecifically bound vesicles. Subsequently, melittin was injected followed by buffer. Each injection step was done at intervals of 45 min maintaining a constant flow rate during the entire experiment. NOSE Tools software written in IGOR PRO was used to analyze the data.

8.3 Results

To measure in static mode (surface stress induced by structural changes), the cantilevers must be sensitized in an asymmetrical way, i.e. at one interface only. Furthermore, unspecific binding of melittin to the cantilever must be blocked. For this, the upper cantilever interface was first covered with a 20 nm gold layer followed by a SAM formation of 11-aminoundecanethiol (AUT). Voltametric studies indicate that thiol group on AUT is deprotonated upon adsorption (Wink et al., 1997). The assumed gold-thiolated bond is $\text{RSH} + \text{Au} \longleftrightarrow \text{RS}^-\text{Au} + \text{e}^- + \text{H}^+$. With NH_3^+ termination on the other end of the SAM a net-positive charge on this interface is expected. This pre-functionalization procedure was important for all subsequent experiments in two ways: First, it prevents the unspecific binding of melittin peptide which has a net positive charge. Second, the DOPC vesicles bind stronger and faster to AUT functionalized cantilevers as compared to bare silicon interfaces, as shown in vesicle binding experiments (Fig. 8.1 panel A). These experiments were done during initial surface optimization process with 130 nm vesicles in a solution of 10 mM HEPES buffer and 150 mM NaCl. Casein blocked cantilevers did not show any significant mass adsorption after lipid vesicle injection. In comparison AUT pre-functionalized cantilevers show a mass uptake of 3 ng when only the upper cantilever interface was pre-functionalized, but 8 ng vesicles adsorbed when both surfaces were pre-functionalized with a positively charged thioalkane. We conclude that the vesicles bind preferentially to AUT functionalized cantilevers. Most probably by electrostatic interactions. Figure 8.1A also show the slow kinetic of vesicles absorbing to bare silicon in the absence of casein. Furthermore, unspecific binding of vesicles to bare silicon interfaces can be blocked by prior incubation of the cantilever array in a casein solution. In most the experiments the initially injected vesicles seem to bind irreversibly to the cantilevers since no mass decrease was observed after buffer injection without vesicles. However, with very high lipid concentrations or subsequent injection of additional vesicles a washing-off was observed. Obviously vesicles form multilayers with a weak affinity between layers. These additional vesicles are removed in subsequent buffer washing steps.

The mass adsorption to single sided AUT functionalized cantilevers during injections of different solutions with varying vesicle concentrations are presented in Fig. 8.1 panel B. These experiments were done in Tris buffer and 100 nm vesicles as mentioned in methods section. All curves show a saturation behavior but at different final absolute adsorbed mass. Plotting the final mass uptake against the concentration (Fig. 8.1 C)

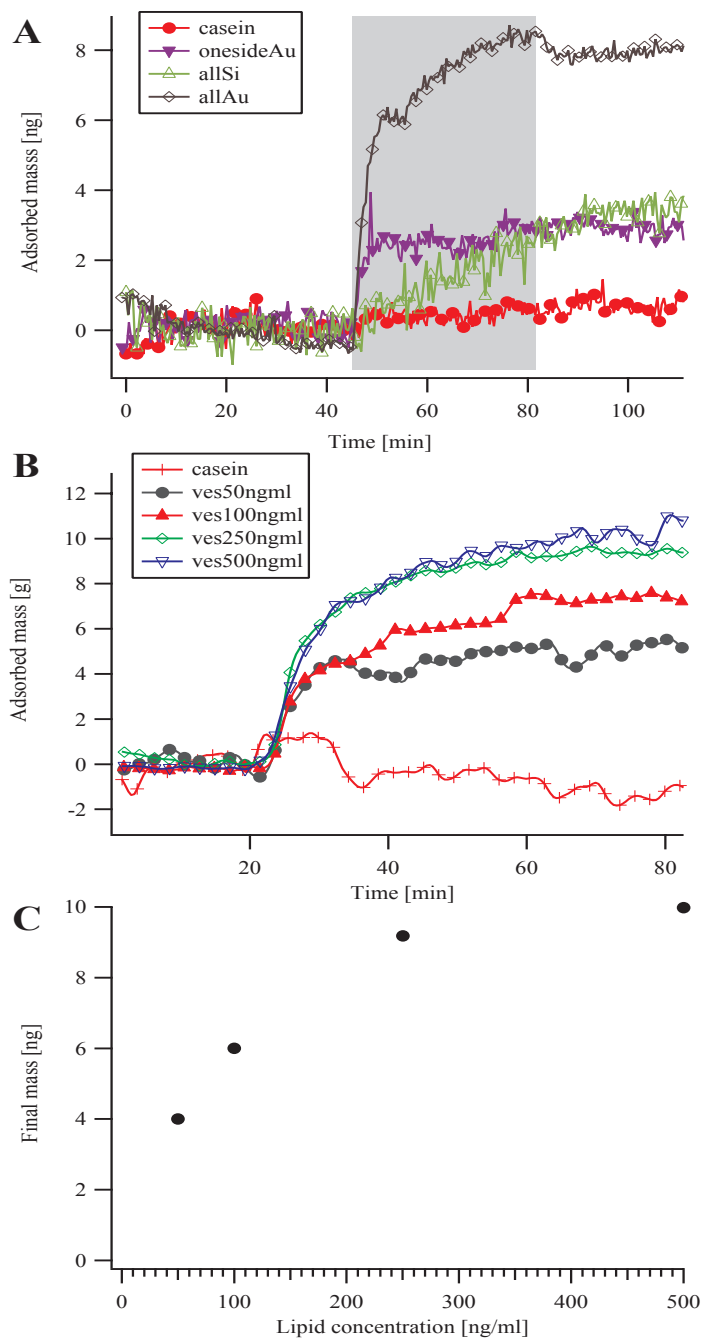


Fig. 8.1: Pre-functionalization of cantilevers and vesicle adsorption. (A) Vesicle adsorption of a 100 ng/ml lipid solution to distinct functionalized cantilever arrays. (B) Injection of differently concentrated vesicles to single sided functionalized cantilever arrays. (C) End-concentrations of the adsorption curves of panel B.

revealed a saturation reached with concentration of 250 ng/ml. Taken the results together we conclude that we have only one layer of vesicles which are able to adsorb on the AUT layer. This is important for the following melittin binding experiment.

Figure 8.2 depicts the mass adsorption and the surface stress development for vesicles (500 ng/ml) and subsequent melittin injection (1 μ M). The average of two cantilevers is shown. Note that the signals of the negative control does not exhibit any significant changes during the experiment (data not shown). After recording a buffer baseline (Fig. 8.1 section I), vesicles were injected with a concentration of 500 ng/ml leading to saturation of cantilever surface with vesicles. The surface stress difference between the AUT functionalized side and the silicon backside of the cantilever leads to a upward bending of the cantilever by 143 nm in average (section II). Note that we show the differential signal between AUT functionalized and blocked reference cantilevers, as discussed previously (T. Braun et al., 2006). After vesicle injection buffer was flown through again (section III) before melittin was injected (section IV) and washed finally (section V). As with the vesicle injection, the mass in section IV increased for \sim 1 ng, whereas the bending of the cantilever decreased by 25 nm, representing a small, but significant deflection change. Note that the relative change for the static mode signal is much clearer than seen in dynamic mode signal.

8.4 Discussion

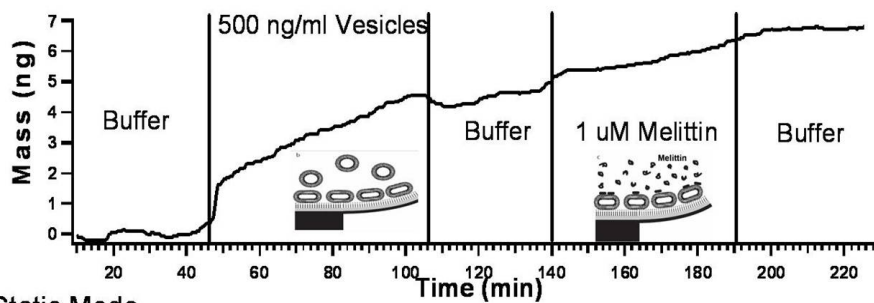
Our results show that (a) we can measure ligands of wide range of masses and, (b) mass adsorption and structural changes on the cantilever interface have been measured simultaneously (Fig. 8.2).

One sided cantilever functionalization is essential to measure a surface stress with cantilevers. Our data show that the vesicles mostly adsorbed on the AUT functionalized side of the cantilevers and have only a weak affinity to silicon oxide (Fig. 8.1 A). Double sided AUT functionalized cantilevers adsorbed more than the double amount of vesicles. This is most probably due to electrostatic interactions as reported before

Vesicle adsorption experiments lead to different saturation masses adsorbed to the cantilever (Fig. 8.1 B). Since the vesicle adsorption is not reversible this hints strongly to a two step adsorption process: After initial contact of the vesicle with the AUT interface, structural changes takes place flattening the vesicle on the cantilever interface. During this process, the vesicle expands on the cantilever interface which is limited by two factors: First, the vesicle can only expand/flatten to certain limit before breaking up (which can also take place) and second by the free space on the cantilever interface before being limited by a neighboring adsorbed vesicle. Therefore the final adsorbed mass is higher for experiments with high vesicle concentrations since the vesicles have less time to flatten on the surface before being limited by a neighbor. Note that the higher adsorbed mass is not due to the growth of multiple vesicle layer on the cantilever surface which is demonstrated in Fig. 8.1 C. The flattening of the vesicles is also visible by the cantilever deflection (Fig. 8.2, section II) where the cantilever is bend up by the interaction with the cantilever vesicles (Newton's law of reciprocal actions).

Literature indicate that vesicle adsorption and bilayer formation are highly dependent of the chemical and physical nature of the surface, the lipid and the used buffer (Benes et al., 2004; Cha et al., 2006). We measured a mass per area of 4 μ g/cm² with the highest concentrations of vesicle solutions (500 ng/ml). Comparing with literature (Benes et al., 2004), mass per areas higher than 1 μ g/cm² are generally regarded as vesicle-like structures adsorbed on the surface. Bilayer formation is reported with a mass per area of around 0.5 μ g/cm². Hence we conclude that large part of the adsorbed lipid is in forms

Dynamic Mode



Static Mode

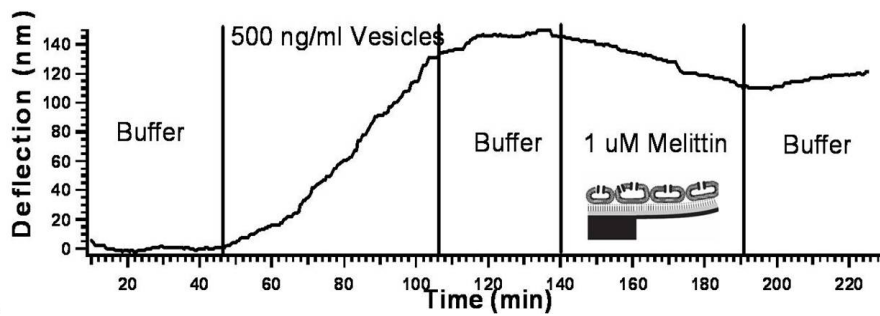


Fig. 8.2: Combined static and dynamic experiment measuring the lipid adsorption and subsequently the binding of melittin to the adsorbed vesicles. The upper graph displays the mass adsorption, while the lower graph the surface stress development measured simultaneously. The experiment was performed in five sections: (I) Baseline recording in buffer. (II) Injection of 500 ng/ml DOPC vesicles. (III) Buffer injection. (IV) Melittin injection ($1 \mu\text{M}$). (V) Final buffer injection. Note that the upper cantilever interface were pre-functionalized with AUT prior to the experiment.

of vesicles, but the exact structure of the lipid on the cantilever can not be determined. One reason that our vesicles do not break up in the same extent as reported could be the flexible support of the cantilever which itself bends up by the interaction force of the vesicles and cantilever surface charge. However, the exact state of the adsorbed vesicles is not of importance for a qualitative discussion.

The combined signal of the melittin experiment show the upward flexing of the cantilevers during vesicle adsorption as discussed above. After the injection of the melittin the cantilever bends down - first slowly and with increased mass concentration faster. This indicates a delayed respond of the cantilever compared to the mass adsorption which is in good agreement with current models for melittin adsorption to lipid vesicles and their insertion. Our data suggest, that this delay is related to the insertion into the lipid bilayer and the subsequent formation of the channels. This channel formation explains the downwards bending of the cantilever. This interpretation is depicted as pictures in Fig. 8.2, section II and IV. In section II, adsorption of vesicles on the cantilever surface bends the cantilever upwards driven by the interaction energy between the cantilever surface and the vesicles which are flattened by this interaction. In section IV, after injection of the melittin these small peptides first bind to the vesicle surface (top picture), form α -helices, insert into the membrane and form channels by oligomerization (bottom picture). Interestingly, the mass increase during the melittin flow happens 30 min after injection while the bending of the cantilever starts already after 20 min. This can be explained by the fact that melittin being a small molecule (2.8 kDa). Sufficient accumulation of the molecules on the vesicles is required before there is a detectable mass change on the cantilever, whereas the channel formation in the vesicle walls is so quick and strong that the bending is seen before an appreciable mass change occurs. Note that the melittin concentration in the cantilever surrounding buffer remains constant during injection, since we are pumping a constant melittin concentration of 1 μ M through the measurement chamber.

8.5 Conclusions

We developed a biosensor to measure not only the binding but also the effect of ligand molecules on their biological target *in vitro*. This sensor is cantilever based and measures simultaneously the mass adsorption (dynamic mode) and structural changes (static mode). We tested the sensor by measuring the adsorption of lipid vesicles (high mass) and small peptide (melittin, low mass). The obtained mass and surface stress curves reflect the adsorption of vesicle to the pre-functionalized cantilever surface, the binding of melittin to lipid and the insertion and the oligomerization of the melittin peptide in the lipid phase. The results are in good agreement of current models gained by various techniques. We strongly believe that the combined measurement as proposed here will establish as a general tool to characterize molecular interactions.

CHAPTER 9

CONCLUSIONS AND OUTLOOK

"Try not to become a person of success but a person of value." – Albert Einstein

The use of microcantilevers as sensitive label free detectors has been repeatedly proved. Various chemical and biological processes were detected via surface stress monitoring by static bending of the microcantilever independent of fluorescent or radioactive labeling of molecules. The bending is mainly due to steric or charge effects among an ensemble of molecules on the cantilever surface giving a resultant qualitative effect of the molecules. However, quantitative information can be obtained via mass change monitored by frequency shift in the resonance frequency of the microcantilever. But, owing to heavy damping in liquid and associated low quality factors it has always been a challenge to resonate cantilevers in liquid. This thesis describes the successful attempt in vibrating microcantilever sensors in liquid at various resonant modes and using them to do quantitative measurements for biological applications.

Major Contributions

Instrument

- A setup capable of simultaneously measuring surface stress (static mode) and mass change in liquid has been built. Efficient energy transfer between piezo and the microcantilevers was achieved. The fluid cell with chamber volume of 6 μl can hold a chip with an array of eight cantilevers. It uses an air pressure system for smooth flow of liquids. The entire system is temperature controlled with a stability of 0.01 K. It is suitable to quantify certain real-time multi-step biological and chemical processes.

Physics

- Prior to operating the cantilevers in liquid it has been proved that mass sensitivity of resonating cantilevers increases as a second order function of mode number in ambient conditions. From uniformly deposited gold layers, a sensitivity increase of 940 $\text{ag/Hz}/\mu\text{m}^2$ at mode 1 to 8.6 $\text{ag/Hz}/\mu\text{m}^2$ at mode 7 indicates an increase of at least two orders of magnitude by resonating cantilevers at higher modes.

The mass sensitivity starts to decrease for a distributed mass load of above 2 % of cantilever thickness with its spring constant starting to get changed significantly.

- Clear well resolved resonance peaks for 16 flexural modes of vibration in liquid were obtained in 1 MHz frequency range. Increase in quality factor with mode number (1 at mode 1 and 30 at mode 16) clearly indicated a sensitivity increase at higher modes. Frequencies beyond mode 9 matched very well with estimated frequencies by the Elmer-Dreier model and the extended viscous model by Sader. Our experimental results have proved that 2D and 3D models converge at higher modes keeping the effect of viscosity constant. The added apparent mass due to liquid on a cantilever of mass 93 ng becomes asymptotically smaller at higher modes, it displaces almost 40 times of its mass at fundamental and about 10 times at mode 16.
- The independent effects of density and viscosity on the resonating cantilevers have been studied. Microcantilevers were able to clearly distinguish between these two changes. They could measure a density change of 0.06 % and a viscosity change of 3 % in water. Furthermore, owing to a heavily damped system with low quality factor, the difference between peak frequency from amplitude curve and eigen frequency from phase curve was clearly distinguished.
- Binding of biotin latex beads (each 250 nm in diameter, 1 fg) to a streptavidin functionalized cantilever was performed as a model experiment to measure mass in liquids. An mass adsorption of 7 ng was measured on the cantilever with a mass resolution of 1 ng. A clear frequency increase with mode number for the same amount of mass adsorption on the cantilever was observed indicating that mass sensitivity increases with mode number.

Biology

- As a next stage we did a real time biological experiment. 2D crystals of reconstituted FhuA transmembrane proteins were immobilized on the cantilever by nanolitre volumes using the ink jet spotting technique. The gold interface of the cantilever was pre-functionalized with a self-assembling DSU cross-linker, which binds to the gold via a thiol group. It reacts through a succinimidyl reaction with primary amino or lysine groups of the FhuA protein reconstituted in the lipid-vesicles. FhuA containing proteoliposomes were confirmed using tapping mode AFM on the cantilever surface. FhuA functionalized cantilevers were found to sensitive to detect their ligands T5 phage virus (10^{-17} g) and ferrichrome (700 Da).
- Finally we combined static and dynamic mode measurements by separating AC and DC signals from the position sensitive detector. This enabled us to detect both stress change and mass change on a cantilever. After initially confirming our setup with a simple heat test we investigated a two stage biological system along with confirming simultaneous stress and mass measurement. Initially adsorption by an assay of lipid vesicle ultra structures on a positively charged cantilever surface revealed that they form only a monolayer of vesicles with maximum mass of 8 ng resulting in the cantilever bending upwards. This monolayer of vesicles constitutes a platform for adsorption of melittin (a 2.8 kDa bee venom protein) to bind to vesicles and open channels in the lipid membrane of vesicles. Melittin

binding has resulted in mass increase and its pore forming ability created stress on the cantilever producing downward bending.

In conclusion, a microcantilever sensing system in liquid has been developed, which can perform simultaneous measurement of mass adsorption and surface stress on the cantilever at a resolution of 1 ng and 10 nm deflection towards biological applications.

Outlook

- The existing array of eight cantilevers can be extended to thousands of cantilevers for simultaneous measurement of many different analytes thus forming a large scale multifunctional cantilever array sensor (Lutwyche et al., 2000).
- A self sensing mechanism like piezoelectric or piezoresistive embedded in the cantilever itself will make them able to detect even opaque liquid samples and makes them portable avoiding the optical detection technique.
- Shrinking the cantilever dimensions will result in sensitivity increase. Already zepto gram (10^{-21} g) has been achieved in vacuum (Yang et al., 2006).
- Extending the simultaneous mass and stress sensing to even voltage sensing will provide detection of complete functionality across the cell membrane.
- Portability and cost of the system can be reduced to a large extent by shrinking the entire fluid flow system and the microcantilever on to a single chip. Combining with other sensors in a single chip, microcantilevers represent ideal components for lab on a chip applications.
- Cantilevers might be applied as portable diagnostic tool in personalized medicine.
- The ultimate grand challenge is to measure the mass of single molecules in real time and simultaneously detect different types of molecules. Furthermore, if device microfabrication can reach the ultimate sensitivity of mass detection, a portable non-destructive mass spectrometer in liquid can be envisaged.

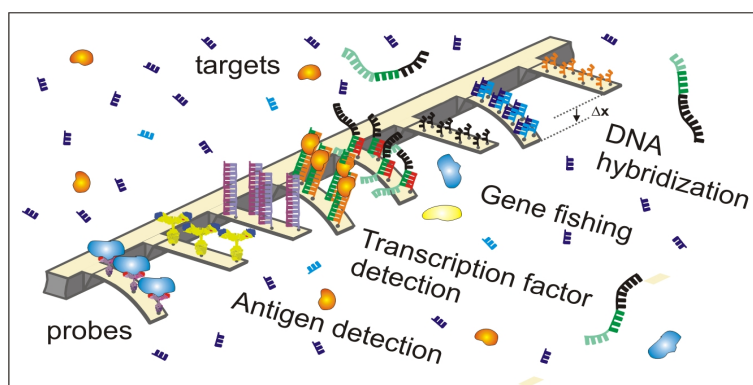


Fig. 9.1: Cantilever array simultaneously detecting multiple ligands

REFERENCES

- Alberts, B., Johnson, A., Lewis, J., Raff, M., Roberts, K., & Walter, P. (2002). *The molecular biology of the cell* (K. Jenner, Ed.). Garland Science.
- Arntz, Y., Seelig, J. D., Lang, H. P., Zhang, J., Hunziker, P., Ramseyer, J. P., et al. (2003). Label-free protein assay based on a nanomechanical cantilever array. *Nanotechnology*, *14*, 86-90.
- Backmann, N., Zahnd, C., Huber, F., Bietsch, A., Plückthun, A., Lang, H. P., et al. (2005, October 11). A label-free immunosensor array using single-chain antibody fragments. *PNAS*, *102*(41), 14587-14592.
- Baller, M. K., Lang, H. P., Fritz, J., Gerber, C., Gimzewski, J. K., Drechsler, U., et al. (2000). A cantilever array-based artificial nose. *Ultramicroscopy*, *82*, 1-9.
- Basak, S., Raman, A., & Garimella, S. V. (2006). Hydrodynamic loading of microcantilevers vibrating in viscous fluids. *J. Appl. Phys.*, *99*, 114906.
- Baskurt, O. K. (2003). Pathophysiological significance of blood rheology. *Turk. J. Med. Sci.*, *33*, 347-355.
- Battiston, F. M., Ramseyer, J. P., Lang, H. P., Baller, M., Gerber, C., Gimzewski, J. K., et al. (2001). A chemical sensor based on a microfabricated cantilever array with simultaneous resonance-frequency and binding readout. *Sensors and Actuators B*, *77*, 122-131.
- Benes, M., Billy, D., Benda, A., Speijer, H., Hof, M., & Hermens, W. T. (2004). Surface-dependent transitions during self-assembly of phospholipid membranes on mica, silica, and glass. *Langmuir*, *20*(23), 10129-37.
- Bergauda, C., & Nicu, L. (2000). Viscosity measurements based on experimental investigations of composite cantilever beam eigenfrequencies in viscous media. *Rev. Sci. Instrum.*, *71*, 2487-2491.
- Berger, R., Delamar, E., Lang, H. P., Gerber, C., Gimzewski, J. K., Meyer, E., et al. (1997, June). Surface stress in the self-assembly of alkanethiols on gold. *Science*, *276*, 2021-2024.
- Berger, R., Gerber, C., Gimzewski, J. K., Meyer, E., & Güntherodt, H.-J. (1996, July). Cantilever sensor for nanomechanical detection of specific protein conformations. *Appl. Phys. Lett.*, *69*(1), 2385-2388.
- Berger, R., Lang, H. P., Gerber, C., Gimzewski, J., Fabian, J., Scandella, L., et al. (1998). Micromechanical thermogravimetry. *Chemical Physics Letters*, *294*, 363.

- Bietsch, A., Hegner, M., Lang, H. P., & Gerber, C. (2004, June). Inkjet deposition of alkanethiolate monolayers and DNA oligonucleotides on gold: Evaluation of spot uniformity by wet etching. *Langmuir*, *12*(20), 5119-5122.
- Bietsch, A., Zhang, J., Hegner, M., Lang, H. P., & Gerber, C. (2004). Rapid functionalization of cantilever array sensors by inkjet printing. *Nanotechnology*, *15*, 873-880.
- Binnig, G., Quate, C. F., & Gerber, C. (1986). Atomic force microscope. *Phys. Rev. Lett.*, *56*, 930.
- Binnig, G., Rohrer, H., Gerber, C., & Weibel, E. (1982, January). Tunneling through a controllable vacuum gap. *App. Phys. Lett.*, *40*(2), 178-180.
- Binnig, G., Rohrer, H., Gerber, C., & Weibel, E. (1983, January). 7x7 reconstruction on si(111) resolved in real space. *App. Phys. Lett.*, *50*(2), 178-180.
- Bizet, K., Gabrielli, C., Perrot, H., & Therasse, J. (1998). Validation of antibody-based recognition by piezoelectric transducers through electroacoustic admittance analysis. *Biosens. Bioelectron.*, *13*(3-4), 259-269.
- Böhm, J., Lambert, O., Frangakis, A. S., Letellier, L., Baumeister, W., & Rigaud, J. L. (2001, August). FhuA-mediated phage genome transfer into liposomes: A cryo-electron tomography study. *Current Biology*, *11*(1168-1175), 963-971.
- Bonhivers, M., Plancon, L., Ghazi, A., Boulanger, P., Maire, M. le, Lambert, O., et al. (1998, May/June). FhuA, an escherichia coli outer membrane protein with a dual function of transporter and channel which mediates the transport of phage DNA. *Biochimie*, *80*(363-369), 963-971.
- Boskovic, S., Chon, J. W. M., Mulvaney, P., & Sader, J. E. (2002, July/August). Rheological measurements using microcantilevers. *J. Rheol.*, *46*, 891-899.
- Boulanger, P., Maire, M. le, Bonhivers, M., Dubois, S., Desmadril, M., & Letellier, L. (1996). Purification and structural and functional characterization of FhuA, a transporter of the escherichia coli outer membrane. *Biochemistry*, *35*(45), 14216-14224.
- Braun, T., Backmann, N., Bietsch, A., Gerber, C., Lang, H. P., & Hegner, M. (2006). Conformational change of bacteriorhodopsin quantitatively monitored by microcantilever sensors. *Biophys. J.*, *90*(8), 2970-2977.
- Braun, T., Barwich, V., Ghatkesar, M. K., Bredekamp, A. H., Gerber, C., Hegner, M., et al. (2005). Micromechanical mass sensors for biomolecular detection in a physiological environment. *Phys. Rev. E*, *72*, 031907.
- Braun, T., Ghatkesar, M. K., Barwich, V., Backmann, N., Huber, F., Grange, W., et al. (2007). Digital processing of multi-mode nano-mechanical cantilever data. *J. of Phys., Conference Series*, *61*, 341-345.
- Braun, T., Huber, F., Ghatkesar, M. K., Backmann, N., Lang, H.-P., Gerber, C., et al. (2007). Processing of kinetic microarray signals. *Sensors and Actuators B, Accepted*.

- Braun, T., Kaufmann, T., Remigy, H., & Engel, A. (2005). Encyclopedic reference of genomics and proteomics in molecular medicine. In (chap. Two-dimensional Crystallization of Membrane Proteins).
- Braun, V., & Braun, M. (2002). Iron transport and signaling in *Escherichia coli*. *FEBS Lett*, 529(1), 78-85.
- Burg, T. P., Godin, M., Knudsen, S. M., Shen, W., Carlson, G., Foster, J. S., et al. (2007, April). Weighing of biomolecules, single cells and single nanoparticles in fluid. *Nature*, 446, 1066-1069.
- Butt, H.-J., & Jaschke, M. (1995). Calculation of thermal noise in atomic force microscopy. *Nanotechnology*, 6, 1-7.
- Butt, R.-J., Siedle, P., Seifert, K., Fendler, K., Bamberg, E., Goldie, K., et al. (1993). Scan speed limit in atomic force microscopy. *Journal of Microscopy*, 169, 75.
- Calleja, M., Nordstro, M., Ivarez, M. A., Tamayo, J., Lechugaa, L., & Boisen, A. (2005, November). Highly sensitive polymer-based cantilever-sensors for *dna* detection. *Ultramicroscopy*, 105(13), 215-222.
- Cha, T., Guo, A., & Zhu, X.-Y. (2006). Formation of supported phospholipid bilayers on molecular surfaces: role of surface charge density and electrostatic interaction. *Biophys J*, 90(4), 1270-4.
- Chen, G. Y., Thundat, T., Wachter, E. A., & Warmack, R. J. (1995). Adsorption-induced surface stress and its effects on resonance frequency of microcantilevers. *J. Appl. Phys.*, 77(8), 3816-3622.
- Chen, G. Y., Warmack, R. J., Thundat, T., & Allison, D. (1994). Resonance response of scanning force microscopy cantilevers. *Rev. Sci. Instrum.*, 65, 2532.
- Chon, J. W. M., Mulvaney, P., & Sader, J. E. (2000). Experimental validation of theoretical models for the frequency response of atomic force microscope cantilever beams immersed in fluids. *J. Appl. Phys.*, 87(8), 3978-3988.
- Chu, W. H. (1963). *Vibration of fully submerged cantilever plates in water* (Technical Report No. 2). South-West Research Institute.
- Craighead, H. G. (2000, November). Nanoelectromechanical systems. *Science*, 290, 1532-1535.
- Despont, M., Drechsler, U., Yu, R., Pogge, H., & Vettiger, P. (2004). Wafer-scale microdevice transfer/interconnect: Its application in an AFM-based data-storage system. *Journal of micromechanical systems*, 13(6), 895-901.
- Destoumieux-Garzón, D., Duquesne, S., Péduzzi, J., Goulard, C., Desmadril, M., Letellier, L., et al. (2005, April). The iron-siderophore transporter FhuA is the receptor for microcin J25: role of the microcin val11-pro16 beta-hairpin region in the recognition mechanism. *Biochem J*, 389(3), 869.
- Dohn, S., Sandberg, R., Svendsen, W., & Boisen, A. (2005, June). Enhanced functionality of cantilever based mass sensors using higher modes. *Appl. Phys. Lett.*, 86, 233501-233503.

- Dorrestijn, M. (2006). *Nanomechanical sensing in liquid*. Doctoral dissertation, Institute for Physics, University of Basel.
- Dorrestijn, M., Bietsch, A., Acikalin, T., Raman, A., Hegner, M., Meyer, E., et al. (2007, January). Chladni figures revisited based on nanomechanics. *Phys. Rev. Lett.*, *98*(1), 026102.
- Eigler, D., & Schweizer, E. (1990, April). Positioning single atoms with a scanning tunneling microscope. *Nature*, *344*, 524-526.
- Ekinci, K. L., Huang, X. M. H., & Roukes, M. L. (2004, May). Ultrasensitive nanoelectromechanical mass detection. *Appl. Phys. Lett.*, *8*(22), 4469-4471.
- Ekinci, K. L., & Roukes, M. L. (2005). Nanoelectromechanical systems. *Rev. Sci. Instrum.*, *76*, 061101.
- Elmer, F.-J., & Dreier, M. (1997). Eigenfrequencies of a rectangular atomic force microscope cantilever in a medium. *J. of Appl. Phys.*, *81*(12), 7709-7714.
- Engvall, E., & Perlman, P. (1971). Enzyme-linked immunosorbent assay (elisa). quantitative assay of immunoglobulin g. *Immunochemistry*, *8*(9), 871-4.
- Eysden, C. A. V., & Sader, J. E. (2006). Resonant frequencies of a rectangular cantilever immersed in a fluid. *J. Appl. Phys.*, *100*, 114916.
- Eysden, C. A. V., & Sader, J. E. (2007). Frequency response of cantilever beams immersed in viscous fluids with applications to the atomic force microscope: Arbitrary mode order. *J. Appl. Phys.*, *101*, 044908.
- Ferguson, A. D., Kodding, J., Walker, G., Bos, C., Coulton, J. W., Diederichs, K., et al. (2001). Active transport of an antibiotic rifamycin derivative by the outer-membrane protein fhua. *Structure*, *9*(8), 707-16.
- Fields, S., & Song, O. (1989). A novel genetic system to detect protein-protein interactions. *Nature*, *340*(6230), 245-6.
- Fritz, J., Baller, M. K., Lang, H. P., Rothuizen, H., Vettiger, P., Meyer, E., et al. (2000). Translating biomolecular recognition into nanomechanics. *Science*, *288*(5464), 316-8.
- Fritz, J., Baller, M. K., Lang, H. P., Strunz, T., Meyer, E., Güntherodt, H.-J., et al. (2000). Stress at the solid-liquid interface of self-assembled monolayers on gold investigated with a nanomechanical sensor. *Langmuir*, *16*, 9694-9696.
- Gerber, C., & Lang, H. P. (2006, October). How the doors to the nanoworld were open. *Nat. Nano.*, *1*, 3-5.
- Gfeller, K. Y., Nugaeva, N., & Hegner, M. (2005a). Micromechanical oscillators as rapid biosensor for the detection of active growth of *escherichia coli*. *Biosens. Bioelectron.*, *21*(3), 528-533.
- Gfeller, K. Y., Nugaeva, N., & Hegner, M. (2005b). Rapid biosensor for detection of antibiotic-selective growth of *escherichia coli*. *Appl Environ Microbiol*, *71*(5), 2626-31.

- Ghatkesar, M. K., Barwich, V., Braun, T., Bredekamp, A. H., Drechsler, U., Despont, M., et al. (2004). Real-time mass sensing by nanomechanical resonators in fluid. In *Proceedings of third IEEE international conference on sensors 2004* (p. 1060-1063).
- Ghatkesar, M. K., Braun, T., Barwich, V., Ramseyer, J. P., Gerber, C., Hegner, M., et al. (2007). Resonating modes of vibrating microcantilevers in liquid. *Submitted*.
- Gimzewski, J. K., Gerber, C., Meyer, E., & Schlittler, R. R. (1994). Observation of a chemical-reaction using a micromechanical cantilever sensor. *Chemical Physics letters*, 217(5-6), 589-594.
- Godin, M., Tabard-Cossa, V., Grütter, P., & Williams, P. (2001, July). Quantitative surface stress measurements using a microcantilever. *Appl. Phys. Lett.*, 79(4), 013701-013705.
- Grange, W., Husale, S., Güntherodt, H.-J., & Hegner, M. (2002). Optical tweezers system measuring the change in light momentum flux. *Rev. of Sci. Instr.*, 73(6), 2308-2316.
- Gronewold, T. M. A., Baumgartner, A., Quandt, E., & Famulok, M. (2006). Discrimination of single mutations in cancer-related gene fragments with a surface acoustic wave sensor. *Anal. Chem.*, 78(14), 4865-4871.
- Gupta, A., Akin, D., & Bashir, R. (2004). Single virus particle mass detection using microresonators with nanoscale thickness. *Appl. Phys. Lett.*, 84, 1976.
- Herman, D., Gaitan, M., & DeVoe, D. (2001, June). MEMS test structures for mechanical characterization of vlsi thin films. In *Proc. SEM conference*. Portland, Oregon.
- Higgins, M. J., Proksch, R., Sader, J. E., Polcikb, M., Endoo, S. M., Cleveland, J. P., et al. (2006). Noninvasive determination of optical lever sensitivity in atomic force microscopy. *Rev. Sci. Instrum.*, 77, 013701-013705.
- Homola, J., Yee, S. S., & Gauglitz, G. (1999). Surface plasmon resonance sensors: Review. *Sensors and Actuators B*, 54(1-2), 3-15.
- Hu, Z., Seeley, T., Kossek, S., & Thundat, T. (2004, February). Noninvasive determination of optical lever sensitivity in atomic force microscopy. *Rev. Sci. Instrum.*, 75(2), 400-404.
- Huber, F., Hegner, M., Gerber, C., Güntherodt, H.-J., & Lang, H. P. (2006). Label free analysis of transcription factors using microcantilever arrays. *Biosens. Bioelec.*, 21, 1599-1605.
- Ilic, B., Craighead, H. G., Krylov, S., Senaratne, W., Ober, C., & Neuzil, P. (2004, April). Attogram detection using nanoelectromechanical oscillators. *J. Appl. Phys.*, 95(7), 3694-3703.
- Ilic, B., Yang, Y., & Craighead, H. G. (2004, September). Virus detection using nanoelectromechanical devices. *Appl. Phys. Lett.*, 85(13), 2604-2606.
- Jap, B. K., Zulauf, M., Scheybani, T., Hefti, A., Baumeister, W., Aebi, U., et al. (1992). 2D crystallization: From art to science. *Ultramicroscopy*, 46(1-4), 45-84.

- Ji, H.-F., Feng, Y., Xu, X., Purushotham, V., Thundat, T., & Brown, G. M. (2004, November). Photon-driven nanomechanical cyclic motion. *Chem. Comm.*, 21(22), 2532-2533.
- Jordan, C., & Corn, R. (1997, APR 1). Surface plasmon resonance imaging measurements of electrostatic biopolymer adsorption onto chemically modified gold surfaces. *Anal. Chem.*, 69, 1449–1456.
- Jr, G. C. W., McBride, S. E., Warmack, R. J., & Sande, B. V. (1989, August). Calibration of scanning tunneling microscope transducers using optical beam deflection. *Appl. Phys. Lett.*, 55(6), 528-530.
- Junker, R., Heinrich, J., Ulbrich, H., Schulte, H., Schönfeld, R., Köhler, E., et al. (1998). Relationship between plasma viscosity and the severity of coronary heart disease. *Arterioscler. Thromb. Vasc. Biol.*, 18, 870-875.
- Kirstein, S., Mertesdorf, M., & Schönhoff, M. (1998). The influence of a viscous fluid on the vibration dynamics of scanning near-field optical microscopy fiber probes and atomic force microscopy cantilevers. *J. Appl. Phys.*, 84(4), 1782-1789.
- Koenig, W., Sund, M., Filipiak, B., Döring, A., Löwel, H., & Ernst, E. (1998). Plasma viscosity and the risk of coronary heart disease : Results from the MONICA-augsburg cohort study, 1984 to 1992. *Arterioscler. Thromb. Vasc. Biol.*, 18, 768-772.
- Koenig, W., Sund, M., Lowe, G., Lee, A. J., Resch, K. L., Tunstall-Pedoe, H., et al. (2001, January). Simultaneous liquid viscosity and density determination with piezoelectric unimorph cantilevers. *J. Appl. Phys.*, 89, 1497-1505.
- Lambert, O., Plancon, L., Rigaud, J. L., & Letellier, L. (1998, November). Protein-mediated dna transfer into liposomes. *Molecular Microbiology*, 30(761-765), 963-971.
- Lang, H. P., Berger, R., Andreoli, C., Brugger, J., Despont, M., Vettiger, P., et al. (1998, January). Novel sequential position readout from arrays of micromechanical cantilever sensors. *Appl. Phys. Lett.*, 72(3), 383-385.
- Lang, H. P., Berger, R., Battiston, F., Ramseyer, J. P., Meyer, E., Andreoli, C., et al. (1998). A chemical sensor based on a micromechanical cantilever array for the identification of gases and vapors. *Appl. Phys. A*, 66(S61-S64), 2532-2533.
- Lang, H. P., Hegner, M., & Gerber, C. (2005, April). Cantilever array sensors. *Materials Today*, 8, 30-36.
- Lang, H. P., Hegner, M., & Gerber, C. (2006). Nanomechanical cantilever array sensors. In *Springer handbook of nanotechnology, 2nd edition* (p. 443-450). Springer Verlag (Berlin, New York, Heidelberg).
- Lévêque, G., Ferrandis, J. Y., Est, J. V., & Cros, B. (2000, March). An acoustic sensor for simultaneous density and viscosity measurements in liquids. *Rev. Sci. Instrum.*, 71(3), 1433-1440.
- Lutwyche, M. I., Despont, M., Drechsler, U., Dürig, U., Häberle, W., Rothuizen, H., et al. (2000, November). Highly parallel data storage system based on scanning probe arrays. *Appl. Phys. Lett.*, 77(20), 3-5.

- Maali, A., Hurth, C., Boisgard, R., Jai, C., Cohen-Bouhacina, T., & Aiméa, J.-P. (2005). Hydrodynamics of oscillating atomic force microscopy cantilevers in viscous fluids. *J. Appl. Phys.*, *97*, 074907.
- Manoharan, H. C., Lutz, C. P., & Eigler, D. (2000, February). Quantum mirages formed by coherent projection of electronic structure. *Nature*, *403*, 512-515.
- Marx, K. A. (2003). Quartz crystal microbalance: a useful tool for studying thin polymer films and complex biomolecular systems at the solution-surface interface. *Biomacromolecules*, *4*(5), 1099-120.
- McKendry, R., Zhang, J., Arntz, Y., Strunz, T., Hegner, M., Lang, H. P., et al. (2002). Multiple label-free biodetection and quantitative DNA-binding assays on a nanomechanical cantilever array. *PNAS*, *99*(15), 9783-9788.
- Meyer, G., & Amer, N. M. (1988, September). Novel optical approach to atomic force microscopy. *Appl. Phys. Lett.*, *53*(12), 1045-1047.
- Miyatani, T., & Fujihira, M. (1997, June). Calibration of surface stress measurements with atomic force microscopy. *J. Appl. Phys.*, *81*(11), 400-404.
- Mukhopadhyay, R., Sumbayev, V. V., Lorentzen, M., Kjems, J., Andreasen, P. A., & Besenbacher, F. (2005, April). Cantilever sensor for nanomechanical detection of specific protein conformations. *Nano Lett.*, *5*(12), 2385-2388.
- Nelson, B. P., Grimsrud, T. E., Liles, M. R., Goodman, R. M., & Corn, R. M. (2001). Surface plasmon resonance imaging measurements of DNA and RNA hybridization adsorption onto DNA microarrays. *Anal. Chem.*, *73*(1), 1-7.
- Nugaeva, N., Gfeller, K. Y., Backmann, N., Duggelin, M., Lang, H. P., Güntherodt, H.-J., et al. (2007, February). An antibody-sensitized microfabricated cantilever for the growth detection of aspergillus niger spores. *Microscopy and Microanalysis*, *13*, 13-17.
- Nugaeva, N., Gfeller, K. Y., Backmann, N., Lang, H. P., Duggelin, M., & Hegner, M. (2005, March). Micromechanical cantilever array sensors for selective fungal immobilization and fast growth detection. *Biosens. Bioelectron.*, *21*, 849-856.
- Oden, P. I., Chen, G. Y., Steele, R. A., Warmack, R. J., & Thundat, T. (1996, June). Viscous drag measurements utilizing microfabricated cantilevers. *Appl. Phys. Lett.*, *68*, 3814-3816.
- Paul, M. R., Clark, M. T., & Cross, M. C. (2006). The stochastic dynamics of micron and nanoscale elastic cantilevers in fluid: fluctuations from dissipation. *Nanotechnology*, *17*, 4502-4513.
- Pinnaduwage, L. A., Hawk, J. E., Boiadjev, V., Yi, D., & Thundat, T. (2003, August). Use of microcantilevers for the monitoring of molecular binding to self-assembled monolayers. *Langmuir*, *19*(19), 7841-7844.
- Quist, A., Chand, A., Ramachandran, S., Cohena, D., & Lal, R. (2006). Piezoresistive cantilever based nanoflow and viscosity sensor for microchannels. *Lab on a Chip*, *6*, 1450-1454.

- Rabe, U., Janser, K., & Arnold, W. (1996). Vibrations of free and surface-coupled atomic force microscopy cantilevers: Theory and experiment. *Rev. Sci. Instrum.*, *67*(7), 3281-3293.
- Raghuraman, H., & Chattopadhyay, A. (2006, December). Melittin: a membrane-active peptide with diverse functions. *Biosci Rep.*
- Ramos, D., Tamayo, J., Mertens, J., Calleja, M., & Zaballos, A. (2006, November). Origin of the response of nanomechanical resonators to bacteria adsorption. *J. Appl. Phys.*, *100*, 106105-106107.
- Rast, S., Wattering, C., Gysin, U., & Meyer, E. (2000). Dynamics of damped cantilevers. *Rev. Sci. Instrum.*, *71*(7), 2772-2775.
- Rex, S., & Schwarz, G. (1998). Quantitative studies on the melittin-induced leakage mechanism of lipid vesicles. *Biochemistry*, *37*, 2336-2345.
- Sader, J. E. (1998). Frequency response of cantilever beams immersed in viscous fluids with applications to the atomic force microscope. *J. Appl. Phys.*, *84*(10), 64-76.
- Shih, W. Y., Li, X., Gu, H., Shih, W.-H., & Aksay, I. A. (1994, September). Geographical variations in plasma viscosity and relation to coronary event rates. *The Lancet*, *344*, 711-714.
- Shu, W., Liu, D., Watari, M., Riener, C. K., Strunz, T., Welland, M. E., et al. (2005). DNA molecular motor driven micromechanical cantilever arrays. *J. Am. Chem. Soc.*, *127*, 17054-17060.
- Stoney, G. G. (1909). *The tension of metallic films deposited by electrolysis*. Proceedings of Royal Society of London.
- Takai, E., Costa, K. D., Shaheen, A., Hung, C. T., & GUO, X. E. (2005, July). Osteoblast elastic modulus measured by atomic force microscopy is substrate dependent. *Annals of Biomedical Engineering*, *33*(7), 963-971.
- Tamayo, J., Humphris, A. D. L., Malloy, A., & Miles, M. (2001). Chemical sensors and biosensors in liquid environment based on microcantilevers with amplified quality factor. *Ultramicroscopy*, *86*, 167-173.
- Tamayo, J., Ramos, D., Mertens, J., & Calleja, M. (2006, November). Origin of the response of nanomechanical resonators to bacteria adsorption. *Appl. Phys. Lett.*, *89*, 224104-224106.
- Thomas, W. E., Nilsson, L. M., Forero, M., Sokurenko, E. V., & Vogel, V. (2004). Shear-dependent 'stick-and-roll' adhesion of type 1 fimbriated *Escherichia coli*. *Mol Microbiol*, *53*(5), 1545-57.
- Thundat, T., Warmack, R. J., Chen, G. Y., & Allison, D. P. (1994). Thermal and ambient-induced deflections of scanning force microscope cantilevers. *Appl. Phys. Lett.*, *64*, 2894.
- Timoshenko, S. P., & Young, D. H. (2003). *Elements of strength of materials*. Litton Educational Publishing, Inc.

- Van Holde, K., Johnson, W. K., & Shing Ho, P. (2006). *Principles of physical biochemistry*. Pearson Education International.
- Wachter, E. A., & Thundat, T. (1995, June). Micromechanical sensors for chemical and physical measurements. *Rev. Sci. Instrum.*, 66(6), 3662-3667.
- Wagegg, W., & Braun, V. (1981). Ferric citrate transport in escherichia coli requires outer membrane receptor protein feca. *J Bacteriol*, 145(1), 156-63.
- Wagner, P., Hegner, M., Kernen, P., Zaugg, F., & Semenza, G. (1996). Covalent immobilization of native biomolecules onto au(111) via n-hydroxysuccinimide ester functionalized self-assembled monolayers for scanning probe microscopy. *Biophys J*, 70(5), 2052-66.
- Wagner, P., Kernen, P., Hegner, M., Ungewickell, E., & Semenza, G. (1994). Covalent anchoring of proteins onto gold-directed NHS-terminated self-assembled monolayers in aqueous buffers: SFM imaging of clathrin and its cages. *FEBS Letters*, 356, 267.
- Wang, Z. H., & Jin, G. (2003). A label-free multisensing immunosensor based on imaging ellipsometry. *Anal. Chem.*, 75(22), 6119-6123.
- Watari, M., Galbraith, J., Lang, H. P., Sousa, M., Hegner, M., Gerber, C., et al. (2007). Investigating the molecular mechanisms of in-plane mechanochemistry on cantilever arrays. *JACS*, 129(3), 601-609.
- Weigert, S., Dreier, M., & Hegner, M. (1996). Frequency shifts of cantilevers vibrating in various media. *Appl. Phys. Lett.*, 69(19), 2834-2836.
- Wink, T., Zuilen, S. J. van, Bult, A., & Bennekom, W. P. van. (1997). Self-assembled monolayers for biosensors. *Analyst*, 122, 43R-50R.
- Wise, A., Gearing, K., & Rees, S. (2002). Target validation of g-protein coupled receptors. *Drug Discov. Today*, 7(4), 235-46.
- Wu, G., Datar, R. H., Hansen, K. M., Thundat, T., Cote, R. J., & Majumdar, A. (2001, September). Bioassay of prostate-specific antigen (psa) using microcantilevers. *Nat. Biotech.*, 19, 856-860.
- Wu, G., Ji, H., Hansen, K., Thundat, T., Datar, R., Cote, R., et al. (2001, February). Origin of nanomechanical cantilever motion generated from biomolecular interactions. *PNAS*, 98(4), 1560-1564.
- Xiaodi, S., Wu, Y.-J., Rudolf, R., & Woldgang, K. (2005). Surface plasmon resonance spectroscopy and quartz crystal microbalance study of streptavidin film structure effects on biotinylated DNA assembly and target DNA hybridization. *Langmuir*, 21(1), 348-353.
- Yang, Y. T., Callegari, C., Feng, X. L., Ekinci, K. L., & Roukes, M. L. (2006, April). Zeptogram-scale nanomechanical mass sensing. *Nano Letters*, 6(4), 583-586.
- Young, D., & Felgar, R. P. (1949). Tables of characteristic functions representing normal modes of vibration of a beam. *The University of Texas Publication*, 44(4913), 1-32.
- Zachary, D. J., & Boisen, A. (2005). Aluminum nanocantilevers for high sensitivity mass sensors. *Appl. Phys. Lett.*, 87, 013102-013104.

Zhang, J., Lang, H. P., Huber, F., Bietsch, A., Grange, W., Certa, U., et al. (2006, December). Rapid and label-free nanomechanical detection of biomarker transcripts in human RNA. *Nat. Nano.*, *1*(3), 214–220.

Zhang, Y., Venkatachalan, S. P., Xu, H., Xu, X., Joshi, P., Ji, H.-F., et al. (2004). Micromechanical measurement of membrane receptor binding for label-free drug discovery. *Biosens. Bioelectron.*, *19*, 1473-8.

PUBLICATIONS AND PRESENTATIONS

Publications

M. K. Ghatkesar, V. Barwich, T. Braun, A.H. Bredekamp, U. Drechsler, M. Despont, H.P. Lang, M. Hegner, Ch. Gerber, Real-Time Mass Sensing by Nanomechanical Resonators in Fluid, *Proc.IEEE Sensors*, 1060-1063 (2004).

T. Braun, V. Barwich, M. K. Ghatkesar, A.H. Bredekamp, Ch. Gerber, M. Hegner, H. P. Lang, "Micromechanical mass sensors for biomolecular detection in a physiological environment", *Phys.Rev.E* 72, 031907 (2005).

T. Braun, M. K. Ghatkesar, V. Barwich, N. Backmann, F. Huber, W. Grange, N. Nugaeva, H. P. Lang, J. ŮP. Ramseyer, Ch. Gerber and M. Hegner, Digital processing of multi-mode nano-mechanical cantilever data, *JournalofPhysics : ConferenceSeries*, 341-345 (2007).

M. K. Ghatkesar, V. Barwich, T. Braun, J. -P. Ramseyer, U. Drechsler, M. Despont, Ch. Gerber, M. Hegner, H.P. Lang, Higher modes of vibration increase mass sensitivity in nanomechanical cantilevers, Submitted.

M. K. Ghatkesar, T. Braun, V. Barwich, J. -P. Ramseyer, Ch. Gerber, M. Hegner, H.P. Lang, Vibrating nanomechanical cantilevers in liquid, Submitted.

M. K. Ghatkesar, T. Braun, Ch. Gerber, H. P. Lang and M. Hegner, Simultaneous measurement of mass adsorption and structural change of biomolecules, Manuscript in preparation.

T. Braun, M K. Ghatkesar, W. Grange, P. Boulanger, L. Letellier, H. P. Lang, A. Bietsch, Ch. Gerber and M. Hegner, Quantitative, time-resolved measurement of virus binding to membrane protein receptors, Manuscript in preparation.

M. K. Ghatkesar, T. Braun, Ch. Gerber, M. Hegner and H. P. Lang, Rheological effects of liquid on resonating nanomechanical microcantilevers, Manuscript in preparation.

Presentations

Oral

Microcantilever sensors vibrating in liquid: A sojourn from setup to biosensing, Strategic Research Area Meeting: Biosensors, Basel, Switzerland (May 2007).

Simultaneous detection of mass adsorption and surface stress on a nanomechanical cantilever, Exploring new frontiers in bio/nano, Zermat, Switzerland (March 2007).

Flapping nanomechanical cantilevers sense happy biomolecular partners in real-time, International conference on nanoscience and technology NANO9 meets STM06, Basel, Switzerland (August 2006).

Micro spring boards can catch virus, Frontiers Meeting, Lenzerheide, Switzerland (March 2006).

Nanomechanics of microcantilevers, Department of Instrumentation, Indian Institute of Science, India (INVITED) (January 2006).

Mass measurements using dynamic mode in fluids, Frontiers cantilevers idea exchange meeting, Basel, Switzerland (June 2005)

Real time mass sensing by nanomechanical resonators in fluid, IEEE Sensors conference 2004, Vienna, Austria (October 2004).

Poster

Towards combined static and dynamic mode cantilever bio-sensing, Frontiers annual meeting, Sicily, Italy (October 2006).

Virus detection with cantilever sensors, Frontiers young scientists meeting, Karlsruhe, Germany (March 2006).

Development and exploration of cantilever sensor array techniques, Nanofair, St.Gallen, Switzerland (Nov 2004).

CURRICULUM VITAE

Personal Details

Name : Murali Krishna Ghatkesar
Nationality : Indian
Place of Birth : Hyderabad, India
Date of Birth : 19 May 1975

Education

2007 Ph.D. in Experimental Physics, University of Basel, Switzerland.
2001 M.Sc[Engg] in Instrumentation, Indian Institute of Science, India.
1997 M.Sc in Electronics, University of Hyderabad, India.
1995 B.Sc in Electronics, Osmania University, India.

Experience

May 2003 - Jun 2007 University of Basel, Switzerland.

- Dissertation: Resonating nanomechanical microcantilevers for quantitative biological measurements in liquid.

Jan 2003 - May 2003 Indian Institute of Science, Bangalore, India.

- Research Assistant, High Enthalpy Aerodynamics Laboratory: Responsible for development of thin film heat transfer gauges for hypersonic shock tunnel.

Apr 2001 - Sep 2002 HelloSoft Inc, Hyderabad, India

- Member of Technical Staff, Digital Signal Processing group: Responsible for optimization of speech codecs on Analog Devices DSP processors.

Jun 1998 - Mar 2001 Indian Institute of Science, Bangalore, India

- Thesis: Development of tactile sensors based on piezoelectric resonance and surface acoustic wave techniques.

Jun 1995 - Mar 1997 University of Hyderabad, India

- Project: Uninterruptible power supply based on pulse width modulation.